



Universidade do Estado do Rio de Janeiro

Centro de Tecnologia e Ciências

Instituto Politécnico

Alexandre Melhorce Barboza

**Deformation mechanisms and properties of nanocrystalline Al, Ni and
 $\text{Al}_{80}\text{Ti}_{15}\text{Ni}_5$ alloy: a molecular dynamics study**

Nova Friburgo

2021

Alexandre Melhorance Barboza

**Deformation mechanisms and properties of nanocrystalline Al, Ni and Al₈₀Ti₁₅Ni₅ alloy:
a molecular dynamics study**



Tese apresentada, como requisito parcial para obtenção do título de Doutor, ao Programa de Pós-Graduação em Modelagem Computacional da Universidade do Estado do Rio de Janeiro.

Orientadores: Prof. Dr. Ivan Napoleão Bastos

Prof. Dr. Luis César Rodríguez Aliaga

Nova Friburgo

2021

CATALOGAÇÃO NA FONTE
UERJ/REDE SIRIUS/BIBLIOTECA CTC/E

B239 Barboza, Alexandre Melhorance.
Deformation mechanisms and properties of nanocrystalline Al, Ni
and Al₈₀Ti₁₅Ni₅ alloy: a molecular dynamics study / Alexandre
Melhorance Barboza. – 2021.
91 f. : il.

Orientadores: Ivan Napoleão Bastos e Luis César Rodríguez
Aliaga.

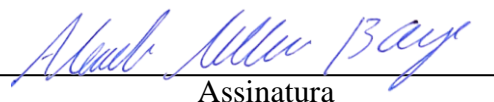
Tese (doutorado) - Universidade do Estado do Rio de Janeiro,
Instituto Politécnico.

1. Metais – Propriedades mecânicas - Teses. 2. Metais -
Deformação - Teses. 3. Ligas – Propriedades mecânicas - Teses. 4.
Dinâmica molecular - Métodos de simulação - Teses. I. Bastos, Ivan
Napoleão. II. Aliaga, Luis César Rodríguez. III. Universidade do
Estado do Rio de Janeiro. Instituto Politécnico. IV. Título.

CDU 620.173.26

Bibliotecária Cleide Sancho CRB7/5843

Autorizo, apenas para fins acadêmicos e científicos, a reprodução total ou parcial desta tese,
desde que citada a fonte.


Assinatura

16/07/2021

Data

Alexandre Melhorance Barboza

**Deformation mechanisms and properties of nanocrystalline Al, Ni and Al₈₀Ti₁₅Ni₅ alloy:
a molecular dynamics study**

Tese apresentada, como requisito parcial para
obtenção do título de Doutor, ao Programa de Pós-
Graduação em Modelagem Computacional da
Universidade do Estado do Rio de Janeiro.

Aprovada em 29 de abril de 2021.

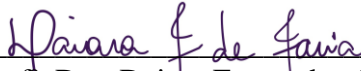
Banca Examinadora:



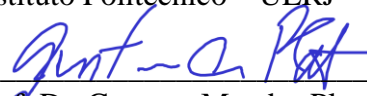
Prof. Dr. Ivan Napoleão Bastos (Orientador)
Instituto Politécnico – UERJ



Prof. Dr. Luis César Rodríguez Aliaga (Orientador)
Instituto Politécnico – UERJ



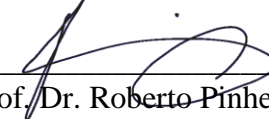
Prof. Dra. Daiana Fernandes de Faria
Instituto Politécnico – UERJ



Prof. Dr. Gustavo Mendes Platt
Universidade Federal do Rio Grande



Prof. Dr. Piter Gargarella
Universidade Federal de São Carlos



Prof. Dr. Roberto Pinheiro Domingos
Instituto Politécnico - UERJ

Nova Friburgo

2021

DEDICATION

À minha família e em memória de meu pai.

Our greatest glory is not in never falling, but in rising every time we fall.

Oliver Goldsmith

ABSTRACT

BARBOZA, A. M. *Deformation mechanisms and properties of nanocrystalline Al, Ni and Al₈₀Ti₁₅Ni₅ alloy: A molecular dynamics study*. 2021. 91 f. Tese (Doutorado em Modelagem Computacional) – Instituto Politécnico, Universidade do Estado do Rio de Janeiro, Nova Friburgo, 2021.

Nanocrystalline metals and alloys show promising properties for technological applications. However, their unusual mechanical behavior proved to be a real challenge to be understood. Experimental studies of these materials are affected by complexity and cost in creating a bulk sample free of defects. Thus, molecular dynamics simulations have emerged as an important tool to assess, at atomic level, the phenomena responsible for their behavior. In this thesis, three different nanocrystalline systems (Al₈₀Ti₁₅Ni₅ alloy, pure nickel, and pure aluminum) were studied using molecular dynamics. The focus was to analyze the systems' mechanical behavior with special attention to the inverse Hall-Petch relationship and the related deformation mechanisms. Atomic arrangement analysis of the ternary alloy demonstrated the grain boundary sliding and diffusion as the dominant deformation mechanisms. In addition, deformation mechanisms present in amorphous materials seems to be capable of work in nanocrystalline systems. The results related to nanocrystalline nickel demonstrated that partial dislocations remain active regardless of grain size. However, other deformation mechanisms, such as grain rotation and grain boundary sliding, takes place below a critical grain size of *circa* 20 nm, leading to the inverse Hall-Petch relationship. Moreover, a distinct strain rate sensitivity behavior was found, in which it decreases with the grain size reduction. Regarding the nanocrystalline aluminum, Coble creep phenomenon was observed and no clear indication of dislocation pile-up was evidenced.

Keywords: Nanocrystalline materials. Aluminum. Nickel. Titanium. Molecular dynamics. Hall-Petch. Deformation mechanisms.

RESUMO

BARBOZA, A. M. *Mecanismos de deformação e propriedades mecânicas do Al, Ni e liga Al₈₀Ti₁₅Ni₅: um estudo por dinâmica molecular*. 2021. 91 f. Tese (Doutorado em Modelagem Computacional) – Instituto Politécnico, Universidade do Estado do Rio de Janeiro, Nova Friburgo, 2021.

Os metais e ligas nanocristalinas apresentam propriedades promissoras para o uso em aplicações tecnológicas. No entanto, seu comportamento mecânico incomum mostra-se um verdadeiro desafio para ser compreendido. Estudos experimentais destes materiais são afetados pela complexidade e custo para se criar amostras livres de defeitos. Assim, as simulações de dinâmica molecular surgiram como uma importante ferramenta para avaliar, a nível atômico, os fenômenos responsáveis por tal comportamento. Nesta tese, três sistemas nanocristalinos (liga Al₈₀Ti₁₅Ni₅, níquel puro e alumínio puro) foram estudados usando dinâmica molecular. O foco foi a análise do comportamento mecânico com atenção especial à relação inversa de Hall-Petch e aos mecanismos de deformação relacionados. Análise do arranjo atômico da liga ternária demonstrou o deslizamento e difusão do contorno de grão como os mecanismos de deformação dominantes. Além disso, mecanismos de deformação presentes em materiais amorfos parecem ser capazes de atuar em sistema nanocristalinos. Os resultados relacionados ao níquel nanocristalino demonstraram que as discordâncias parciais se mantêm ativas independentemente do tamanho de grão. No entanto, outros mecanismos de deformação, como rotação do grão e deslizamento do contorno de grão, ocorrem abaixo de um tamanho crítico de grão de *circa* 20 nm, causando a relação inversa de Hall-Petch. Ademais, um comportamento distinto foi encontrado para a sensibilidade à taxa de deformação, a qual diminui com a redução do tamanho de grão. Com relação ao alumínio nanocristalino, o fenômeno de fluência de Coble foi observado e nenhuma indicação de empilhamento de discordâncias foi evidenciada.

Palavras-chave: Materiais nanocristalinos. Alumínio. Níquel. Titânio. Dinâmica molecular.

Hall-Petch. Mecanismos de deformação.

LIST OF FIGURES

Figure 1 – Schematic of the Lennard-Jones pair potential.....	25
Figure 2 – Schematic of potential cut- in two dimensions.....	28
Figure 3 – Creation of a Voronoi polyhedron.....	32
Figure 4 – Simulated structures of Al ₈₀ Ti ₁₅ Ni ₅ alloy and X-ray diffraction pattern.....	36
Figure 5 – Simulated tensile test for Al ₈₀ Ti ₁₅ Ni ₅ alloy at a strain rate of 1.0 x 10 ¹⁰ s ⁻¹	38
Figure 6 – Voronoi polyhedron analysis.....	40
Figure 7 – Structural evolution of the amorphous sample.....	41
Figure 8 – Atomic fraction related to strain for the nanocrystalline samples.....	42
Figure 9 – Dislocation evolution under different strains.....	43
Figure 10 – Grain tracking analysis for the d12 sample.....	45
Figure 11 – Stress-strain curves for Al, Ni and Ti with $d \approx 10$ nm using unary and ternary potentials.....	47
Figure 12 – Stress-strain curves for nanocrystalline Ni at 1.0 x 10 ¹⁰ s ⁻¹ strain rate.....	48
Figure 13 – Ultimate stress dependence on grain size for Ni.....	49
Figure 14 – Dislocation segments for the $d = 24.1$ nm sample at zero strain computed using the dislocation extraction algorithm.....	50
Figure 15 – Two partial dislocations separated by a fault ribbon forming an extended dislocation.....	51
Figure 16 – A slab with a thickness of 2.0 nm from the 24.1 nm nanocrystalline sample colored according to the local minimum non-affine displacement D_{min}^2	53
Figure 17 – Resolved shear stress required to nucleate partial and perfect dislocations at GB with dependency on the critical radius.....	55

Figure 18 – Partial dislocation emitted from GB.....	56
Figure 19 – Slab normal to the x-axis for the 8.7 nm sample with 0.2 nm width.....	57
Figure 20 – NH-like mechanism taking place in a grain.....	58
Figure 21 – Grain undergoing rotation.....	59
Figure 22 – Young’s modulus as a function of the reciprocal grain size.....	60
Figure 23 – Fraction of atoms structured as FCC and GB as a function of reciprocal grain size.....	60
Figure 24 – Young’s modulus of grain boundary E_{GB} using Voigt and Reuss model for composites materials.....	62
Figure 25 – Dependency of Young’s modulus with the grain size using the MD results and Reuss model for composites.....	62
Figure 26 – Stress relaxation curves for NC samples starting at $\varepsilon = 0.035$	63
Figure 27 – Plot for the sample with $d = 24.1$ nm grain size obtained from the stress relaxation curve.....	64
Figure 28 – Strain rate sensitivity, m , versus grain size.....	65
Figure 29 – Repeated stress relaxation tests.....	66
Figure 30 – Evolution of dislocations from GB for the sample with $d = 24.1$ nm....	68
Figure 31 – Plot of $\ln(-\dot{\sigma})$ against $\ln(\sigma)$ for the sample with $d = 15.0$ nm.....	69
Figure 32 – Grain volume distribution for the four Al nanocrystalline samples.....	71
Figure 33 – Stress-strain curves of Al nanocrystalline samples.....	71
Figure 34 – Conventional (dashed blue line) and inverse (dashed red line) Hall-Petch relationship.....	72
Figure 35 – Tensile test result after strain hardening of the 15-grain nanocrystalline sample.....	73
Figure 36 – A triple junction of the 15-grain sample.....	74

LIST OF TABLES

Table 1 –	Experimental results from literature for NC materials that present an inverse HP relationship.....	16
Table 2 –	Length, time scale and methods usually utilized in computational materials science to study crystalline materials.....	22
Table 3 –	Elastic modulus using unary and ternary potentials. The experimental values of nanocrystalline materials are present for comparison.....	46
Table 4 –	Mechanical properties related to the grain size.....	48

LIST OF ABBREVIATIONS

at. %	Atomic percent
BCC	Body Centered-Cubic
CNA	Common Neighbor Analysis
d10	Al ₈₀ Ti ₁₅ Ni ₅ sample with 10 nm grain size
d12	Al ₈₀ Ti ₁₅ Ni ₅ sample with 12 nm grain size
DXA	Dislocation Extraction Algorithm
EAM	Embedded-Atom Method
FCC	Face-Centered Cubic
FEA	Finite Element Analysis
FR	Frank-Read
GB	Grain Boundary
GBD	Grain Boundary Diffusion
GBS	Grain Boundary Sliding
GR	Grain Rotation
GTA	Grain Tracking Analysis
HCP	Hexagonal Close-Packed
HP	Hall-Petch
LRO	Long-Range Order
MD	Molecular Dynamics
MG	Metallic Glass
MRO	Medium-Range Order
NC	Nanocrystalline
NH	Nabarro-Herring
NPT	Isobaric-Isothermal Ensemble
NVE	Microcanonical Ensemble
NVT	Canonical Ensemble
SRO	Short-Range Order
SRS	Strain Rate Sensitivity
STZ	Shear Transformation Zone
UTS	Ultimate Tensile Stress
VP	Voronoi Polyhedron

LIST OF SYMBOLS

d	Grain size
σ_y	Yield stress
k_1	Constant
σ_0	Approximately the yield stress of a very coarse-grained polycrystal
T	Temperature
T_m	Melting temperature
$\dot{\epsilon}$	Strain rate
D_{gc}	Lattice diffusivity
σ	Stress
b	Burgers vector magnitude
k_B	Boltzmann constant
β	Constant
D_{GB}	Grain boundary diffusivity
θ	Constant
K'	Constant
σ_{GC}	Flow stress of dislocation-free grain core
σ_{GB}	Flow stress of the grain boundary region
k_2	Fitted parameter
k_3	Fitted parameter
p	Initial spatial configuration
U_p	Initial system energy
\vec{F}_i	Force vector on atom i
m_i	Atomic mass of atom i
\vec{a}_i	Acceleration vector of atom i
\vec{v}_i	Velocity vector of atom i
\vec{r}_i	Position vector of atom i
U	Potential energy
r_{ij}	Distance between atom i and j
φ_{ij}	Potential between atom i and j

γ	Distance at which the potential is zero
ϵ	Lowest energy of the potential curve
f	Some function of the interatomic distance
M	Functional of a sum over functions
ρ_e	Electron densities
$\bar{\rho}_i$	Electron gas density
t	Time
δt	Timestep
r_{cut}	Cut-off radius
$\langle T \rangle$	Average temperature over some time period
P	Pressure
$\langle P \rangle$	Average pressure over some time period
N	Number of atoms
K	Kinetic energy
V	System volume
E_T	Total energy
\vec{v}_i	Euclidean space point
$K-\alpha$	Alpha copper radiation wavelength
$Al-\alpha$	Aluminum alpha phase
σ_u	Ultimate tensile stress
ϵ	Strain
E	Young's modulus
n_i	Number of i -edged faces of a Voronoi polyhedron
$\langle n_3, n_4, n_5, \dots \rangle$	Voronoi index
ρ	Dislocation density
ρ_0	Initial dislocation density
d_c	Critical average grain size
D_{min}^2	Local minimum non-affine displacement
τ_h	Resolved shear stress for homogeneous nucleation of dislocations
m_S	Schmid factor
τ_p	Shear stress in a specific plane
τ_c	Resolved shear stress for nucleation of dislocations with stress concentrators

L	Distance between two anchor points
R_c	Critical semicircle configuration
τ_{crt}	Critical stress
ξ	Dislocation character
G	Shear modulus
τ_l	Leading partial dislocation stress required to reach R_c
γ_s	Stacking fault energy
b_l	Leading partial Burgers vector magnitude
R_l	Leading partial radius
F_{lt}	Interaction force per unit length acting between leading and trailing partial dislocation.
τ_l^*	Stress required to allow a leading partial to slip across the grain after its emission
R_t	Transition radius, from perfect to partial dislocation emission
L_t	Transition length
φ	Grain core volume fraction
E_{core}	Elasticity modulus of grain core
E_{GB}	Elasticity modulus of grain boundary
m	Strain rate sensitivity
$\dot{\sigma}$	Time derivative of the stress
V_a	Apparent activation volume

CONTENTS

	INTRODUCTION	15
1	LITERATURE REVIEW	18
2	SCOPE AND OBJECTIVES	30
3	METHODOLOGY	31
3.1	Al₈₀Ti₁₅Ni₅ Alloy	33
3.2	Nickel	33
3.3	Aluminum	34
4	RESULTS AND DISCUSSION	36
4.1	Al₈₀Ti₁₅Ni₅ Alloy	36
4.1.1	<u>Amorphous Al₈₀Ti₁₅Ni₅ deformation mechanisms</u>	39
4.1.2	<u>Nanocrystalline Al₈₀Ti₁₅Ni₅ deformation mechanisms</u>	41
4.1.3	<u>Influence of interatomic potential</u>	46
4.2	Nickel	47
4.2.1	<u>Effect of grain size on mechanical properties</u>	47
4.2.2	<u>Deformation behavior for sample with $d = 24.1$ nm</u>	49
4.2.3	<u>Deformation behavior for sample with $d = 8.7$ nm</u>	57
4.2.4	<u>Young's modulus and composite model</u>	59
4.2.5	<u>Strain rate sensitivity</u>	63
4.3	Aluminum	70
	CONCLUSIONS	75
	REFERENCES	77
	APPENDIX – Works produced from this thesis	91

INTRODUCTION

The development of new materials has always affected evolution of industries, which directly affects the progress of society and the people's living standards^{1,2}. In general, novel materials have significant advantages over traditional ones, allowing them to perform better in specific applications or to be used on a broader application range^{2,3}. Among the materials developed in the last decades, the nanocrystalline (NC) and amorphous materials, also known as metallic glasses (MG), figure as one of the most important to help in the development of societies in the coming decades¹.

Conventional polycrystalline metals, also known as coarse-grained materials, are usually composed of agglomerates of crystals with specific regions, namely grain core or grain for short, grain boundaries (GBs), and triple/quadruple junctions⁴. The atoms of grain cores exhibit an ordered and repeating lattice pattern defined by the unit cell of the crystal, where the usual crystalline pattern for most metals at room temperature are: body-centered cubic (BCC), face-centered cubic (FCC) and hexagonal close-packed (HCP)⁵. Grain boundaries correspond to the junction regions between two grains and usually exhibit a disordered structure, while the triple/quadruple junctions are regions where more than two grains meet⁶.

Nanocrystalline materials, by its turn, are a particular case of polycrystalline materials in which the grain size, i.e., the size of grain core, denoted by d , is smaller than 100 nm⁷. The interest of the scientific community regarding these materials did not start until the 1980's with the landmark works by Gleiter and Birringer⁸⁻¹⁰. Since then, NC materials have been subject to widespread research to better understand their unique properties, unusual behavior, and processing routes.

The reduction of grain size to such small values causes some interesting phenomena when compared to coarse-grained materials, such as increased strength/hardness¹¹, improved toughness⁹, reduced elastic modulus¹², enhanced diffusivity¹³, higher specific heat¹⁴, lower melting point¹⁵, and higher electrical resistivity¹⁶. Concerning the mechanical properties, the dislocation pile-up model and the Hall-Petch (HP) relationship are widely used to explain the behavior of NC materials. Dislocations are, along with point defects, the most common imperfections existing in nearly all crystals and also the main responsible for plastic deformation at room temperature for most metal¹⁷. Dislocations can usually slip inside a crystal if enough stress is provided and accumulate (pile-up) at some obstacles such as GBs, impurity atoms, second phases precipitates, or other dislocations^{9,18}. While the obstacles pin the

dislocations, the plastic deformation is prevented from progressing. However, for every accumulated dislocation, more stress is concentrated on the tip of the pile-up. At some point, the accumulated stress will be such that the obstacle will no longer hold the dislocation pile-up; consequently, the dislocations will overtake the obstacles continuing with plastic deformation on an adjacent grain. Considering a material with only GBs as obstacles, it was empirically demonstrated by Hall and Petch that its strength could be estimated using the following equation^{19,20}:

$$\sigma_y = \sigma_0 + k_1 d^{-1/2} \quad (1)$$

where σ_y is the yield stress, k_1 is a constant and σ_0 is approximately the yield stress of a very coarse-grained polycrystal²¹.

Considering Eq. (1) and the fact that nanoscale grain cores of NC materials imply an extremely high-volume GB fraction, it is clear that they present enhanced mechanical strength when compared to conventional materials²². However, several studies reported that below a critical grain size the yield stress deviates from the HP relationship, or even an inverse (or negative) HP relationship is observed, i.e., the material starts to lose strength as the grain size decreases²³⁻³⁰, as presented in Table 1.

Table 1 – Experimental results from literature for NC materials that present an inverse HP relationship.

Material	Grain size range studied (nm)	Critical grain size (nm)	[Ref.]
Pd	7–13	>13	[23]
Cu	8–16	>16	[23]
Cu	5–30	9	[24]
Cu	25–120	33	[25]
TiAl	10–700	21	[26,27]
NiZr	8–98	22	[28]
PdCuSi	4–110	10	[29]
FeCoSiB	6–120	25	[29]
NiMo	3.4–30	10	[30]

Source: Adapted from Song et al.²⁸, 1999.

The understanding of the phenomena responsible for the Hall-Petch relationship breakdown is not yet fully clear in the scientific literature. In the present thesis, the mechanical behavior and structural evolution of nanocrystalline metallic materials based on aluminum, nickel, and titanium are investigated by molecular dynamics to shed light on this challenging topic of physical metallurgy.

1 LITERATURE REVIEW

Chokshi et al.²³ were the first to report the inverse HP relationship, in the late 80's, for both Cu and Pd nanocrystals, by using hardness measurements in samples produced by the inert gas condensation method with grain sizes less than 16 nm. The authors suggested that the results were originated from the occurrence of rapid diffusion creep at room temperature by the transport of vacancies along the GBs, namely Coble creep phenomenon. However, shortly after, Nieman et al.³¹ also performed hardness measurements of Cu and Pd produced by the inert gas method with a similar grain size range and found no inverse HP effect; however, a flatter HP slope was observed. These two works mark the beginning of controversial results regarding the HP effect that extends to the present day.

Nanocrystalline materials can be processed by different techniques such as plasma processing, chemical vapor condensation, inert gas condensation, rapid solidification, electrodeposition, mechanical alloying, spark erosion, and sliding wear³². Nevertheless, regardless of the method used, flaws are often present, which may affect the resulting material's mechanical behavior³³. It is suggested that NC samples thermally treated from the as-produced condition may result in structural changes such as phase transformations, densification, stress relief, or grain growth, all of which can introduce errors into the experimental estimation of strength^{34,35}. Chokshi et al.²³ has indeed annealed the smallest grain size samples in order to obtain grain growth and therefore a range of grain sizes, whereas Nieman et al.³¹ processed all samples using the inert gas method, hence performing the hardness measurements in as-produced condition. Nevertheless, it is essential to notice that materials produced by the inert gas method present highly flaw sensitivity^{36,37}; hence, porosity and gaseous impurities can cause a significant change in mechanical behavior. However, it is by no means certain that inverse HP occurs only in heat-treated and not in as-prepared nanomaterials, since there are instances in the literature that show inverse HP for as-prepared materials³⁸⁻⁴².

Nanocrystalline alloys samples prepared using the electro deposition method often show significant composition changes with the grain size due to tendency of some soluble atoms such as C, S, or W to segregate at GBs⁴³. Thus, such changes in composition raise doubts about the analysis of grain size dependence. For instance, Trelewicz and Schuh⁴⁴ found an inverse HP relationship in a NC NiW alloy where the 3-150 nm grain size range was associated with alloy compositions ranging from 25 to 1 at. % W, respectively. The major difference in composition

might be responsible for the apparent HP breakdown and not the grain size. Nanocrystalline samples can also be produced by controlling the crystal growth from a glassy alloy⁴⁵. Notwithstanding, a thin amorphous layer can still be present after crystallization, affecting the grain size dependency analysis. Moreover, indentation testing in NC materials can also induce grain growth³⁵.

It is known that a large fraction of experimental observations about the inverse HP relationship can be associated to artifacts in sample processing⁶ and different measurement methods, e.g., hardness measurements, compressive tests, and tensile tests³⁴. Therefore, there is still no unambiguously evidence of the inverse HP relationship^{32,46}. That is why some researchers believe that it is factual and provide some theoretical explanations for its occurrence, while others consider that it is just an anomaly^{32,47}. Considering that the inverse HP effect is real, the basic premise to envision its occurrence in NC materials is that the classical dislocation pile-up model cannot occur in such small grain because the average dislocation spacing is close to the grain size^{48,49}. Thus, other deformation mechanisms may operate in this regime⁴³. Different models have been proposed to explain the inverse HP relationship, and most of them can be inserted into at least one of four categories: dislocation-based models^{50,51}, diffusion-based model^{52,53}, grain-boundary-shearing models⁵⁴, and two-phases model^{55,56}.

The dislocation-based model takes the conventional slip model and extends it to the NC materials taking into account the characteristic features of this regime. However, this leads to two main problems. First, it considers that the dislocations play the same role in nanograin as coarse grains⁵⁷. Studies revealed that this is energetically unfavorable^{58,59}. Second, experimental observations show paucity or absence of dislocations in NC materials⁶⁰⁻⁶².

The diffusion-based models consider that, even at room temperature, diffusional creep is operational and work as the dominant deformation mechanism in NC materials³⁸. Conventional diffusional creep was initially attributed by Nabarro⁶³ and Herring⁶⁴ to the mass transport of vacancies through the grains from one GB to another at high temperatures, $T \approx T_m$, where T_m is the melting temperature, as:

$$\dot{\epsilon} = \frac{D_{gc}\sigma b^3}{k_B T d^2} \quad (2)$$

where $\dot{\epsilon}$ is the strain rate, D_{gc} is the lattice diffusivity, σ is the applied stress, b is the Burgers vector magnitude, k_B is the Boltzmann constant and T is the temperature. In 1963, Coble⁶⁵ suggested that at lower temperatures, $T < 0.7 T_m$, the grain boundary diffusion (GBD) (diffusion of vacancies along GBs) is larger than through the grains. The author proposed that the strain rate in this case follows the relation:

$$\dot{\epsilon} = \frac{\beta D_{GB} \sigma b^4}{k_B T d^3} \quad (3)$$

where β is a constant and D_{GB} is the GB diffusivity. The stress in the Nabarro-Herring model is proportional to d^2 , whereas it is proportional to d^3 in the Coble model. As already mentioned, Chokshi et al.²³ were the first to suggest Coble creep as a deformation mode in NC solids. However, they showed that their results fit the relation $\sigma_y = \theta - K' \cdot d^{-1/2}$, where θ and K' are constants, instead of $\sigma_y \propto d^3$, which indicates that Coble creep was in fact not responsible for the plastic deformation. Also, their equation cannot be related to any known mechanism³⁸. However, Masumura et al.⁶⁶ proposed a generalization of the HP relationship based on the classical HP equation for large grains and Coble creep for smaller grains so that contributions from both mechanisms are considered. This model provides a reasonable fit for some experimental observations⁶⁷. These findings indicate that Coble's contribution to the plastic deformation in NC materials cannot be ignored.

The grain-boundary-shearing model considers the atomic shear events at GB and their implications in NC materials, being the grain boundary sliding (GBS) and grain rotation (GR) its main pillars. The GBS was initially proposed as a deformation mechanism of polycrystals at high temperatures and later extended to NC materials deformed at room temperature due to evidence of its occurrence⁶⁷⁻⁶⁹. The model describes the relative displacement of adjacent grains under stress due to mechanically or thermally activated single atomic jumps at or near GB⁷⁰. It is important to recognize the two types of GBS termed Lifshitz sliding⁷¹ and Rachinger sliding⁷². Rachinger sliding requires an accommodation by intragranular slip, i.e., it must be accommodated by some intragranular movement of dislocations within the adjacent grains. In contrast, Lifshitz sliding is an accommodation process for Nabarro-Herring and Coble diffusion creep^{9,73,74}. Grain rotation is also a well-known phenomenon for polycrystalline materials

deforming at high temperatures⁷⁵⁻⁷⁷ that was extended to model the plastic deformation in NC metals at room temperature⁷⁸⁻⁸⁰. In general, it is assumed that the driven force for GR is the energy gradient due to misorientation of the GBs that delineate a grain from its neighbors^{81,82}. There seems to be a consensus regarding the existence of GR in NC materials. The debate, in this case, is whether the GR is mediated by cross-grain gliding of a larger number of dislocations^{83,84}, diffusional creep^{85,86}, GBS^{87,88} or by the change in the content of GB dislocations^{83,89}.

The two-phases model was also primarily developed for polycrystalline materials and extended to the nanoscale⁹⁰. Often referred to as core-and-mantle model, it considers the NC material as a composite material composed of two phases: one being the GBs and the other the grain cores^{91,92}. The material's strength in this model varies with grain size according to⁹:

$$\sigma = \sigma_{GC} + k_2(\sigma_{GB} - \sigma_{GC})d^{1/2} - k_3(\sigma_{GB} - \sigma_{GC})d^{-1} \quad (4)$$

where σ_{GC} is the flow stress of dislocation-free grain core, σ_{GB} is the flow stress of the GB region, and k_2 and k_3 are free parameters. For coarse grains, the reciprocal square root term in Eq. (4) dominates the stress-strain relationship (classical HP dependence), whereas for smaller grains the reciprocal of grain size becomes important, reducing the HP slope⁴³.

The amorphous-limit model can also be mentioned here, in which the amorphous material is considered a limit-case of the NC material⁹³. This model arises from observations of similar deformation mechanisms between MGs and GBs. Although the fundamental mechanism of plasticity in amorphous solids is not yet fully resolved, one widely accepted theory is referred to as shear transformation zones (STZs)⁹⁴. These STZs are cluster of atoms, usually comprised of tens of atoms, that undergo collective displacement from their mean positions to accommodate local strain and relax the applied stress^{95,96}. At room temperature, and considering that the stress is sufficiently large, the STZs can evolve to a highly localized plastic flow known as shear bands^{95,97}. Similar concepts have also been applied to GBs^{93,98}. Thus, deformation mechanisms usually observed in amorphous materials may become essential to explain NC materials' behavior.

It is important to mention that crystalline and MGs materials are quite different concerning the atomic order ranges. Metallic glasses present a disordered atomic structure and are thermodynamically metastable solids⁹⁹. Long-range order (LRO) is typical of crystalline

materials, whereas it is absent in MGs. Nonetheless, short-range order (SRO) and even medium-range order (MRO) persist in amorphous alloys¹⁰⁰. Usually, the SRO corresponds to the local unit involving the nearest neighbor atoms. The MRO encompasses more considerable distances than the short-range of structural configuration; both atomic aggregates influence the MGs' mechanical properties.

The deformation of NC materials may also be a simultaneous action of different deformation mechanisms³⁸. Furthermore, the experimental data are usually not precise enough to allow one to select a concept from various theoretical models to fully describe the experimental data³⁸. An example of divergent experimental data for NC materials is present in Table 1 for Cu in which one work reports the critical grain size as 9 nm²⁴ whereas the other 33 nm²⁵.

The imprecise experimental data caused by the difficult in processing flaw-free NC samples associated with the progress in computational technology has created a great opportunity to study this class of materials using computational materials science. By definition, computational materials science is the computer-based tools employed in modeling and simulation to understand and predict the material's behavior¹⁰¹. The wide range of length and time scales that govern materials response creates a challenge to simulate them¹⁰². Table 2 presents a schematic view of both the length and time scale expected when simulating crystalline materials' mechanical behavior¹⁰³. Given the wide range of such scales, it is clear that no single modeling technique would work for all of them. Thus, different methods have been developed, which are also shown in Table 2, each one focused on a specific set of physical phenomena and appropriated times and lengths.

Table 2 – Length, time scale and methods usually employed in computational materials science to study crystalline materials.

Entity representation	Length scale (m)	Time scale (s)	Method
Complex structure	10^3	10^6	Finite element analysis
Simple structure	10^1	10^3	Finite element analysis
Grain microstructure	10^{-3}	10^{-3}	Monte Carlo
Dislocation microstructure	10^{-5}	10^{-6}	Monte Carlo
Atom	10^{-9}	10^{-12}	Molecular Dynamics/Monte Carlo
Electron orbitals	10^{-11}	10^{-15}	<i>Ab-initio</i>

Source: Adapted from Ashby¹⁰³, 1992.

Finite element analysis (FEA) subdivides a system into small elements, called finite elements, creating a geometric mesh¹⁰¹. Each of these finite elements is represented by a set of equations that must be combined into a global system of equations¹⁰⁴. This macroscale method can deal with systems of length and time scales relevant for engineering problems, including fracture mechanics, fatigue, wear, impact, penetration, and shock wave phenomena^{101,105}. However, processes taking place at a minimal length or time scale are not captured by this method.

The Monte Carlo method is based on statistical sampling and is usually applied when thermodynamic information of the system is required¹⁰². Monte Carlo approach can be summarized as: given a system with an initial spatial configuration p and energy U_p , a trial move is performed on the fundamental entities (which can be single atoms, group of atoms, dislocations and so on) to a new position $p + 1$. The energy in this new configuration, U_{p+1} , is calculated in such a way that if $\Delta U_{p,p+1} \leq 0$ then the trial move is accepted, otherwise, if $\Delta U_{p,p+1} > 0$ then the trial move will only be accepted based on a probability distribution, this process is then repeated until a certain criterion is met¹⁰². As can be noticed, the evolution of the position variables in Monte Carlo is not based on any physical model.

The *Ab-initio* methods, also known as first principles, are fundamentally useful because they do not require experimental input of material, except the corresponding atomic number¹⁰⁶. The calculation methods are based solely on the laws of Physics. Moreover, since this method considers the nuclei and electrons as the primary particles, electronic and magnetic properties can be obtained. The major drawback of this method is that it involves complex differential partial equations based on quantum mechanics to be solved^{101,106}, thus requiring considerably computational effort. Therefore, in most cases, the system is usually limited to hundreds or a couple of thousands of atoms. It is important to mention a remarkable progress recently achieved by Jia et. al.¹⁰⁷ in this field. They managed to simulate more than 1 nanosecond-long trajectory of over 100 million atoms per day using a machine learning protocol called Deep Potential Molecular Dynamics while retaining *Ab-initio* accuracy. This achievement required and massive computational resources; they used the entire Summit supercomputer, which figures as the second-fastest supercomputer in the world with a peak performance of 200 PFLOPS (it held the number 1 position from November 2018 to June 2020)¹⁰⁷.

Classical molecular dynamics (MD) simulations, hereafter referred to as MD, is one of the most used techniques for modeling and simulation in materials research¹⁰². It was also one of the first computer-based methods employed in studying the properties of materials dating

back to the 1950s^{108,109}. Working with solids the MD can be used to investigate phase transitions, phase equilibrium, defect formation and migration, elastic and plastic mechanical properties, grain boundaries, grain growth, dislocations, motion of interfaces, and much more^{101,102}.

Unlike the first-principles method, the MD considers atoms as rigid spheres and disregards nuclei and electrons¹¹⁰. Thus, the system can be described by Newton's equations of motion, in order that the acting force, \vec{F}_i , considering it to be conservative, on atom i can be expressed as¹⁰⁶:

$$\vec{F}_i = m_i \vec{a}_i = m_i \frac{d\vec{v}_i}{dt} = m_i \frac{d^2\vec{r}_i}{dt^2} = -\nabla_i U(\vec{r}_1, \vec{r}_2, \dots, \vec{r}_N) = -\nabla_i U(\vec{r}_1, \vec{r}_2, \dots, \vec{r}_N) \quad (5)$$

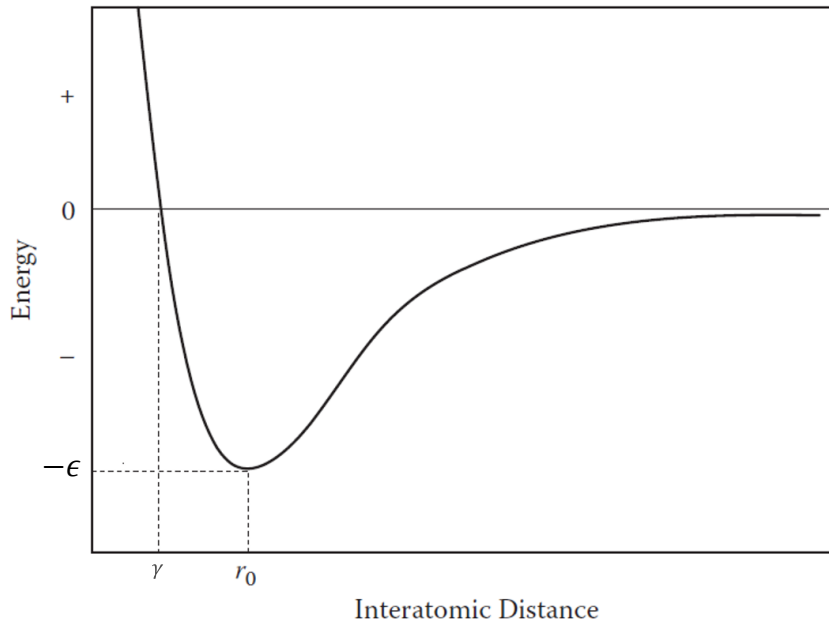
where m_i is the atomic mass, \vec{a}_i is the acceleration vector, \vec{v}_i is the velocity vector, \vec{r}_i is the position vector, ∇_i is the gradient, and $U(\vec{r}_1, \vec{r}_2, \dots, \vec{r}_N)$ is the potential energy as a function of the position of the particles for N atoms (interatomic potential). From Eq. (5), it is possible to note that the force acting on an atom at a given time can be obtained solely by the interatomic potential, which is a function of the position of all atoms. This kind of potential energy, and also the simplest, can be express as the Lennard-Jones potential, also called pair potential¹⁰²:

$$U(\vec{r}_1, \vec{r}_2, \dots, \vec{r}_N) = \frac{1}{2} \sum_{i=1}^N \sum_{j=1}^N ' \varphi_{ij}(r_{ij}) \quad (6)$$

$$\varphi_{ij}(r_{ij}) = 4\epsilon \left(\left(\frac{\gamma}{r_{ij}} \right)^{12} - \left(\frac{\gamma}{r_{ij}} \right)^6 \right) \quad (7)$$

where the single quotes (') indicates that the terms in which $i = j$ are not included in the sums, the distance between atom i and j is $r_{ij} = |\vec{r}_j - \vec{r}_i|$ and the potential between them is denoted by $\varphi_{ij}(r_{ij})$, γ is the distance at which the potential is zero and ϵ is the lowest energy of the potential curve as shown in Figure 1.

Figure 1 – Schematic of the Lennard-Jones pair potential.



Legend: r_0 is the equilibrium interatomic distance.
 Source: Adapted from Lee¹⁰⁶, 2012.

Although useful to describe some properties of rare-gas solids, the Lennard-Jones potential is often not a good description of the atomic interactions in most metallic materials^{102,111}. A more appropriate potential to this goal is the Embedded-atom method (EAM), in which the basic idea is to add an energy function of the local electron density into the pair potential as follows¹⁰²:

$$U_{EAM} = \frac{1}{2} \sum_{i=1}^N \sum_{j=1}^N \phi_{ij}(r_{ij}) + \sum_i M_i \left[\sum_{j \neq i} f_{ij}(r_{ij}) \right] \quad (8)$$

where f is some function of the interatomic distance representing an approximation of the electron density, and M is a functional of a sum over functions that depends on the local positions of the atoms. Since M is a non-linear function, it cannot be written as a sum of pair potentials. The Eq. (8) is a general form of the EAM model; however it has many variations of it and the exact form depends on which model and assumptions one uses. For instance, in the original EAM model^{112,113}, M represent the energy to embed an atom i in a uniform electron gas of density $\bar{\rho}_i$, which can be approximated as a sum of contributions of the electron densities, $\rho_e(r_{ij})$ ¹⁰²:

$$\bar{\rho}_i = \sum_{j \neq i} \rho_e(r_{ij}) \quad (9)$$

Therefore, the form of this EAM potential is:

$$U = \frac{1}{2} \sum_{i=1}^N \sum_{j=1}^N \phi_{ij}(r_{ij}) + \sum_i M_i(\bar{\rho}_i) \quad (10)$$

Generally, the functions F , $\bar{\rho}_i$ and ϕ depend on parameters that are usually determined by fitting the model to experimental values or *Ab-initio* ones.

As aforementioned, with the correct application of an interatomic potential, the force \vec{F}_i on the atom i , and consequently \vec{a}_i , can be found. The next step would be to calculate \vec{v}_i and \vec{r}_i . However, the model used in MD simulation as it is, using Newton's laws of motion to describe the movement of rigid spheres (atoms), results in the N -body problem. This problem was originated in the dynamics of the solar system and it was shown that it does not have an analytical solution for three or more bodies¹¹⁰. Therefore, MD simulations rely on numerical methods to find \vec{v}_i and \vec{r}_i . One of the most frequently used method for this purpose is the velocity Verlet algorithm¹⁰⁶, which is based on the finite-difference method, i.e., it advances in time by discrete intervals denoted by δt , called timesteps. The velocity Verlet algorithm yields reasonably high-quality simulations due to its stability and accuracy^{102,114}. With a known set of positions and velocities, the recurrence relation of the velocity Verlet algorithm has the form^{106,115}:

$$\vec{r}_i(t + \delta t) = \vec{r}_i(t) + \vec{v}_i(t)\delta t + \frac{1}{2m_i} \vec{F}_i(t)\delta t^2 \quad (11)$$

$$\vec{v}_i(t + \delta t) = \vec{v}_i(t) + \frac{1}{2m_i} \left(\vec{F}_i(t) + \vec{F}_i(t + \delta t) \right) \delta t \quad (12)$$

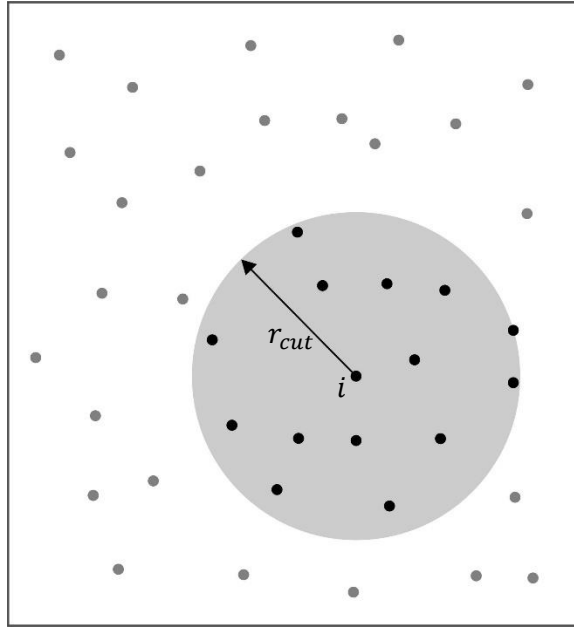
Finally, a usual MD simulation can be summarized in the following steps:

- Using a given potential, the forces on all atoms are computed.
- With $\vec{a}_i = \vec{F}_i/m_i$ the accelerations are calculated.
- \vec{v}_i and \vec{r}_i are then numerically calculated at later time, $t + \delta t$, using finite-difference methods.
- Using The values obtained in the previous steps are used in the next iteration, and the process is repeated until an arbitrary stopping criterion is met.

One of the main limitations of MD is the spatial and temporal scales. The former limitation arises from the number of atoms required to represent a system, which is extremely high even for microscopic elements. For this reason, the systems in MD are usually limited within the nanometer scale. Even so, the atomic force evaluation considering the influence of all atoms in the system is unattainable¹¹⁶. Long-range interaction, which is outside a given cut-off radius, r_{cut} , is discarded and only atoms within this radius is considered in the force calculation as depicted in Figure 2. The temporal limitation occurs due to the timestep. If a large timestep is used the atomic motion becomes unstable and the structure of the system are no longer representative¹¹⁷. Reversely, if an extremely low timestep is used the simulation will not be efficient due to a very long calculation time¹¹⁸. A widely accepted way to set a proper timestep is considering the shortest vibrational period in the system¹⁰². For solids, the shortest period is typically of the order of a picosecond. Considering the Verlet algorithm, it normally requires a timestep of the order of 50 timesteps per vibrational period to obtain sufficient accuracy for energy conservation^{102,119}. Thus, the timestep is usually set to $10^{-15} - 10^{-14}$ s.

Another MD limitation is the interatomic potential. The development of an appropriated interatomic potential is not an easy task¹²⁰. Although interatomic potentials have been developed for many elemental materials, there is a significant lack of reliable potentials for alloys¹²⁰, especially for ternary or more complex systems¹²¹. However, significant advances in this field have amde during the last decade, especially using machine learning¹²².

Figure 2 – Schematic of potential cut-off in two dimensions.



Legend: Black and gray dots represent atoms that are within and outside the cut-off radius, respectively.

Source: The author, 2021.

In a MD simulation, the equivalent thermodynamic variables of the system, such as temperature and pressure, P , can be calculated by averaging them over time as¹⁰²:

$$\langle T \rangle = \frac{2\langle K \rangle}{3Nk_B} \quad (13)$$

$$\langle P \rangle = \frac{N}{V} k_B \langle T \rangle - \frac{1}{3V} \left\langle \sum_{i=1}^N \vec{r}_i \cdot \nabla_i U \right\rangle \quad (14)$$

where $\langle \rangle$ indicates average over some time period, N is the number of atoms, K is the kinetic energy, and V is the system volume. A standard MD simulation with a fixed number of atoms (N), volume (V) and total energy (E_T) is said to be in a microcanonical ensemble, or NVE. In this ensemble, the system is thermodynamically isolated. The equilibrium value of kinetic energy, and thus the temperature, is typically very different from the initial set value since the

atoms relax away from their initial positions. If the goal of simulation is to model a system under specific temperature conditions, which is often required to compare with experiments, then the NVE ensemble is limiting. The Nosé-Hoover method¹²³ makes possible simulations in the canonical ensemble (NVT) in which N , V and T are kept fixed. The Nosé-Hoover introduces some dynamic variables coupled with particle velocities that represent a connection of the system to some reservoir of energy. Hence, when the temperature is dropped from a determined value, some kinetic energy is added to the system and every time the temperature exceeds the desired value, the kinetic energy is removed, thus maintaining the system at a fixed temperature¹⁰². Like the Nosé-Hoover, the Parrinello-Rahman method¹²⁴ introduces new variables that couple the simulation cell to an external force, thus the pressure can be maintained at a given value. Using the Nosé-Hoover and Parrinello-Rahman methods the system can be simulated in the isobaric-isothermal ensemble (NPT), in which N , P and T are kept constant.

2 SCOPE AND OBJECTIVES

This work aims to get a better understanding of the mechanical behavior of NC materials, studying the influence of grain size on the mechanical properties and deformation mechanisms while verifying the influence of the interatomic potential and possible limitations of the MD model itself. To this end, three different NC systems are studied: Al₈₀Ti₁₅Ni₅ alloy, Ni, and Al. The Al₈₀Ti₁₅Ni₅ alloy was chosen due to its good ductility, high mechanical resistance, and low specific mass, with remarkable technological applications¹²⁵. Moreover, as far as we know, there is no record in the literature concerning mechanical behavior of this alloy using MD with an EAM potential. Concerning the Ni, a comprehensive analysis regarding deformation mechanisms is made. Although several MD studies regarding Ni mechanical behavior already exist in the literature¹²⁶⁻¹³⁹, the adopted conditions, construction sample techniques, or analysis methods are different from the present work, thus introducing novel contributions. Moreover, the grain size range covered in this work is larger than the cited works, making it possible to study systems inside the inverse HP relationship and also systems respecting the conventional HP relationship. Lastly, the Al system is studied to verify the connection between the inverse HP relationship and dislocation activity via the strain hardening test.

3 METHODOLOGY

There are different open-source codes for MD simulations, being GROMACS¹⁴⁰ and LAMMPS¹⁴¹ the two most used¹⁴². The latter was chosen to be used in this work because it has several advantages when dealing with hard matter such as metals¹⁴². For instance, some potentials, such as Tersoff¹⁴³ and COMPASS¹⁴⁴, are implemented in LAMMPS but not in GROMACS. However, GROMACS is largely used in the study of biomolecules. The version of LAMMPS used in this work was continuously updated throughout the years, starting on 17/Jan/2017 until 29/Oct/2020 version.

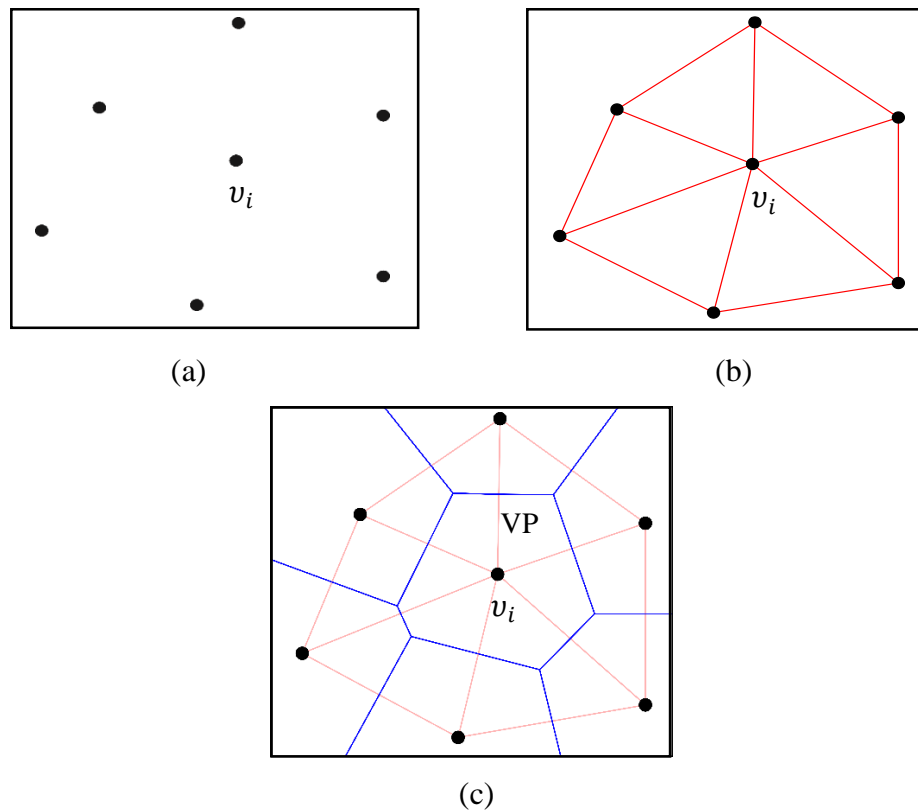
Creating nanocrystal systems with LAMMPS can be a tricky task, especially when there is a need for many grains, which may lead to defective systems. Therefore, it was decided to use the open-source software AtomsK¹⁴⁵ to this end. The AtomsK allows excellent control over the geometry and the system properties. The construction of systems using AtomsK followed, basically, these steps: determination of the simulation box dimensions; creation of a unit cell to be used as a seed; insertion of a specific quantity of seeds in the simulation box; and expansion of the seeds using the Voronoi tessellation^{146,147}. After the creation of the system, their data file is then loaded into LAMMPS to start the MD simulation.

In the Voronoi tessellation method, a set of points $\vec{v}_1, \vec{v}_2, \dots, \vec{v}_n$ is placed at given positions within an Euclidean space. The Voronoi polyhedron (VP) around a given point, \vec{v}_i , is the set of points in the space closer to \vec{v}_i than to any other point¹⁴⁸. Seeds of unit cells are placed at each point and then expanded to fill its Voronoi polyhedron. The required steps to create a VP, using two dimensions as example, can be described as^{149,150}:

- Points are introduced in the space, Figure 3(a).
- Points are linked to their nearest neighbors, red lines in Figure 3(b).
- The midpoints for each redline are found.
- Perpendicular bisectors for each red line are constructed, blue lines in Figure 3(c). These blue lines define the GBs of the future grains, while the Voronoi polyhedron represents the grain interiors.

Usually, the initial spatial positions of each point and the unit cell orientations are randomly generated. This choice allows the production of samples closer to reality.

Figure 3 – Creation of a Voronoi polyhedron.



Legend: (a) Random points inside a space, (b) connections between the nearest points (red lines), (c) perpendicular bisectors (blue lines).
Source: The author, 2021.

For all samples, periodic boundary conditions were applied in all Cartesian directions to remove surface effects. Moreover, the time step was set as 1.0 fs and stresses at orthogonal directions to the tensile axis were zeroed during deformation. The energy minimization at 0 K was performed using the Polak-Ribiere version^{151,152} of the conjugate gradient method. The post-processing analysis was performed using the following tools: Common Neighbor Analysis (CNA)¹⁵³, Voronoi analyses¹⁵⁴, and Dislocation Extraction Algorithm (DXA)¹⁵⁵ as implemented in the OVITO package¹⁵⁶, Grain Tracking Analysis (GTA)¹⁵⁷, and LAMMPS X-ray diffraction under copper $K\text{-}\alpha$ radiation. For visualization, atoms were colored according to their atomic arrangement in the following way: green for FCC, red for HCP, blue for BCC, and gray for unknown coordination structure. The specific methodology for each of the systems will be given next.

3.1 Al₈₀Ti₁₅Ni₅ Alloy

Two NC samples containing five and eight grains, both with Al₈₀Ti₁₅Ni₅ composition, were generated with an initial volume of $15 \times 15 \times 20 \text{ nm}^3$, consisting of 271,829 atoms each sample. The samples with five and eight grains had an average grain size of 12 and 10 nm, respectively, hereafter referred to as d12 and d10 samples. The alloy's final stoichiometry was obtained by inserting Ni and Ti atoms randomly into the Al matrix as substitutional solutes. After energy minimization the samples were relaxed at 300 K for 10 ps under the NPT ensemble. Also, an amorphous sample was created having as starting material the d10 structure. Initially, the d10 sample was heated from 300 to 2300 K (above melting temperature) at a heating rate of 10 K.ps^{-1} . Subsequently, the sample was maintained at 2300 K for 10 ps under the NPT ensemble to stabilize the liquid. Finally, the sample was cooled to 300 K under the cooling rate of 40 K.ps^{-1} and again stabilized at this temperature for 10 ps. This procedure is similar to that reported in the study of Cu-Zr-Al alloys¹⁵⁸.

The atomic interactions were modeled using the EAM potential. However, due to the absence of a true ternary potential for the AlTiNi alloy, we used a ternary potential parameterized by the RAMPAGE method proposed by Ward et al.¹⁵⁹. This method for build binary or higher-order potentials starts from well-fitted elemental potentials available in the literature. The interaction between elements of the same species are taken in unchanged form from their original sources. The only functions required to be fitted to form a full alloy potential are the cross-potential terms, i.e., the interactions between different elements. Details about the method can be found elsewhere¹⁵⁹⁻¹⁶¹. The AlNiTi system's potential has utilized unary potentials reported by Zhou et al.¹⁶². Each potential used is available at NIST Interatomic Potentials Repository tabulation¹⁶³.

All samples were submitted to uniaxial tensile tests performed with a strain rate of $1.0 \times 10^{10} \text{ s}^{-1}$ at 300 K. The tensile testing was conducted until 0.15 strain.

3.2 Nickel

The simulated Ni samples have a volume of $30 \times 30 \times 40 \text{ nm}^3$ and approximately 3.3×10^6 atoms. The grain sizes studied were 3.2, 4.7, 6.0, 8.7, 15.0, 20.4, and 24.1 nm. The number

of grains in the samples ranges from 5 to 2000, depending on the average grain size. The atomic interactions were modeled using the EAM potential parameterized by Myshin et al.¹⁶⁴.

After energy minimization, an initial temperature of 200 K was set and then scaled to 300 K over 50 ps under the NPT ensemble. Subsequently, the samples were relaxed at 300 K for 10 ps under the same NPT ensemble, a sufficient time to obtain steady-state energy values and no observable microstructural changes. Uniaxial tensile tests were performed after relaxation by straining the simulation box parallel to the edge with 40 nm with an engineering strain rate of $1.0 \times 10^{10} \text{ s}^{-1}$. Snapshots were regularly stored for detailed analysis at several strains. The deformation was carried out until 0.15 strain. At least three different runs were conducted for each grain size to obtain a standard deviation of the mechanical properties. Repeated stress relaxation tests were carried out under the NPT ensemble for 2.5 ps for each cycle with a total of four cycles. The starting point of stress relaxation was at 0.035 strain.

Rida et al.¹⁶⁵ reported that the use of a strain rate higher than $5.0 \times 10^5 \text{ s}^{-1}$ for 2D samples does not allow the system to reach the equilibrium state. Thus, some mechanical properties that usually do not vary with the strain rate start to depend on it. While it is true that strain rates above this critical value may alter some mechanisms, this strain rate is utterly unrealistic for most studies of 3D nanocrystals using MD. Moreover, a compromise between grain size, volume, and strain rate has to be considered. For the grain size range used in this work, and taking into account the findings of Rida et al.¹⁶⁵, the $1.0 \times 10^{10} \text{ s}^{-1}$ strain rate should essentially activate the same deformation mechanisms that would be seen using $1.0 \times 10^9 \text{ s}^{-1}$, with just a small difference in yield and ultimate strength.

3.3 Aluminum

Aluminum NC samples were generated using a region of $15 \times 15 \times 20 \text{ nm}^3$ and 271,708 atoms. In total, four NC samples with different numbers of grains were generated. The average grain sizes are 14.2, 11.9, 9.4, and 8.2 nm for samples with 3, 5, 10, and 15 grains, respectively. The systems were relaxed at 300 K under the NPT ensemble for 10 ps. Subsequently, the uniaxial tensile test was performed at a strain rate of $1.0 \times 10^9 \text{ s}^{-1}$.

After the tensile test, the 10 and 15-grain samples were chosen to perform a strain hardening study since they have the smallest average grain sizes, and therefore the grain boundary effects would be enhanced. The strain hardening study was performed by loading the

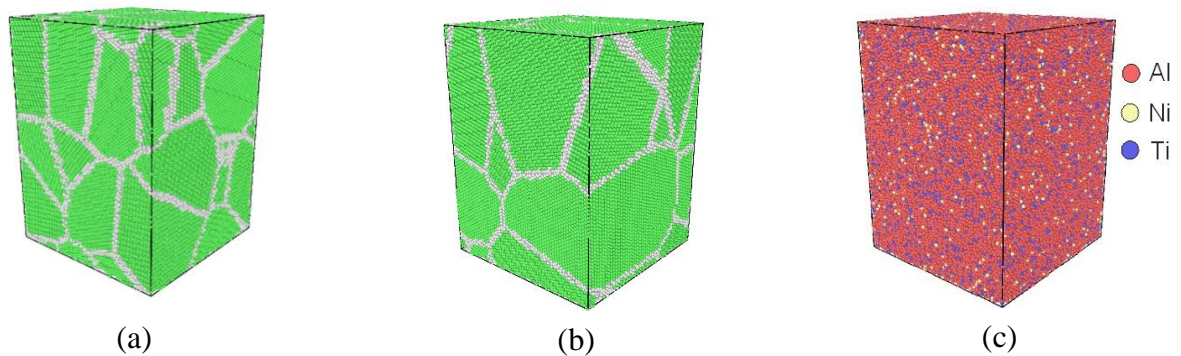
samples until deformation of 0.06 (beyond the elastic deformation), unloading, and loading one last time. The strain hardening was performed under the same temperature and strain rates used in the tensile test.

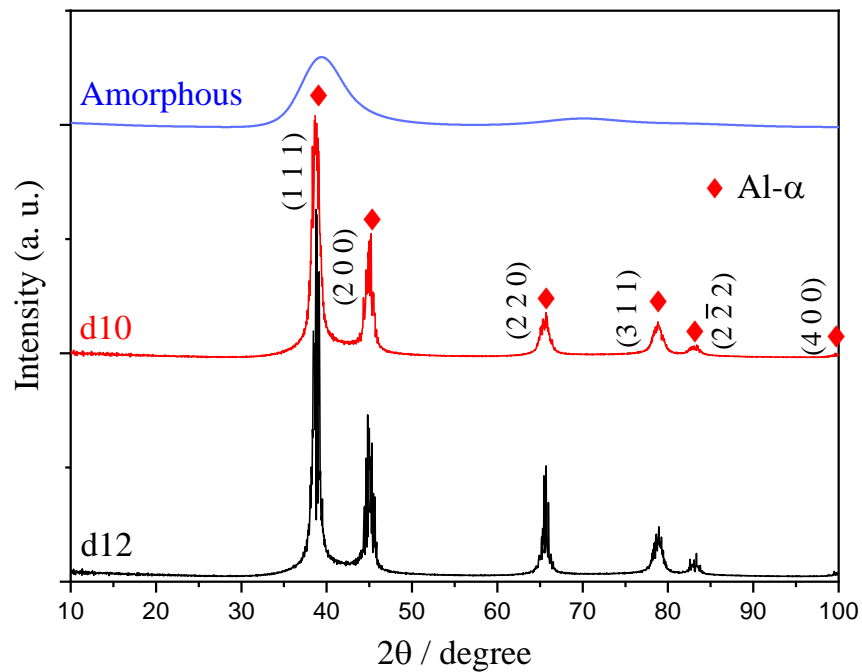
4 RESULTS AND DISCUSSION

4.1 $\text{Al}_{80}\text{Ti}_{15}\text{Ni}_5$ Alloy

Figure 4(a-c) shows the snapshots at 300 K of the samples studied, and the corresponding X-ray diffraction patterns are depicted in Figure 4(d). Diffraction peaks corresponding to Al- α crystalline planes are shown in the diffractograms of d10 and d12 samples, where no clear peaks of secondary phases were observed, indicating that all atoms of Ni and Ti elements are inserted into the Al structure as a solid solution. Also, the peak intensities of the d12 sample are slightly higher than those of d10, reflecting the influence of grain size on X-ray diffraction intensities. As to the amorphous sample, the massive halo around 40° in Figure 1(d) is typical of a completely glassy structure, in agreement with X-ray diffraction data reported in Kim et al.¹⁶⁶ for some alloys of the studied ternary system.

Figure 4 – Simulated structures of $\text{Al}_{80}\text{Ti}_{15}\text{Ni}_5$ alloy and X-ray diffraction pattern.





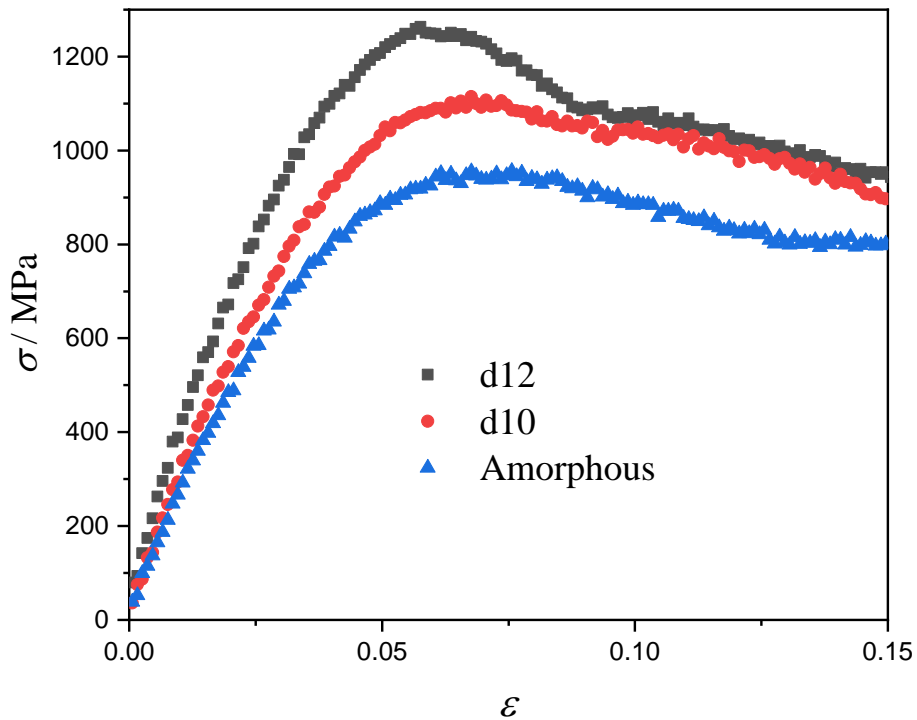
(d)

Legend: (a) d12 and (b) d10 samples. Green atoms refer to FCC structure, and white atoms are those located at grain boundaries. (c) Atomic distribution of amorphous material. (d) Simulated X-ray diffraction patterns of NC and amorphous samples

Source: The author, 2021.

The simulated uniaxial stress-strain curves are shown in Figure 5. A higher ultimate tensile stress (UTS), σ_u , and yield stress are observed for the NC structure compared to the amorphous one. The UTS is reached at about 0.07 strain for the amorphous and d10 samples, denoting a tensile strength of approximately 950 MPa and 1100 MPa, respectively. For the d12 sample, UTS is reached with $\epsilon \approx 0.06$ and 1260 MPa. The UTS values follow an inverse Hall-Petch relationship and are relatively close to experimental values of extruded samples of $\text{Al}_{88.5}\text{Ni}_8\text{Ti}_{3.5}$ alloy with 865 MPa¹⁶⁷.

Figure 5 – Simulated tensile test for $\text{Al}_{80}\text{Ti}_{15}\text{Ni}_5$ alloy at a strain rate of $1.0 \times 10^{10} \text{ s}^{-1}$.



Source: The author, 2021.

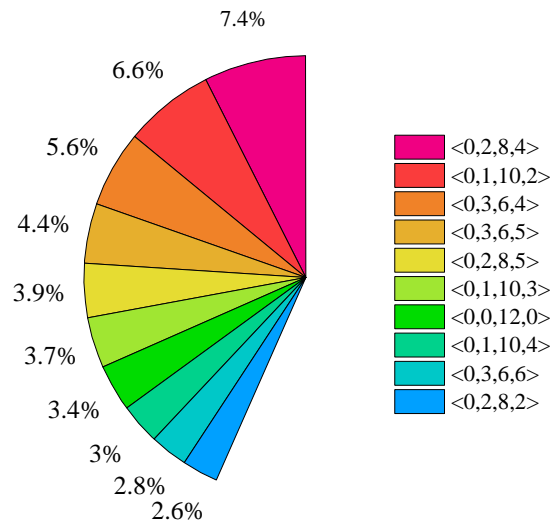
The Young's modulus (E) is obtained from the slope of linear region on the stress-strain curve corresponding to the elastically deformed material. The modulus calculation from the simulation data must include enough data points for a reliable fitting. For this reason, a strain smaller than 0.03 was used to estimate the elastic moduli, resulting in 21.2, 24.7, and 28.8 GPa for the amorphous, d10, and d12 samples, respectively. It is well established for coarse-grained materials that E have low sensitivity to the grain size¹⁶⁸. However, the obtained results showed a dependency between E and the atomic structure. This type of dependence was also reported in the work of Xu and Dávila¹⁶⁹ for NC aluminum. Considering that GB regions are elastically softer than the crystalline grain interior¹⁷⁰, the reduction of E with grain size can be explained by the large volume fraction of GB possessed by the NC materials. Thus, the MGs could indeed be considered a limit-case of NC materials (in which the grain size tends to zero), as already reported for Cu and Cu–Zr based alloy^{93,170}. Nevertheless, the elasticity moduli are lower than the reported for NC Al¹⁷¹. This quantitative inconsistency can be ascribed to the interatomic potential, as further discussed in Section 4.1.3.

4.1.1 Amorphous Al₈₀Ti₁₅Ni₅ deformation mechanisms

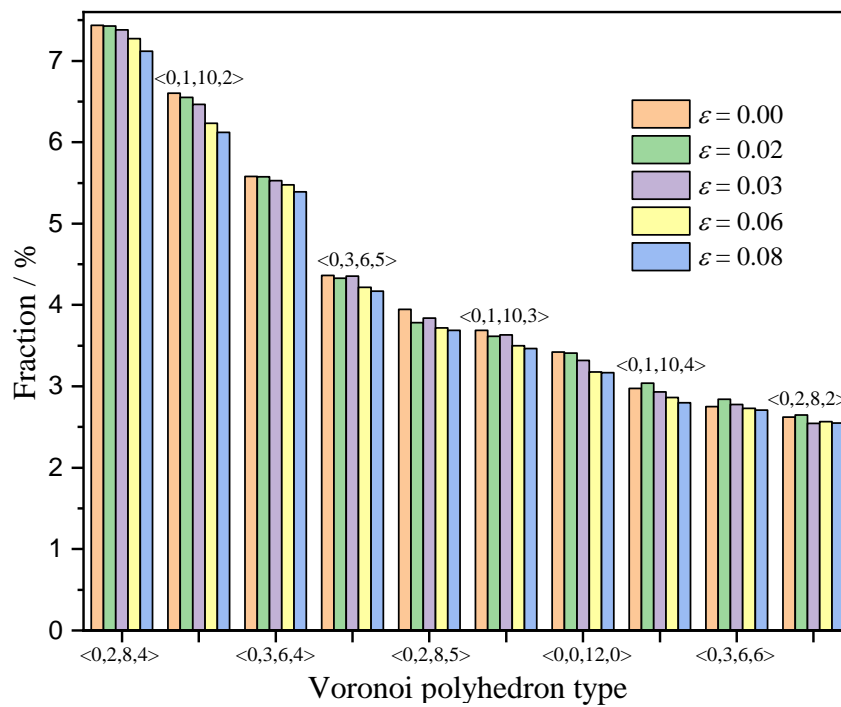
One of the most used methods to analyze the atomic distribution in disordered structures is the pair distribution function that provides a statistical distribution of atoms around a central atom¹⁷². Although the pair distribution method is an essential analytical tool, it cannot provide accurate information about the three-dimensional atomic configuration. A proper method to analyze the SRO in amorphous structures is the Voronoi tessellation technique. Each Voronoi polyhedron is defined by a set of indices $\langle n_3, n_4, n_5, \dots \rangle$ where n_i denotes the number of i -edged faces of the Voronoi polyhedron around a center atom. In this work, we considered the ten most abundant VP present in the amorphous structure where $\langle 0,2,8,4 \rangle$, $\langle 0,2,8,2 \rangle$, $\langle 0,1,10,4 \rangle$, $\langle 0,1,10,3 \rangle$, $\langle 0,1,10,2 \rangle$ correspond to distorted icosahedral clusters and $\langle 0,0,12,0 \rangle$ is the perfect icosahedra. The polyhedrons $\langle 0,3,6,4 \rangle$ and $\langle 0,3,6,5 \rangle$ are characteristic of FCC-like clusters, and the BCC clusters are represented by $\langle 0,3,6,6 \rangle$ and $\langle 0,2,8,5 \rangle$. Figure 6(a) shows the fraction of VP existing at 300 K in the Al₈₀Ti₁₅Ni₅ amorphous alloy. Other clusters are occasionally present, but they were not considered in this study due to their small population. The medium-range order is roughly based on the VP clusters, such as the Zr-centered $\langle 0,2,8,5 \rangle$ polyhedrons, which form an interpenetrating network strongly affecting the mechanical behavior of Cu-Zr based MGs¹⁷³. In this study, the MRO relies mainly on the distorted icosahedra's interconnection, where the $\langle 0,2,8,4 \rangle$ VP likely has a greater tendency to form an interpenetrating network.

It is recognized that the local atomic structures change during tensile deformation, i.e., the strain modifies the SRO and MRO¹⁷⁴. Thus, the VP evolution as a function of applied strain was analyzed, as shown in Figure 6(b). The polyhedrons $\langle 0,0,12,0 \rangle$ and $\langle 0,1,10,2 \rangle$ were the ones that suffered the greatest change, being reduced 7.6 % and 7.3 % in relation to their initial configuration, respectively. These changes in atomic configuration caused by shear can be related to the origin of the increased atomic mobility or the starting of STZ. The decreasing population in icosahedral clusters during tensile deformation are in good agreement with those reported for Mg-Zn-Ca alloys¹⁷⁵.

Figure 6 – Voronoi polyhedron analysis.



(a)



(b)

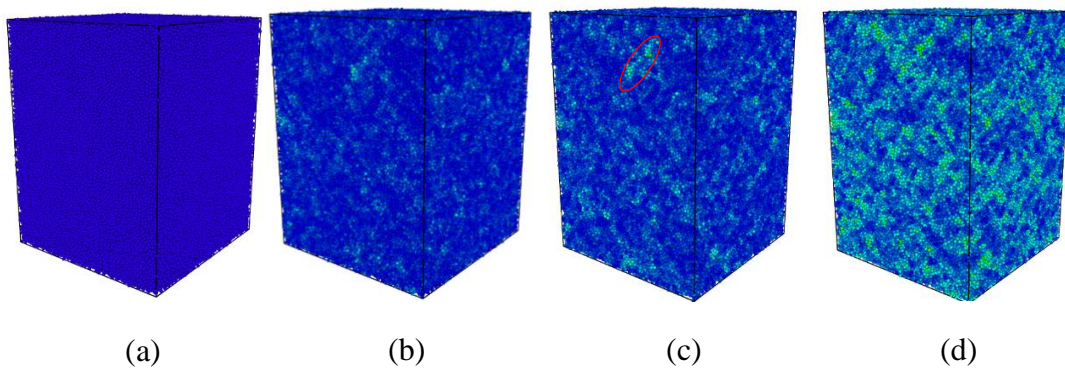
Legend: (a) Ten main VP (clusters) present in $\text{Al}_{80}\text{Ti}_{15}\text{Ni}_5$ amorphous alloy at 300 K and without plastic deformation. (b) Evolution of VP with the deformation.

Source: The author, 2021.

Figure 7 presents snapshots of the atomic-level deformation for some strain stages for the $\text{Al}_{80}\text{Ti}_{15}\text{Ni}_5$ amorphous sample. Figure 7(a) shows the sample without strain as a reference structure. As the stress level increases, the first STZ start to appear. Also, there are many small

regions with a high level of strain distributed homogeneously in the volume of the sample, as shown in Figure 7(b). As the deformation goes on, the quantity and extension of the STZs are increased, as depicted in Figure 7(c). Most STZs present an inclination of about 45 degrees, and some of them coalesce, evolving to shear bands (Figure 7(d)).

Figure 7 – Structural evolution of the amorphous sample



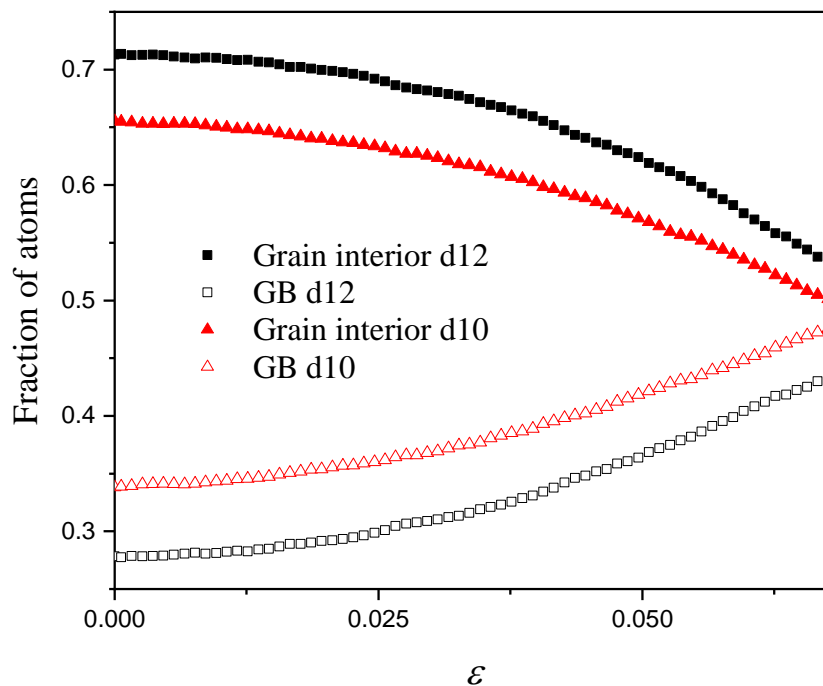
Legend: (a) $\varepsilon = 0.00$, (b) $\varepsilon = 0.02$, (c) $\varepsilon = 0.04$, (d) $\varepsilon = 0.08$. The colors blue and green represent low and high stress, respectively. Red ellipse shows a region of high deformation.

Source: The author, 2021.

4.1.2 Nanocrystalline $\text{Al}_{80}\text{Ti}_{15}\text{Ni}_5$ deformation mechanisms

Due to the small grain sizes, the $\text{Al}_{80}\text{Ti}_{15}\text{Ni}_5$ NC samples behave clearly within the inverse HP regime. The atoms are distributed in the interior of grains and the grain boundaries, as shown in Figure 8. The quantity of atoms identified as GB increases with the strain. On the other hand, the fraction of atoms in the interior of grains reduces with the strain. This behavior means that mass transport occurs from the grain interior to GB, induced by stress. The relative fraction of atoms at the grain interior is higher for the d12 sample than for d10, as expected.

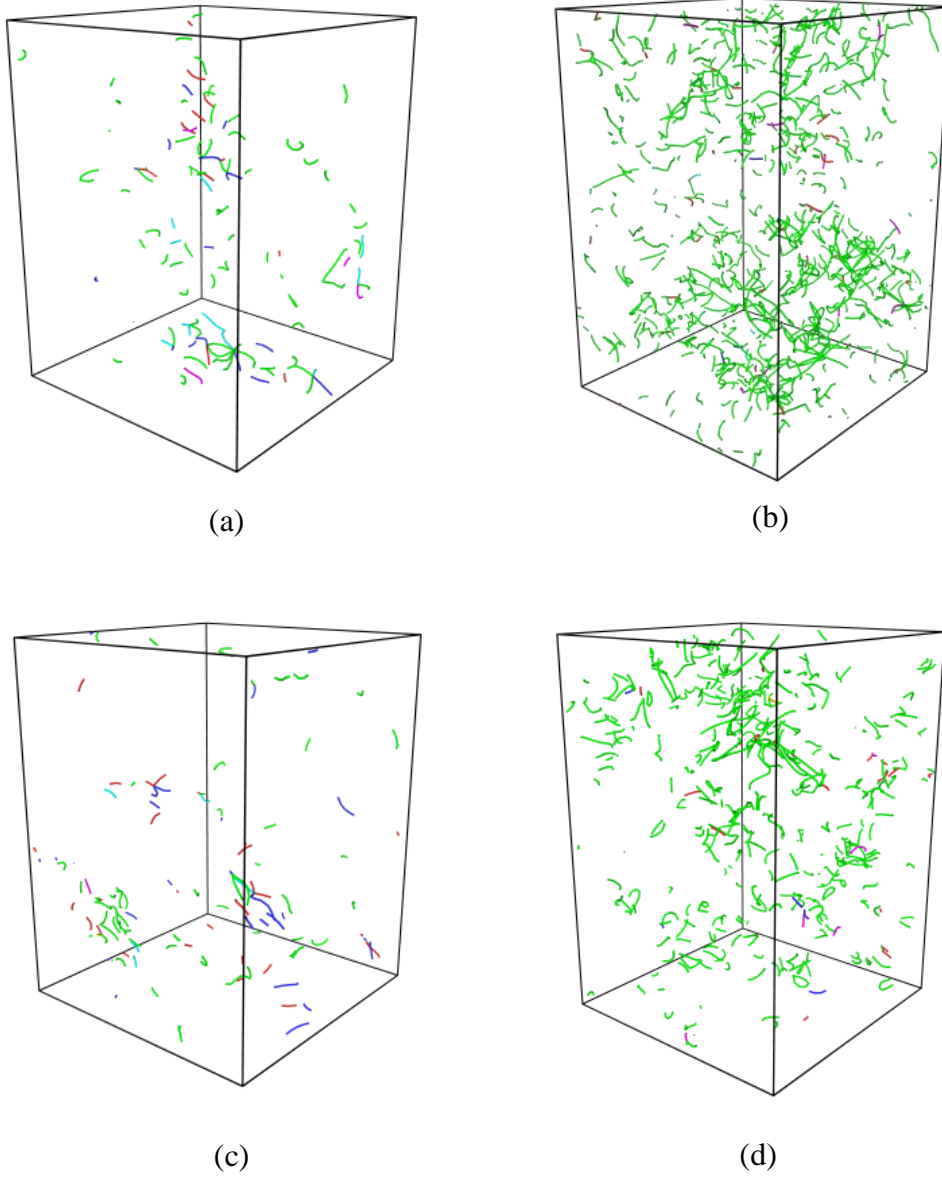
Figure 8 – Atomic fraction related to strain for the nanocrystalline samples.

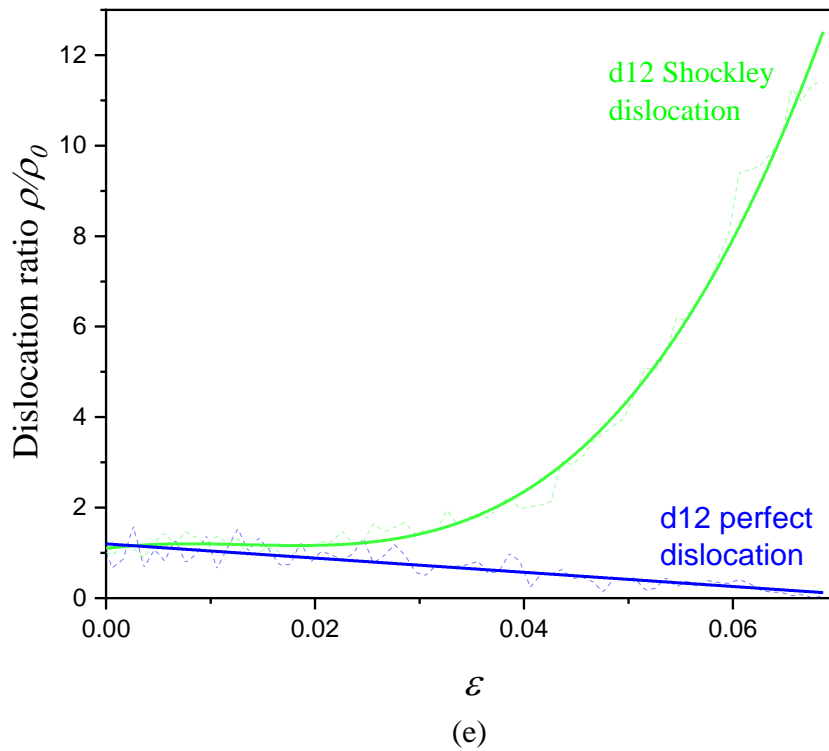


Source: The author, 2021.

To investigate the dislocation dynamics of NC samples, it was used the Dislocation Extraction Algorithm¹⁵⁵, which has the function of evaluating the dislocation density for different strains. Figure 9(a–d) shows the dislocation segments at 0.00 and 0.06 strain. Frank and Stair-Rod dislocations are present, but their quantities are negligible in comparison with Shockley partials. Perfect dislocations are present just in a small amount at the beginning of deformation and decrease linearly with the strain. However, Shockley partials grow exponentially, as shown in Figure 9(e) for the d12 sample. The parameter ρ is the dislocation density at a given strain, ρ_0 denotes the initial density, and the dislocation ratio is expressed as ρ/ρ_0 . The behavior of the d10 sample is similar, except for exhibiting a final dislocation ratio of about half compared to d12. Regardless of the sample (d10 or d12), the observed increase of Shockley partials with strain is relatively low. The existing perfect dislocations are dissociated into two Shockley partials or absorbed by the GBs, both processes reducing its density. This fact shows that in nanocrystals there is a transition from full dislocation slip to partial dislocation slip with the decreasing size of crystals.

Figure 9 – Dislocation evolution under different strains.



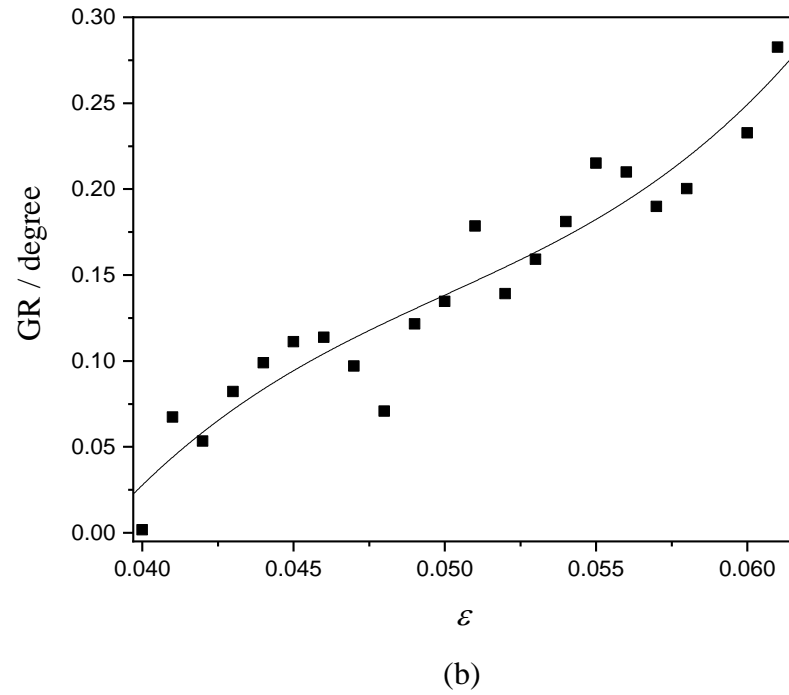
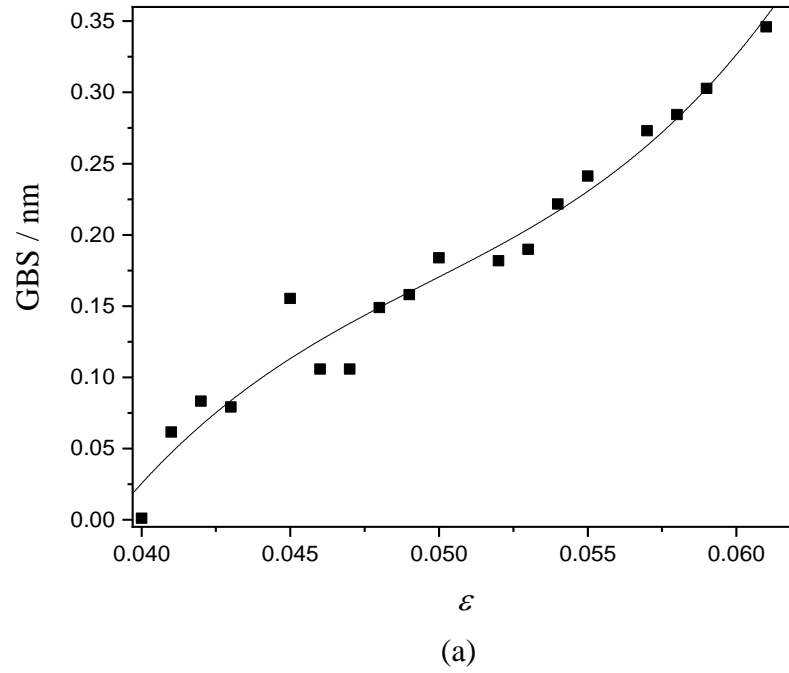


Legend: d12 sample: (a) 0.00 and (b) 0.06 strain. d10 sample: (c) 0.00 and (d) 0.06 strain. The colors green, dark blue, light blue, and purple represent Shockley, perfect, Frank, and Stair-Rod dislocations, respectively, whereas red segments are non-identified dislocations. (e) Normalized dislocation density plotted for d12 sample.

Source: The author, 2021.

As early mentioned, deformation mechanisms usually found in conventional polycrystalline materials at elevated temperatures, such as GBS, GBD, and GR, may be activated at room temperature in NC materials. To assess whether these phenomena were present in the current NC samples, we used the GTA algorithm¹⁵⁷. Figure 10 shows the results for the GBS and GR analysis for the d12 sample. These values are the average over the five grains. The GTA processing is an intense time-consuming algorithm; hence, the analysis was only performed for the d12 sample and limited to the strain range of 0.040-0.061, where these phenomena are expected to be more pronounceable. Surprisingly, the results show almost no rotation of the grains concerning their initial configuration ($\epsilon = 0.040$). This result may be caused due to the stress fields around the solute atoms. Moreover, GBS seems to have an essential contribution to the overall strain. Considering the 12 nm grain size, the GBS displacement of 0.340 nm yields a GBS strain of 0.028, almost half of the total strain 0.061. It is a worthy note that although GBS and GBD are two different phenomena, both of them contribute to the global strain, since the diffusion affects the GBS and *vice-versa*¹⁷⁶.

Figure 10 – Grain tracking analysis for the d12 sample.



Legend: (a) Grain boundary sliding and (b) grain rotation. The black lines are the polynomial fit.

Source: The author, 2021.

4.1.3 Influence of interatomic potential

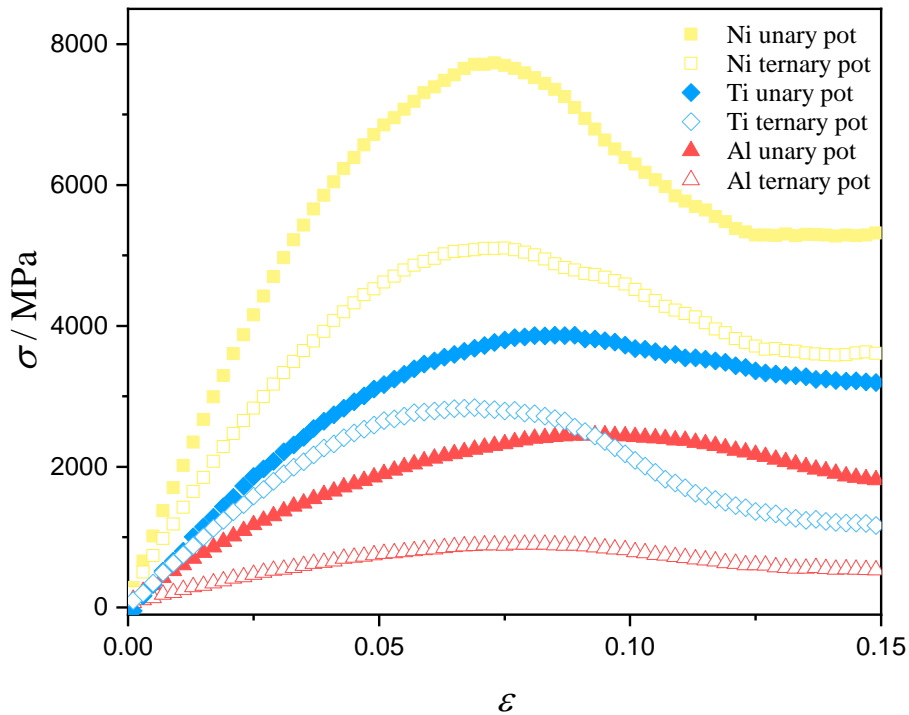
Although a decrease in the elastic modulus is expected within the nanometer regime, the elastic modulus values found in the previous sections can be considered below the expectations. The interatomic potential is crucial in an MD simulation; thus, it is reasonable to consider it as responsible for these low values. Since the experimental tensile test with the ternary composition used here is not available in the literature for comparison, to the best of our knowledge, we decided to study the elements that compose the alloy separately. To this end, it was created an aluminum, nickel, and titanium specimens with a mean grain size of approximately 10 nm. These single element samples were simulated using the same criteria as described in Sections 3.1. The unary potentials used for nickel, aluminum and titanium are reported in Mishin et al.¹⁶⁴, Mendeleev et al.¹⁷⁷, and Mendeleev et al.¹⁷⁸, respectively. The stress-strain results are Shown in Figure 11 and the elastic moduli in Table 3. The data indicate a deficiency from the ternary potential to reproduce the elastic moduli of pure elements. As expected, the unary potentials are adequate to produce elastic constant for pure elements. Therefore, the E values obtained for the $\text{Al}_{80}\text{Ti}_{15}\text{Ni}_5$ alloy samples were, indeed, affected by the ternary potential. However, it is important to remark that the RAMPAGE method does not aim to find the "best-in-class" potentials but to allow the rapid evolution of the alloy potential¹⁵⁹. Depending on the system, and the related phenomena, the RAMPAGE method can provide accurate results comparable to the best potentials available or, as in the present work, it can deviate from the experimental results. Nonetheless, MD simulations of alloys that do not have true potentials deserve studies to shed light on the complex phenomena inherent in nanocrystalline and amorphous materials, but its results must be carefully assessed.

Table 3 – Elastic modulus using unary and ternary potentials. The experimental values of nanocrystalline materials are present for comparison.

	Elastic modulus / GPa		
	Unary potential	Ternary potential	Experimental [Ref.]
Al	49	18	60 [171]
Ni	171	118	177 [179]
Ti	83	65	93 [180]

Source: The author, 2021.

Figure 11 – Stress-strain curves for Al, Ni and Ti with $d \approx 10$ nm using unary and ternary potentials.



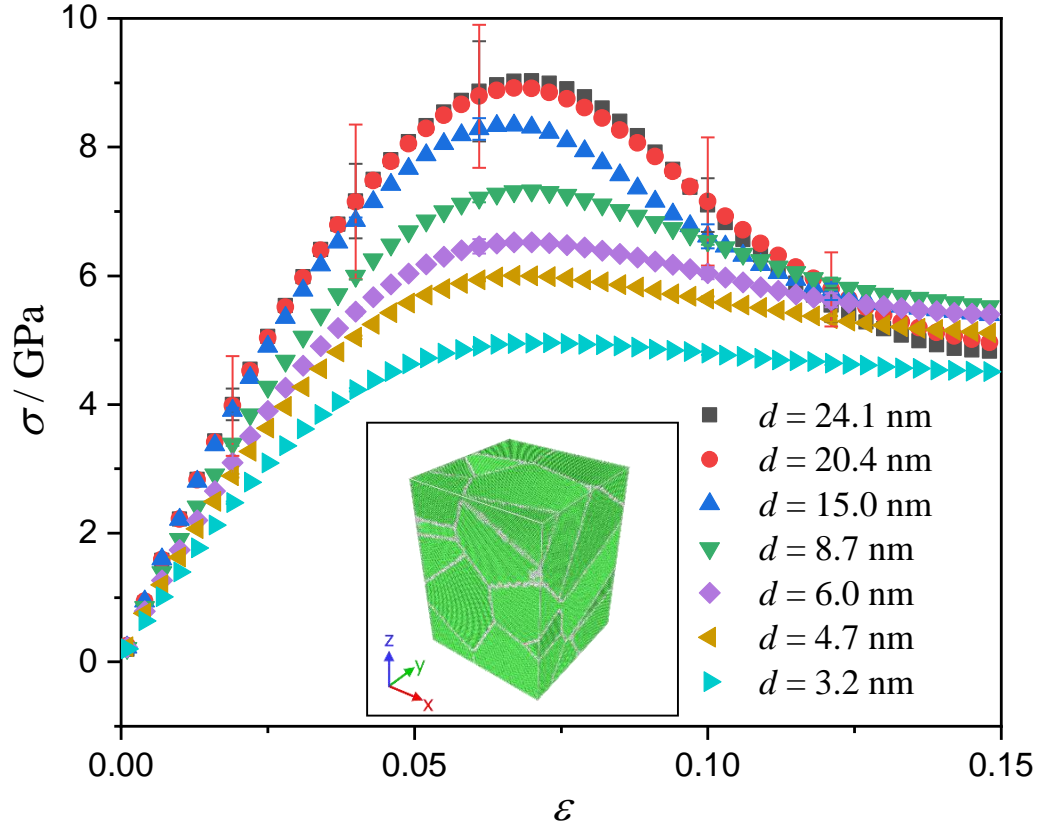
Source: The author, 2021.

4.2 Nickel

4.2.1. Effect of grain size on mechanical properties

The stress-strain curves of NC Ni samples are shown in Figure 12. The results reveal the presence of an inverse HP relationship. The yield stress was obtained at 0.002 offset strain. The Young modulus has been calculated for $\varepsilon \leq 0.02$. The samples with the largest grain sizes (24.1 and 20.4 nm) presented higher stress standard deviation because the few grains they possess causes moderate texture and consequently anisotropy. Table 4 shows the general mechanical properties.

Figure 12 – Stress-strain curves for nanocrystalline Ni at $1.0 \times 10^{10} \text{ s}^{-1}$ strain rate.



Legend: The standard deviation bars are presented in all curves, but for some samples, the values are too small to be seen. Inset: atomic configuration of nanocrystalline nickel with an average grain size of 24.1 nm after relaxation at 300 K. The atoms are colored by the CNA method.

Source: The author, 2021.

Table 4 – Mechanical properties related to the grain size.

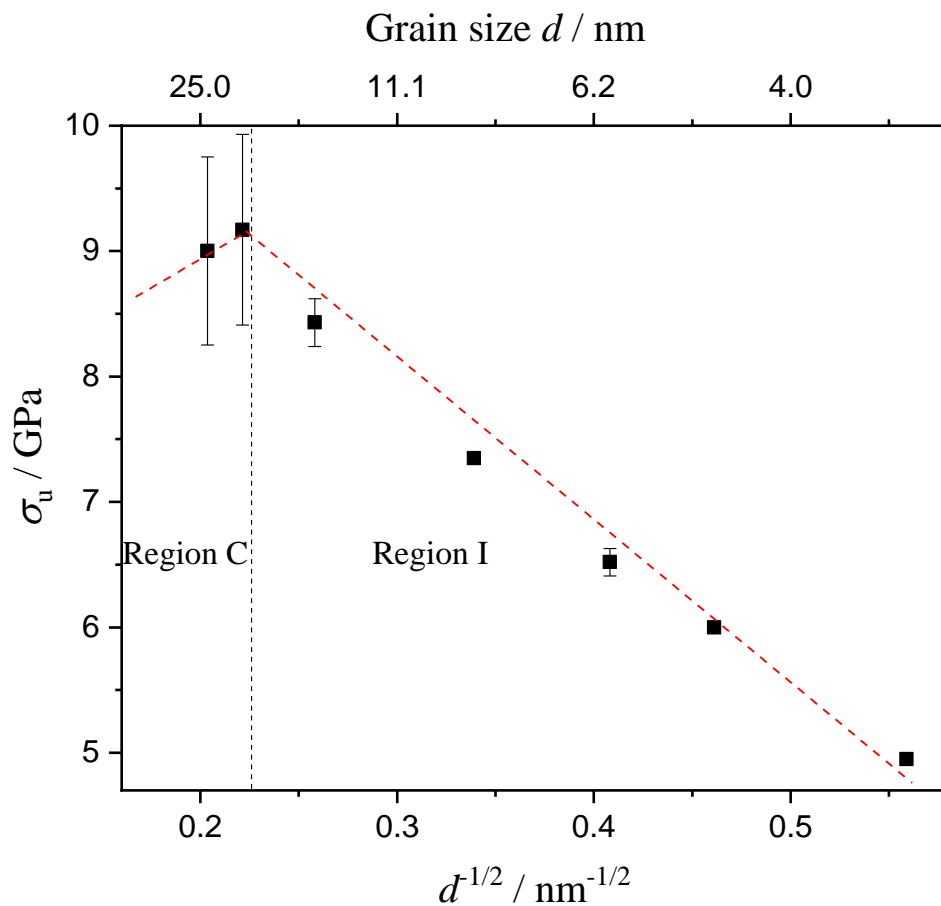
d / nm	3.2 ± 0.1	4.7 ± 0.3	6.0 ± 0.2	8.7 ± 0.2	15.0 ± 0.1	20.4 ± 0.1	24.1 ± 0.2
E / GPa	124.3 ± 1.4	146.0 ± 1.5	156.4 ± 1.2	172.5 ± 2.2	201.0 ± 0.9	205.0 ± 36.1	209.3 ± 12.2
σ_u / GPa	4.9 ± 0.1	6.0 ± 0.1	6.5 ± 0.1	7.3 ± 0.1	8.4 ± 0.2	9.2 ± 0.8	9.0 ± 0.8
σ_y / GPa	3.3 ± 0.1	4.0 ± 0.1	4.4 ± 0.1	4.6 ± 0.1	5.3 ± 0.1	5.7 ± 0.7	5.4 ± 0.5

Source: The author, 2021.

The relation between σ_u and the reciprocal of square root grain size $d^{-1/2}$ is shown in Figure 13, where two regions can be bounded: one following the conventional HP relation

(Region C), and the other related to the inverse HP relation (Region I). The critical average grain size is about 20 nm. This result is consistent with experimental results by Cho et al.¹⁷⁹.

Figure 13 – Ultimate stress dependence on grain size for Ni.



Legend: Red dashed lines are a visual guide representing the conventional and inverse HP relation. The vertical dashed line separates the data into two regions according to the HP behavior. For some points, the standard deviation is very low and, therefore, the amplitude of the error bar is very small and, therefore, cannot be visualized.

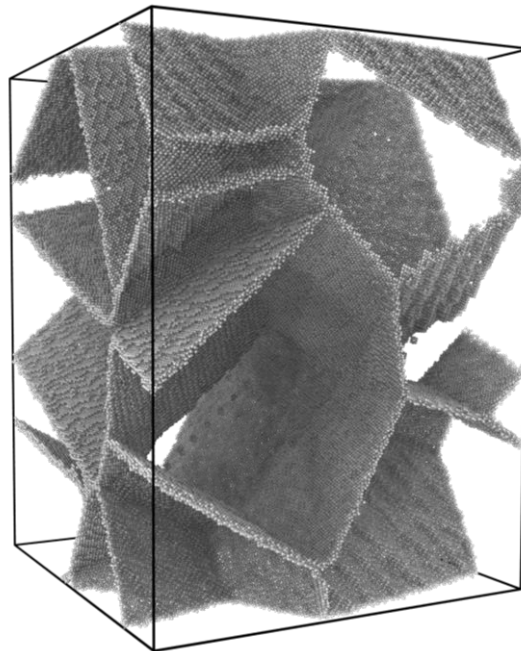
Source: The author, 2021.

4.2.2 Deformation behavior for sample with $d = 24.1$ nm

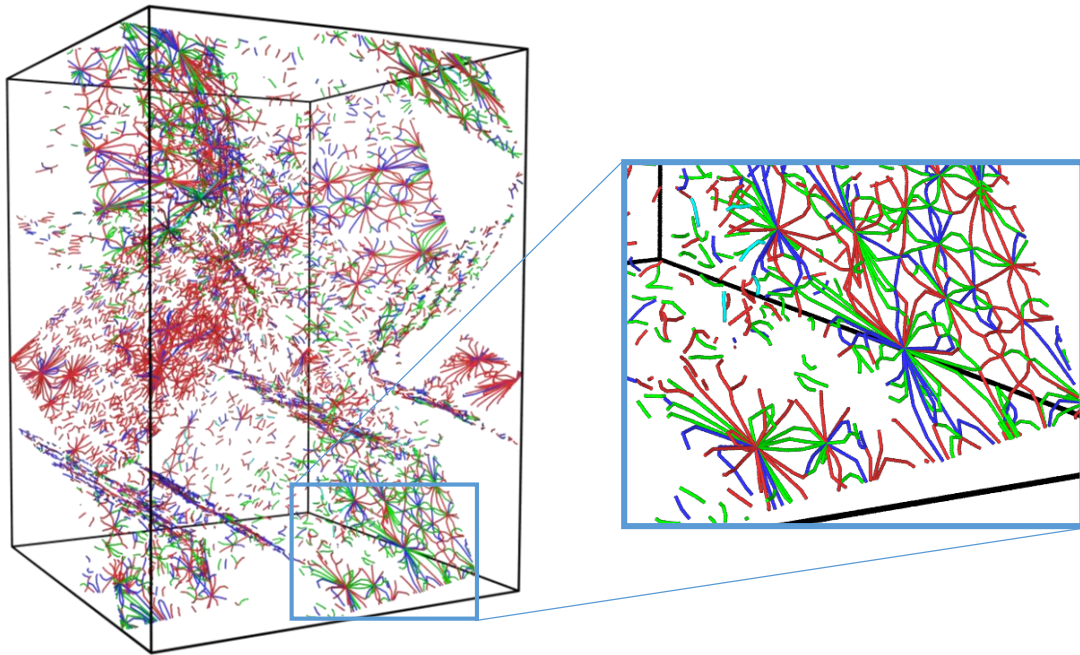
Two samples were chosen from the NC Ni deformation analysis, one representing the conventional ($d = 24.1$ nm) and the other the inverse ($d = 8.7$ nm) HP relationship. For the 24.1 nm average grain size sample, no perfect dislocations were observed in grain interiors

during straining. However, several dislocations were trapped inside GBs, including perfect dislocations, as shown in Figure 14. These perfect dislocations can dissociate into two Shockley partials, namely leading partial and trailing partial, separated by an equilibrium distance. A few extended dislocations were nucleated from triple junctions, where the leading partial creates the stacking fault and the trailing removes it, producing the fault ribbon between them, as shown in Figure 15.

Figure 14 – Dislocation segments for the sample with $d = 24.1$ nm at zero strain computed using the dislocation extraction algorithm.



(a)

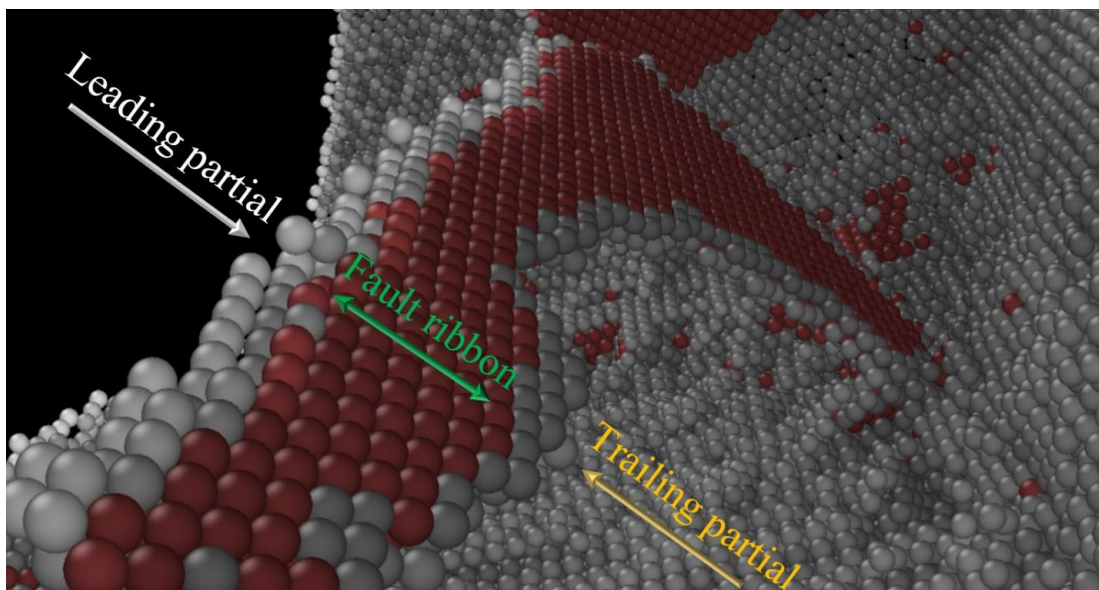


(b)

Legend: (a) The sample without atoms in FCC structure. (b) Same as (a) but removing all atoms, letting only the dislocation segments and a zoom to ease visualization. The segments colored as blue, green, cyan and red represents perfect, Shockley, Frank, and unknown dislocations, respectively.

Source: The author, 2021.

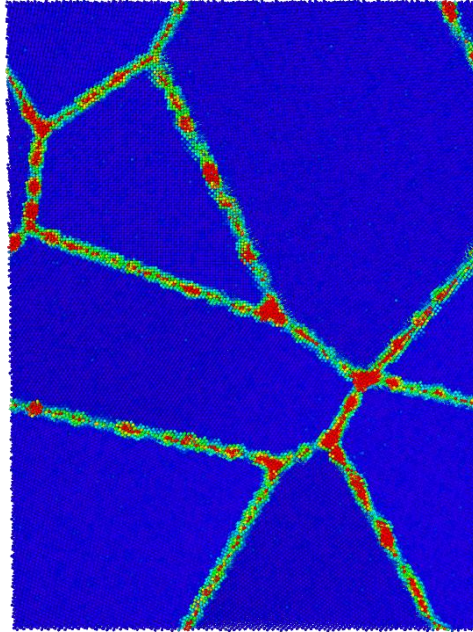
Figure 15 – Two partial dislocations separated by a fault ribbon forming an extended dislocation. Atoms of the FCC structure were removed to ease the visualization.



Source: The author, 2021.

It is important to notice that a real dislocation-free bulk crystal is virtually impossible to exist because dislocations are introduced during the crystal growing process. They can be present in the ‘seed’ crystals used to initiate the growth, be nucleated due to internal stresses created by impurity particles, or by a collision of different growing interfaces¹⁷. On the other hand, the construction of simulated samples using Voronoi tessellation does not imply the growth of crystals, and they can be impurity-free, which avoids the possibility of dislocation nucleation during the sample building. Furthermore, it does not include defects other than GBs, which occurs naturally given the necessity of wrapping atoms inside the volume. Since the crystal is defect-free, no significant rearrangements were observed during energy minimization and thermal equilibrium in grain interiors. Hence virtually all changes occurred in GBs, as can be seen in Figure 16, where the local minimum non-affine displacement¹⁸², D_{min}^2 , was used to avoid displacements related to atomic vibration. Moreover, considering a dislocation-free material with a high stacking fault energy, such as Ni, which obeys the conventional HP relation, it is crucial to understand why perfect dislocations were not nucleated during the straining test. We initially analyze the homogeneous nucleation of dislocations, representing the multiplication of a dislocation in a region of the crystal without defects. The resolved shear stress, τ_h , necessary to nucleate a dislocation, in this case, is $\tau_h \approx G/10$, where G is the shear modulus¹⁷. For the sample with $d = 24.1$ nm, $\tau_h \approx 8.0$ GPa. Considering the existence of a slip plane in this sample with a maximum Schmid factor, $m_s = 0.5$, and a yield stress of 5.4 GPa, the resolved shear stress in that plane would be $\tau_p = 2.7$ GPa, which is not enough to start homogeneous nucleation. Even considering the ultimate strength of 9.0 GPa the resolved shear stress would not reach τ_h . Another way to nucleate dislocations relies on stress concentrators. In this case, the required stress is $\tau_c \approx G/33$, resulting, for the $d = 24.1$ nm sample, in $\tau_c \approx 2.4$ GPa. This value is lower than τ_p , thus, theoretically, dislocations could be nucleated in this way. However, this model considers the existence of some barriers in the crystal lattice, like precipitates, inclusions, surface irregularities, flaws, cracks etc., that are not found in the studied samples. For this reason, this model cannot be applied to our samples.

Figure 16 – A slab with thickness of 2.0 nm from the 24.1 nm nanocrystalline sample colored according to the local minimum non-affine displacement D_{min}^2 .



Legend: The non-affine displacement intensity increases from colors blue, green, yellow to red.

Source: The author, 2021.

An important mechanism to generate dislocations is the Frank-Read (FR) source¹⁸³. The FR model considers a dislocation held at two points at a distance L that responds to an applied resolved shear stress by bowing out. With increasing stress, the dislocation reaches a critical configuration of a semicircle with a R_c radius, where $R_c = L/2$. This critical configuration requires stress, τ_{crt} , given by¹⁸³:

$$\tau_{crt} = \frac{\xi Gb}{R_c} \quad (15)$$

The parameter ξ reflects the dislocation character ($\xi = 0.5$ for edge and $\xi = 1.5$ for screw dislocation). Since most dislocations possess a mixed character, $\xi = 1$ was used.

When a perfect dislocation is dissociated, it is possible to find conditions where the leading partial becomes glissile, whereas the trailing partial moves very slowly or even do not move at all¹⁸⁴. In these cases, the stress required for a leading partial, τ_l , to reach the critical semicircle configuration is¹⁸⁴:

$$\tau_l = \frac{\xi G b_l}{R_l} + \frac{\gamma_s - F_{lt}(R_l^{-1})}{b_l} \quad (16)$$

$$F_{lt} = \frac{G b_l^2}{4\pi R_l} \quad (17)$$

where γ_s is the stacking fault energy, b_l and R_l are the Burgers vector magnitude and the radius of the leading partial, respectively, and F_{lt} is the interaction force per unit length acting between leading and trailing partial dislocation. After the release of the leading partial, both $F_{lt}(R_l^{-1}) \rightarrow 0$ and $\alpha G b_l/R_l \rightarrow 0$ as R_l expands. Thus, basically, after the emission of the leading partial, the applied stress to allow slip across the grain only needs to overcome:

$$\tau_l^* = \frac{\gamma_s}{b_l} \quad (18)$$

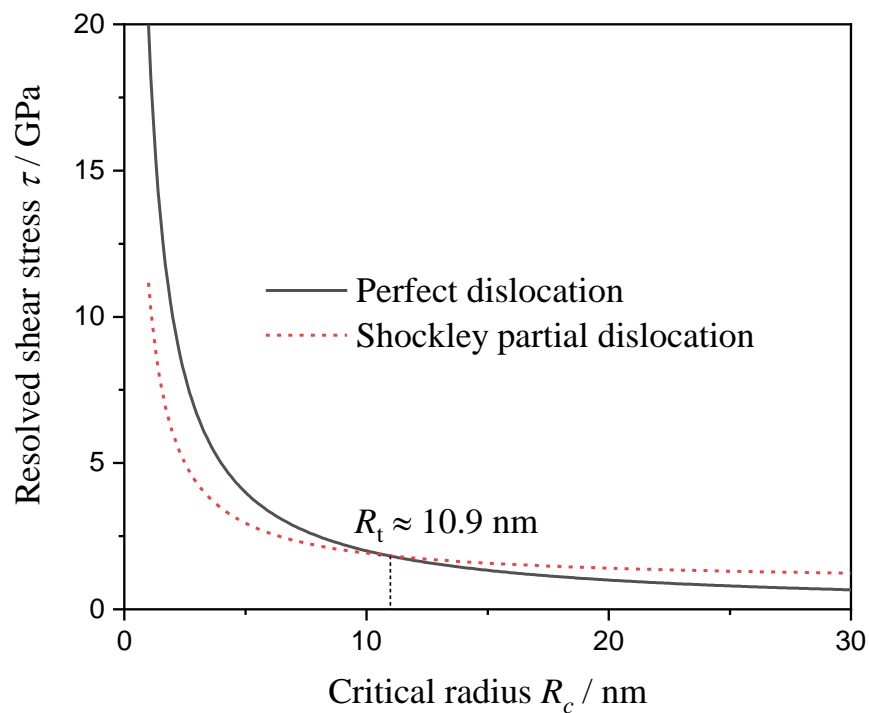
For the $d = 24.1$ nm sample, $\tau_l^* \approx 0.9$ GPa easing the partial dislocation traveling.

Figure 17 shows the behavior of Eq. (15) and Eq. (16). It is possible to notice an intersection point where the abscissa represents the radius, R_t , and consequently the grain size where it is expected to occur a transition from perfect dislocation to Shockley partial emission for nanocrystalline Ni. Since $R_t \approx 10.9$ nm, the length of anchor points is $L_t \approx 21.8$ nm. This analysis was made considering a dislocation emission from the GB and a hexagon-shaped grain. Hence, the transition length, L_t , has to be one of the sides of the grain. Therefore, the grain size expected to occur the transition from perfect to partial dislocations is $d \approx 37.7$ nm.

Unfortunately, the resources required to reach this grain size, applying the same procedures in this work, is exceptionally high, exceeding the operational capacity of the equipment we have at our disposal. Nevertheless, $d \approx 37.7$ nm should mark the grain size where a deviation from the conventional HP is observed. The experimental work of El-Sherik³⁹ reported an HP slope deviation for Ni at $d \approx 39$ nm. Therefore, the nucleation of perfect dislocations is indeed very unlikely to occur in the present conditions. This conclusion is coherent with an experimental nanoindentation study of Ni single crystal, which showed no perfect dislocation nucleation, but only partials¹⁸⁵.

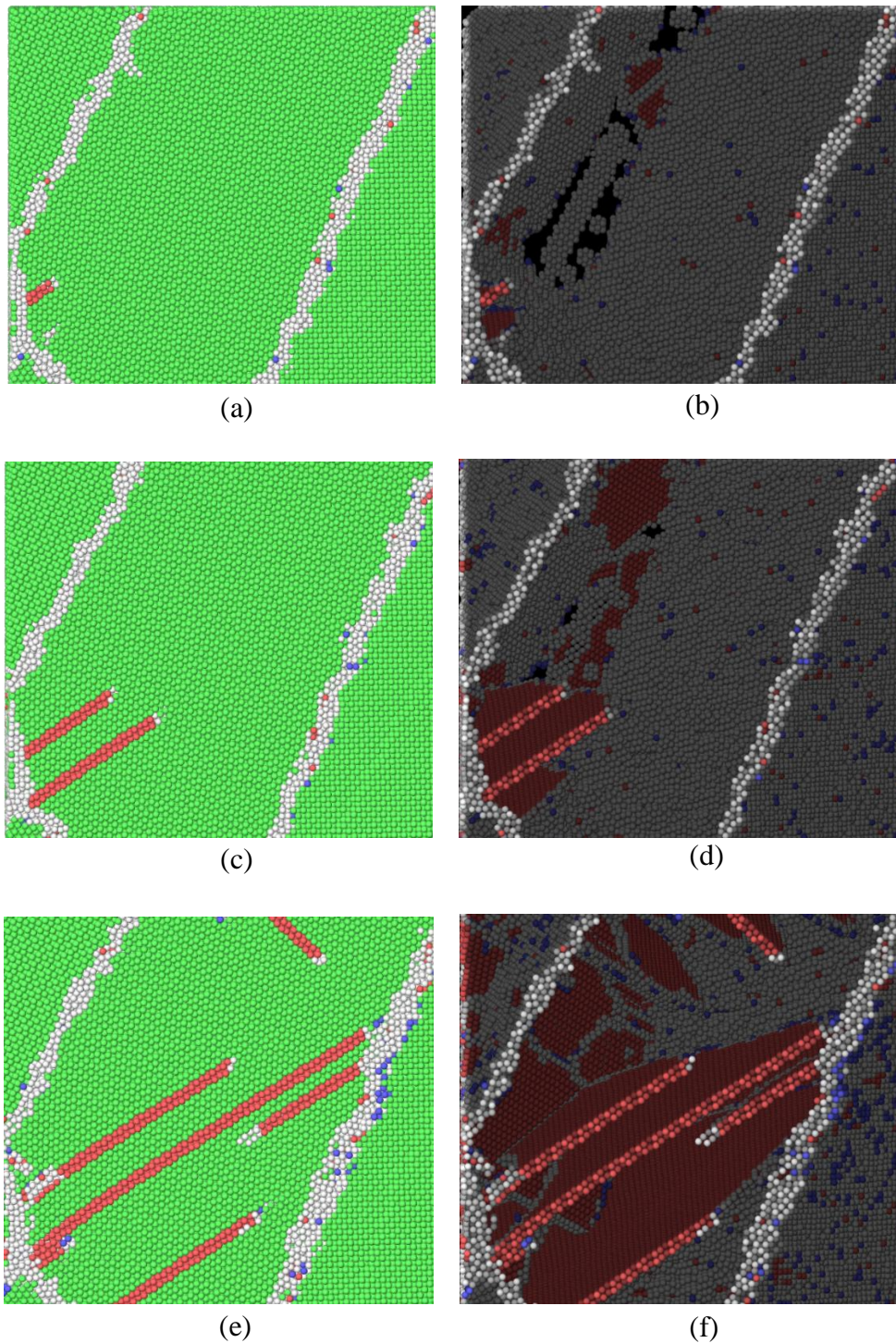
The observation of the 24.1 nm grain size samples during tensile testing showed that significant deformation occurs via the emission of leading partials from the grain boundaries. These partial dislocations are nucleated in the GB and glide through the lattice until being absorbed into the opposite GB, leaving behind stacking faults in the grain interior. This process is depicted in Figure 18.

Figure 17 – Resolved shear stress required to nucleate partial and perfect dislocations at GB with dependency on the critical radius.



Source: The author, 2021.

Figure 18 – Partial dislocation emitted from GB.



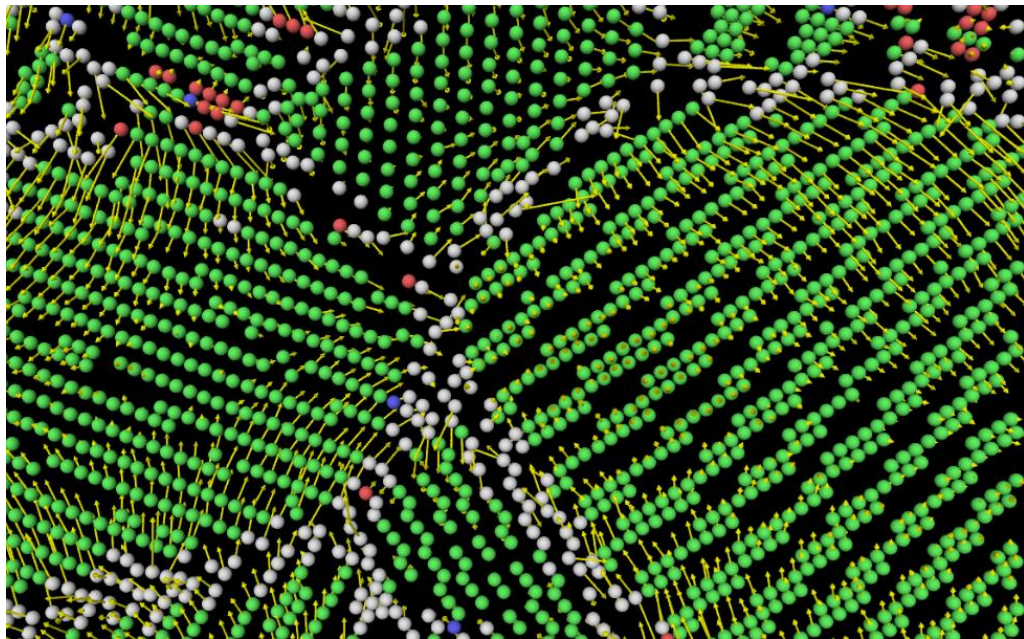
Legend: (a) Partial dislocation emitted from GB, (c) sliding inside the grain, (e) absorption in the opposite grain. Snapshots (b), (d), and (f) correspond to the same process, but the atoms of FCC structure were omitted to reveal the stacking fault planes created by the traveling of partial dislocations.

Source: The author, 2021.

4.2.3 Deformation behavior for sample with $d = 8.7$ nm

The 8.7 nm grain size sample also have no perfect dislocations inside grain interiors, only within GBs, and the motion of Shockley dislocations was observed in a similar way to the $d = 24.1$ nm sample. These results were expected, taking into account the previous analysis. Figure 19 shows a slab normal to the x-axis with 0.2 nm width, in which the yellow arrows represent the displacement vectors of atoms in the strain range from 0.030 to 0.085 with elimination of the affine deformation.

Figure 19 – Slab normal to the x-axis for the 8.7 nm sample with 0.2 nm width.



Legend: Yellow arrows represent the displacement vectors of atoms from 0.030 to 0.085 strain. Vectors were multiplied by 4 for the sake of visualization.

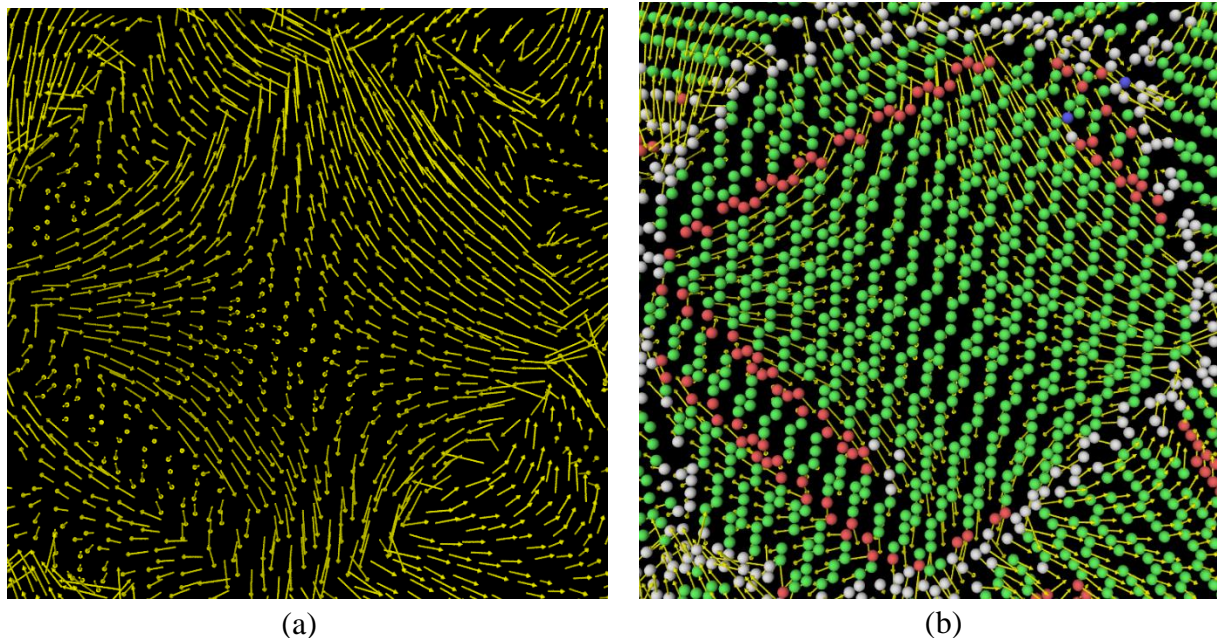
Source: The author, 2021.

Atoms inside or near to the GBs present higher displacements. Furthermore, triple points host a large concentration of atoms with high displacement modulus that cause a extensive impact on the lattice structure nearby. This fact can be indicative of GB-mediated deformation taking place. Indeed, the analysis indicates that a mechanism similar to Nabarro-Herring (NH) diffusional creep could be operative in the 8.7 nm grain size sample. Figure 20

shows a specific grain in which this phenomenon was observed. The GB atoms parallel to the tensile direction flow through the grain into GB lying perpendicularly to the tensile direction. Likely Coble creep is also active in the present nanocrystalline sample, but since this diffusion mechanism is restricted to GB, its contribution becomes complex to be identified. The high fraction of atoms in GBs and triple junctions associated with the high atomic displacement in the nearby lattice rotates some grains, as shown in Figure 21.

The nanocrystalline Ni deformation mechanisms, for sample with $d = 8.7$ nm, is a combination of dislocation motion, mostly Shockley partials, GR, GBS, and an NH-like creep. For the 24.1 nm grain size sample, the grain diameter precludes the NH-like creep and GR mechanisms, being the emission of partial dislocation from the GBs the primary plastic deformation mechanism. Therefore, it can be concluded that for grain sizes below approximately 20 nm, grain rotation and NH-like creep are enhanced due to the proximity of GBs, while emission of partial dislocations is still operational. Thus, the system, especially the GBs, possess more mechanisms to absorb and relaxing energy. This finding could explain the observed inverse HP relationship.

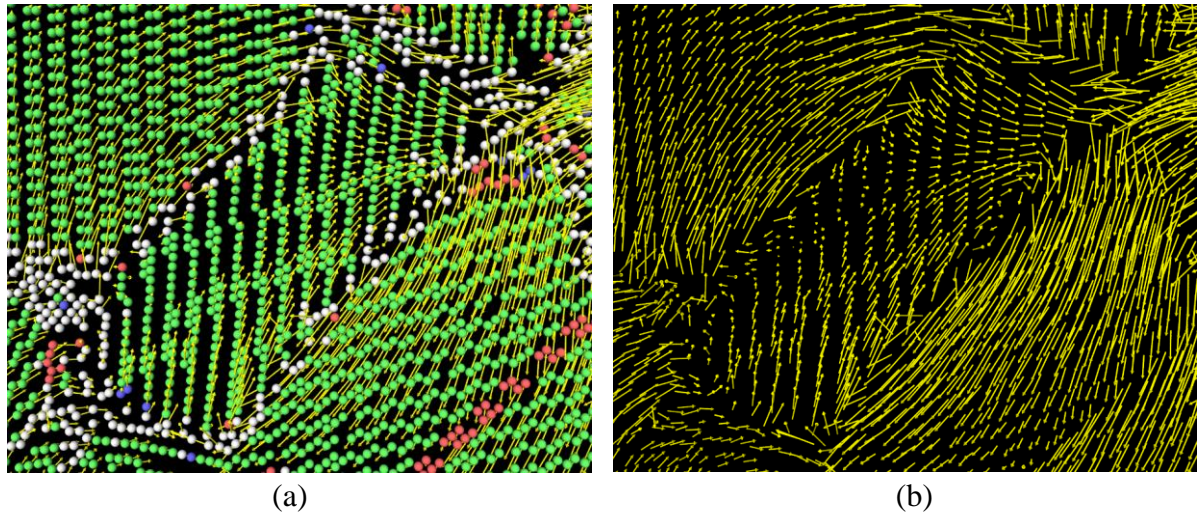
Figure 20 – NH-like mechanism taking place in a grain.



Legend: (a) Only displacement vectors and (b) atoms and vectors. Sample with 8.7 nm average grain size.

Source: The author, 2019.

Figure 21 - Grain undergoing rotation.



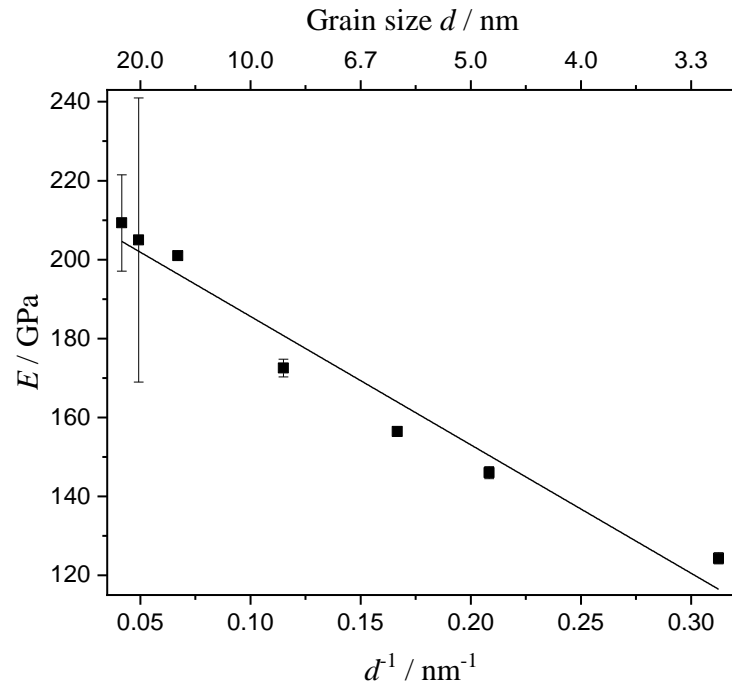
Legend: (a) Atoms with displacement vectors. (b) Only displacement vectors are shown.
Source: The author, 2021.

4.2.4 Young's modulus and composite models

As shown in Figure 22, the Young modulus approximately follows a linear relationship with the reciprocal grain size. A similar relation was also observed for platinum and copper using molecular dynamics simulations and experiments^{186,187}, respectively. Differently from what was observed for the ultimate stress, the sample with $d = 20.4$ nm presented the higher standard deviation, meaning that the texture influence seems not to be the only reason for this observation. For this specific grain size and the adopted conditions, the minimization algorithm could have been trapped in suboptimal solutions, instead of reaching the local optimal point, leading to some scattering in simulated mechanical properties.

Figure 23 shows the atomic fractions of both GB and grain interior as a function of the reciprocal grain size. As expected, the proportion of atoms in GBs increases as the grain size decreases, reaching approximately 50 % for the sample with $d = 3.2$ nm. Moreover, the atomic fraction shows a linear relationship with the reciprocal grain size.

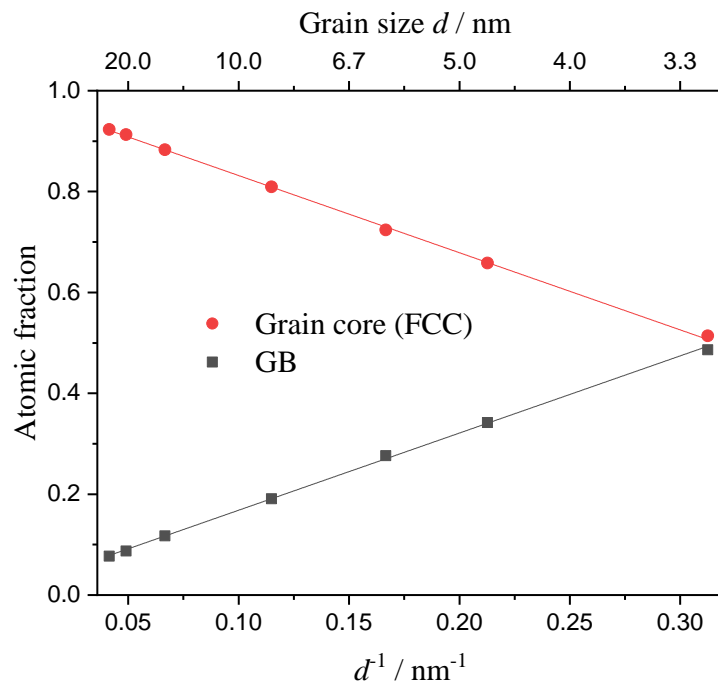
Figure 22 – Young’s modulus as a function of the reciprocal grain size.



Legend: The black line is the linear fit.

Source: The author, 2021.

Figure 23 – Fraction of atoms structured as FCC and GB as a function of reciprocal grain size.



Legend: The red and black lines are the linear fit of grain core and GB, respectively.

Source: The author, 2021.

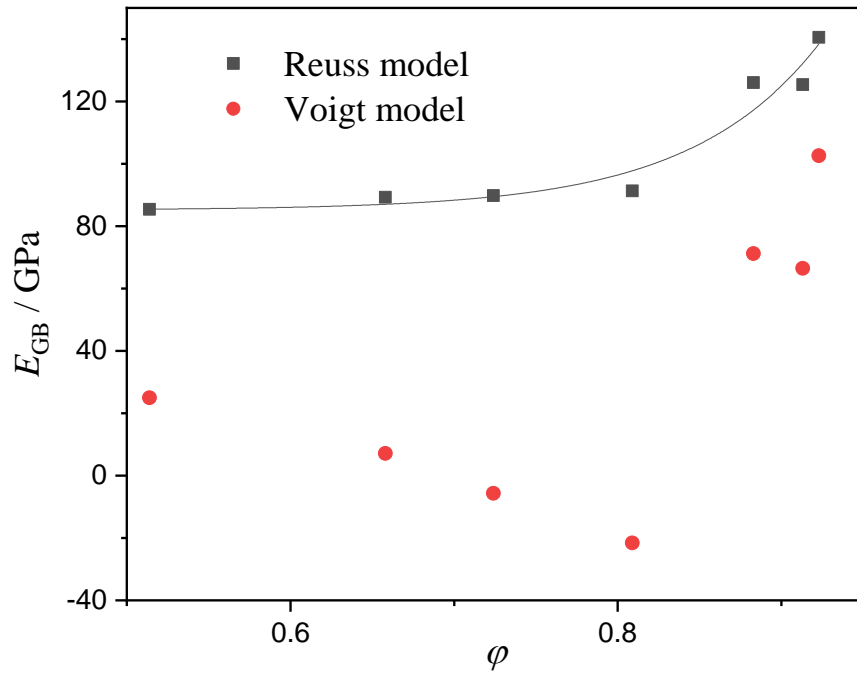
As previously mentioned, there is evidence that NC materials could be considered as a two-phase nanocomposite with the volumes of grains cores and GBs as component phases²². Additionally, studies on nanocrystalline platinum and copper revealed that GB's elastic modulus is considerably lower than the grain interior^{7,186}. To verify whether the present NC Ni samples can be considered nanocomposites, at least regarding the Young modulus, it was used the Voigt, Eq. (19), and the Reuss models, Eq. (20)¹⁸⁸⁻¹⁹⁰:

$$E = \varphi E_{core} + (1 - \varphi) E_{GB} \quad (19)$$

$$E = \frac{1}{\varphi/E_{core} + (1 - \varphi)/E_{GB}} \quad (20)$$

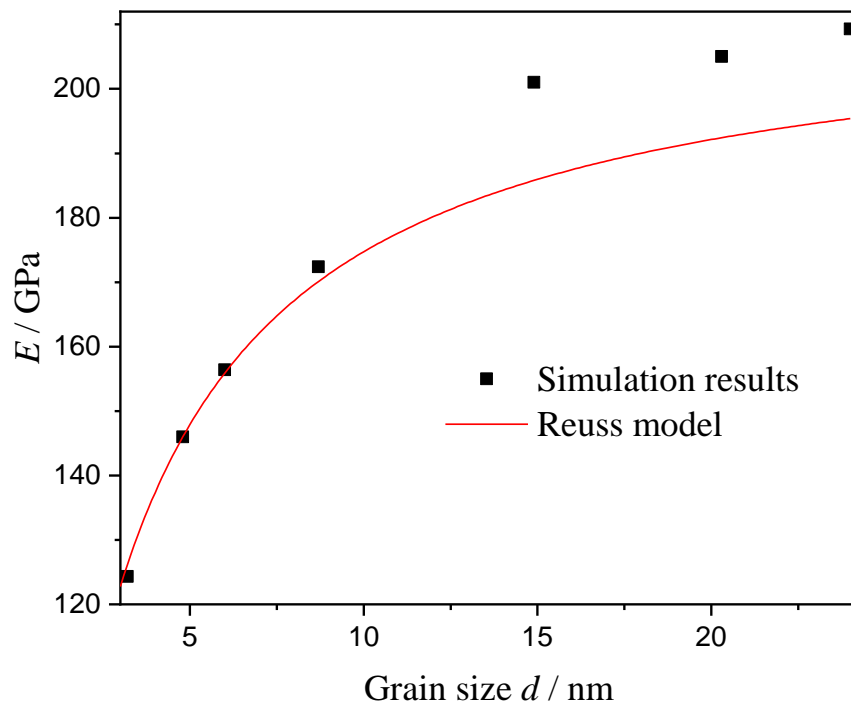
where φ , E_{core} and E_{GB} are the grain interior volume fraction, elasticity modulus of grain interior, and elasticity modulus of GB, respectively. In the absence of GB, $\varphi = 1$ and the Voigt and Reuss models lead to $E = E_{core}$. The value of E_{core} , extrapolated from Figure 10 for grain size tending to infinite, is 218.2 GPa. The elastic modulus of a completely amorphous Ni would yield E_{GB} . However, the simulation of an amorphous Ni structure is problematic, since during the energy minimization the system rapidly nucleates and grows crystallites. Therefore, to estimate E_{GB} , we fitted the relationship between Young's modulus and the fraction of atoms in grains with Voigt and Reuss models. Figure 24 shows the simulated results. Reuss model presents a constant relationship between E_{GB} and φ for $d \leq 8.7$ nm, intercepting the axis at $E_{GB} = 85.2$ GPa. The Voigt model does not present a pattern and also given unphysical negative values of E_{GB} . Therefore, only the Reuss model was considered. The ratio E_{GB}/E_{core} is 0.39, meaning that the GB elasticity modulus is 39 % of the grain interior component. For comparison purposes, the ratio E_{GB}/E_{core} for platinum and copper is 0.42 and 0.27^{7,186}, respectively. Evaluating E_{core} and E_{GB} in the Reuss model and plotting the data versus the grain size, Figure 25 shows that the Reuss model works quite well for $d \leq 8$ nm, whereas for larger grain sizes it deviates from the simulated results. The methodology used to find E_{GB} and E_{core} was a simple numerical approximation, with proper values, the Reuss model would probably produce more accurate results.

Figure 24 – Young's modulus of grain boundary E_{GB} using Voigt and Reuss model for composites materials.



Legend: The black line is the fitting of the Reuss model.
Source: The author, 2021.

Figure 25 – Dependency of Young's modulus with the grain size using the MD results and Reuss model for composites.

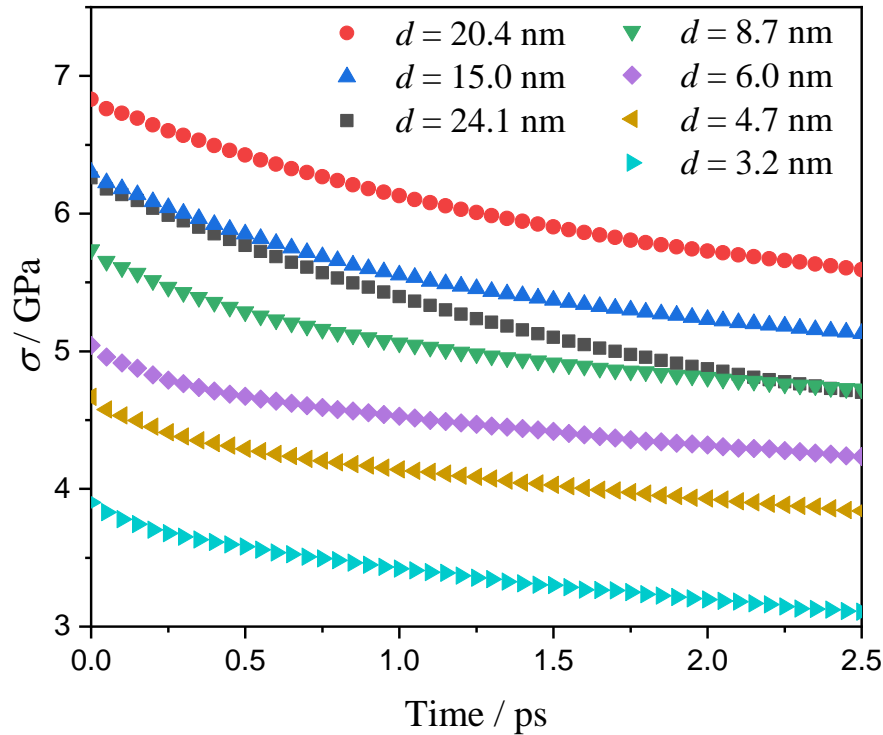


Source: The author, 2021.

4.2.5 Strain rate sensitivity

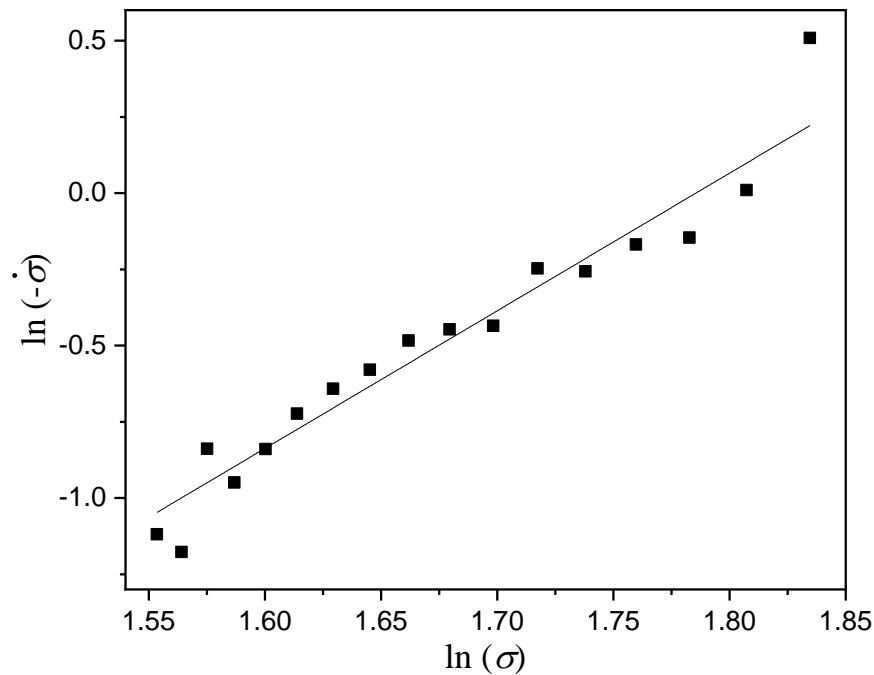
An important parameter to characterize metals and alloys' mechanical behavior is the strain rate sensitivity (SRS), m , usually defined as $m = \partial \ln \sigma / \partial \ln \dot{\epsilon}$, with σ as the stress and $\dot{\epsilon}$ as the strain rate^{191,192}. There are different methods to obtain the SRS, the main ones being the strain rate change and stress relaxation test^{193,194}. For the stress relaxation method, the SRS can be defined as $1/m = d(\ln -\dot{\sigma})/d(\ln \sigma)$ ^{193,195}, where $\dot{\sigma}$ is the time derivative of the stress. Very few attention, when it comes to MD, have been given to stress relaxation technique, and for this reason we decided to use it in this work. Since we are chiefly interested in the behavior near yielding, we decided to set the strain value in which the relaxation test would start at $\epsilon = 0.035$. The stress decay curves for all studied samples are shown in Figure 26. The plot in Figure 27, using $d = 24.1$ nm sample as an example, was used to obtain the strain rate sensitivity.

Figure 26 – Stress relaxation curves for NC samples starting at $\epsilon = 0.035$.



Source: The author, 2021.

Figure 27 – Plot for the sample with $d = 24.1$ nm grain size obtained from the stress relaxation curve.



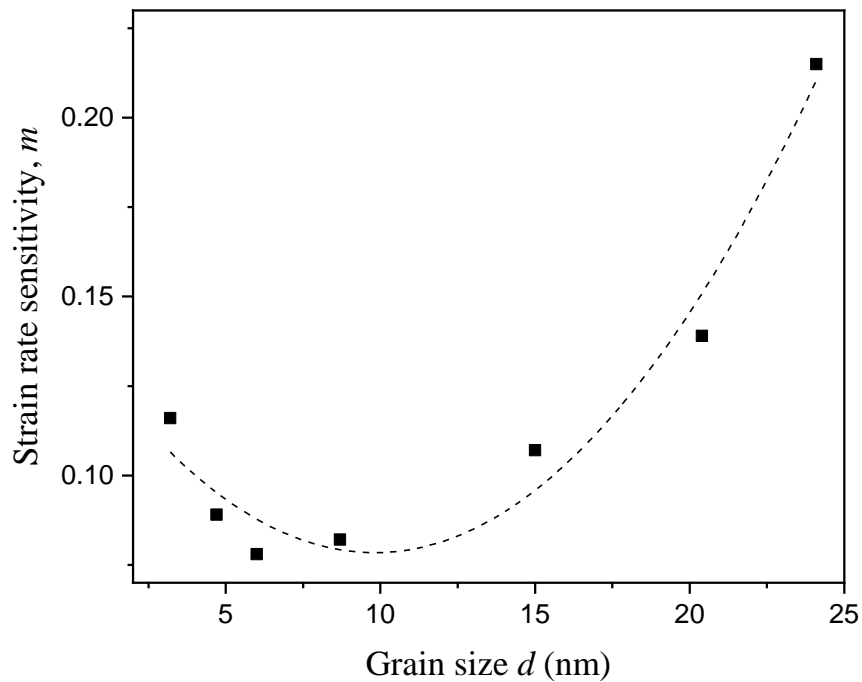
Legend: The linear fit was used to obtain the strain rate sensitivity, $1/m = d(\ln -\dot{\sigma})/d(\ln \sigma)$.

Source: The author, 2021.

The dependence of m with nanograin size is shown in Figure 28. The obtained m values represent a 20– to 50–fold increase when compared to that of coarse-grained Ni¹⁹⁶ ($m \leq 0.004$). A high m value was also reported for nanocrystalline copper¹⁹⁶⁻¹⁹⁸. For Ni, the experimental m value for an average grain size of 26 nm was reported to be approximately 0.1 (considering the upper limit)¹⁹⁹, which is nearly only half of the m value of the sample with $d = 24.1$ nm. However, it is important to notice that direct comparison between strain sensitivity values from different works must be taken carefully. There are several ways to obtain the m parameter, and they can yield markedly different results¹⁹³. In addition, experimental evaluation of m is obtained with a much lower strain rate ($\dot{\epsilon} < 10^3 \text{ s}^{-1}$) than MD typically uses ($\dot{\epsilon} > 10^8 \text{ s}^{-1}$). Furthermore, variables such as temperature, strain value at which the test was performed and deformation history can influence as well. Nevertheless, the values found for m are smaller than those expected for GBS or GBD. This behavior seems controversial since we have already demonstrated the occurrence of these mechanisms in our samples. However, the m values expected for GBS or GBD were also elaborated using different methods and, most importantly, under strain rates much lower than conventional MD simulations. At high strain rates used in

MD simulations, the thermally activated GBS and GBD might give place to a stress-driven process such as athermal grain-boundary sliding and migration²⁰⁰, thus affecting the m values.

Figure 28 – Strain rate sensitivity, m , versus grain size.



Legend: The dashed line is just a guide for the eyes.

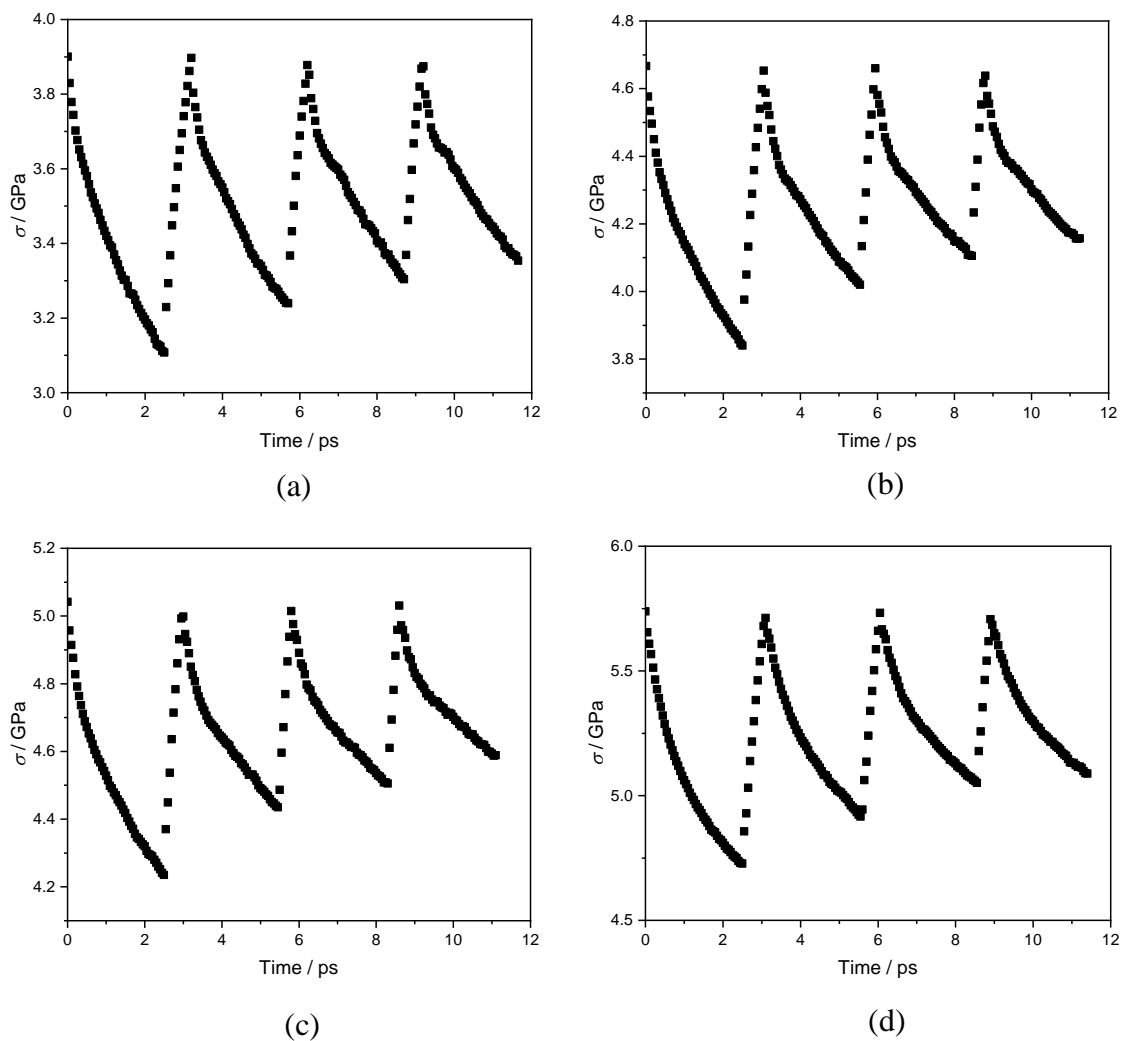
Source: The author, 2021.

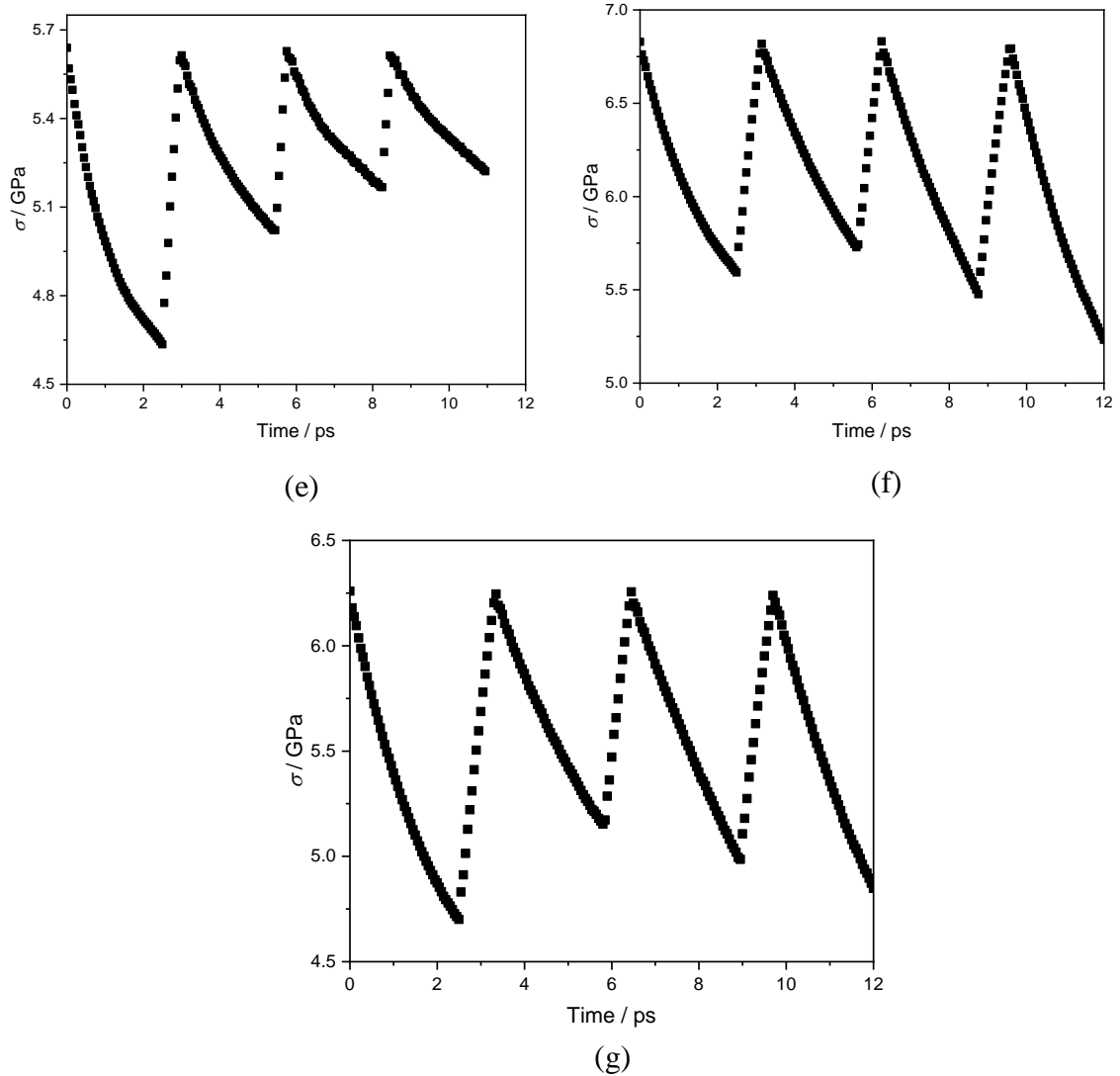
The new and exciting results are the decreasing m with grain size for $24.1 \leq d \leq 10$ nm and the opposite behavior below 10 nm. Several works revealed that the SRS is enhanced by reducing the grain size of FCC metallic materials²⁰¹⁻²⁰⁴. Thus, our results go against the expected behavior showing a regime with an opposite SRS grain size dependence. To the best of our knowledge, this is the first time that this behavior is reported using MD with relaxation test. Corroborating the findings, a relatively recent experimental work with copper using a high strain rate ($\sim 10^3 \text{ s}^{-1}$) showed this same trend²⁰⁵. Moreover, the shift from the SRS behavior at $d \approx 10$ nm is without a doubt an intriguing result since it is not related to the change in the HP relation. Perhaps this change in SRS behavior affects other mechanical responses, but out of this work scope, such as creep or fatigue.

To improve the understanding over SRS, repeated stress relaxation tests were performed, as shown in Figure 29. For samples with $d \leq 15.0$ nm, the relaxation curves demonstrate an increase in the stress levels at the end of each consecutive relaxation cycle

(hardening). The samples with $d > 15.0$ nm present hardening only in the second cycle, for the subsequent cycles, the stress level decreases at each cycle's end. Let us analyze first the samples with $d = 24.1$ nm and $d = 20.4$ nm. These samples are following the conventional HP relation. This means that hardening could occur due to the classical model of a decrease in mobile dislocation density. In this case, an increase in stress is expected at the end of each relaxation cycle²⁰⁶.

Figure 29 – Repeated stress relaxation tests.





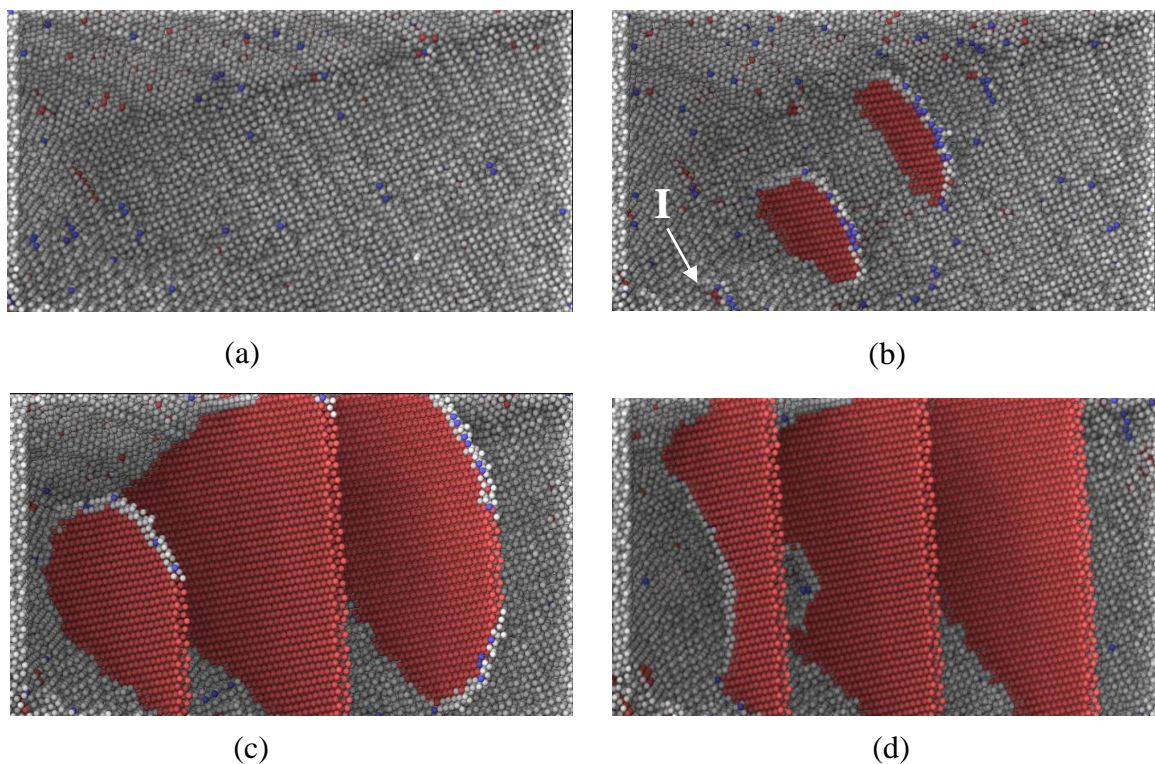
Legend: (a) $d = 3.2$ nm, (b) $d = 4.7$ nm, (c) $d = 6.0$ nm, (d) $d = 8.7$ nm, (e) $d = 15.0$ nm, (f) $d = 20.4$ nm, and (g) $d = 24.1$ nm.

Source: The author, 2021.

Experimental works have demonstrated that this trend is followed even for NC Ni with $d \approx 30$ nm^{195,207}. However, as already mentioned, there are neither perfect dislocation nor dislocation pile-up in our case; only partial dislocations are nucleated from GBs. At the end of the first relaxation cycle ($t \approx 2.5$ ps), for the $d = 24.1$ nm sample, no partial dislocation is observed (Figure 30(a)), although at the end of the second cycle ($t \approx 5.8$ ps) two dislocations have been nucleated while some others, as the one labeled as I in Figure 30(b), are still in the process of overcoming the critical radius to be emitted finally. This emission delay is likely affected by the strain rate applied. The release of dislocations from the GB is a relaxation mechanism. Since the dislocations are being nucleated, the system finds itself in an unrelaxed state, reflecting in

the second cycle's apparent hardening. In the third and fourth cycles, Figures 30(c) and 30(d), respectively, the release of dislocations has already been performed, and what is seen is only the dislocations glide, which requires lower stress than the nucleation. Nevertheless, a few dislocations continue to be nucleated after the second cycle until the last relaxation cycle, but it is not enough to cause hardening. The sample with $d = 20.4$ nm follows this same trend. For samples with $d \leq 15.0$ nm, the behavior is similar: at the end of the second cycle, the partial dislocations are still in the process of being emitted. However, as already demonstrated, other deformation mechanisms, such as GR and GBS, are operative in these samples, which could cause the apparent hardening in the relaxation cycles^{195,208}.

Figure 30 – Evolution of dislocations from GB for the sample with $d = 24.1$ nm.



Legend: At the end of: (a) first relaxation cycle ($t \approx 2.5$ ps), (b) second cycle ($t \approx 5.8$ ps), (c) third cycle ($t \approx 8.9$ ps), and (d) fourth cycle ($t \approx 12$ ps).

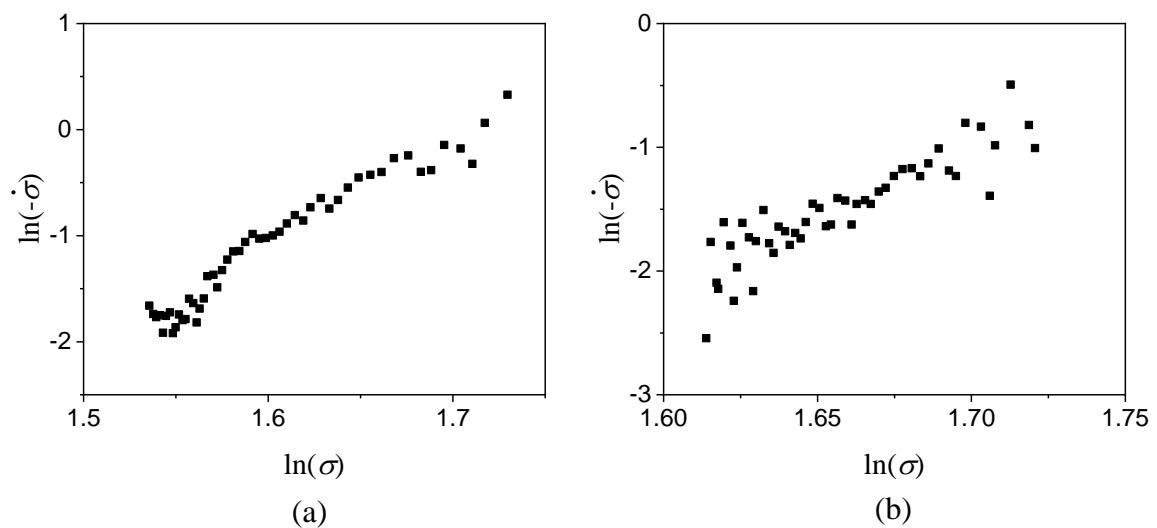
Source: The author, 2021.

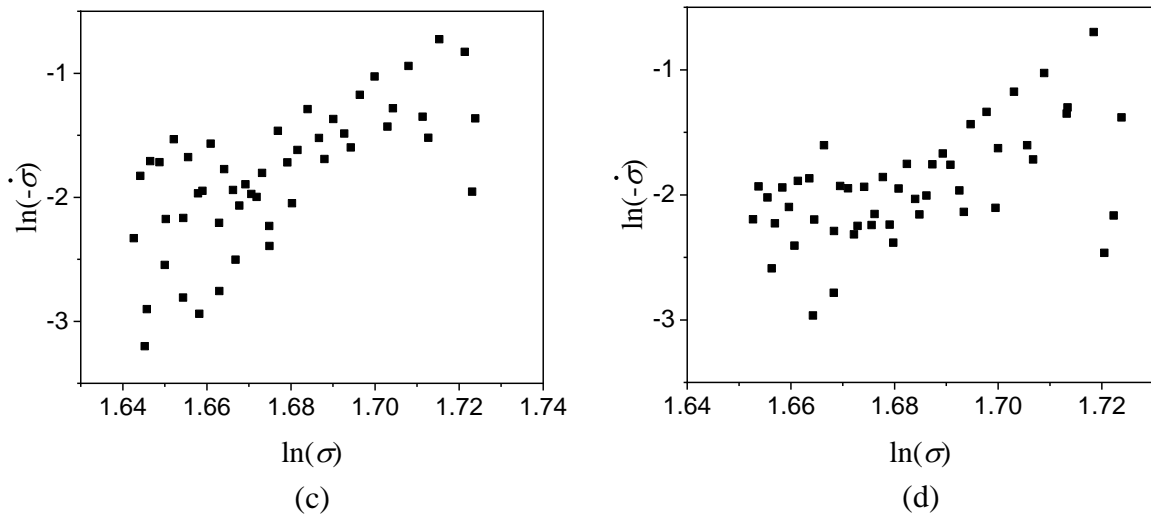
The SRS can be related to the apparent activation parameter (or apparent activation volume), V_a , using the equation¹⁹⁵:

$$V_a = \frac{\sqrt{3}kT}{m\sigma} \quad (21)$$

The V_a parameter is termed as “apparent” because the GB arrangements, microstructure, dislocation density etc., are not held constant during the stress relaxation test²⁰⁹. Hence, its value can, for the same material, vary according to the microstructural state of the specimen. Repeated stress relaxation tests are also useful to extract the effective activation parameter (or effective activation volume). The effective activation volume is considered to be more reliable and consistent than the apparent activation volume²⁰⁹. However, the central concept to obtain it is that the plot of $\ln(-\dot{\sigma})$ versus $\ln(\sigma)$ must produce a somewhat linear trend²⁰⁶, which is not the case with our samples. Figure 31 shows the non-linear trend for all relaxation curves except the first for the sample with $d = 15.0$ nm as an example. For this reason, it is not possible to extract the effective activation volume for these samples. It is unclear the reason for the non-observance of straight line in these plots, since for single element FCC materials or superplastic alloys this behavior is expected¹⁹⁵. Perhaps if the relaxation time were longer, the system would have enough time to accommodate the atoms better, minimizing the energy and allowing the curve to stabilize, or the load between each cycle should have been performed at a slower pace, or it might be an intrinsic limitation of the MD approach.

Figure 31 – Plot of $\ln(-\dot{\sigma})$ versus $\ln(\sigma)$ for the sample with $d = 15.0$ nm.





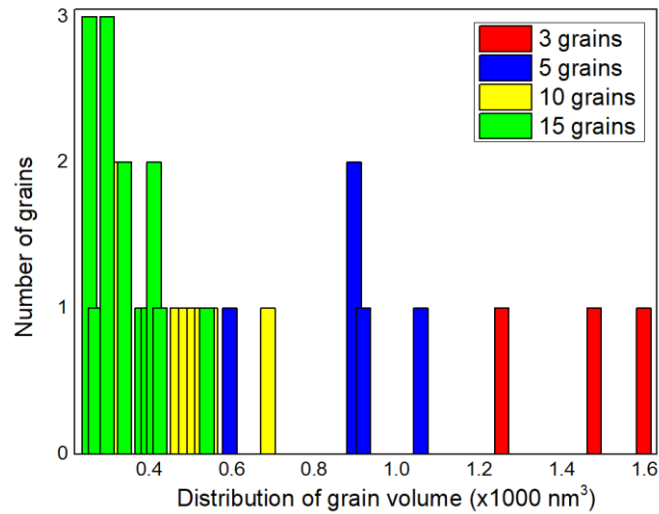
Legend: (a) First, (b) second, (c) third, and (d) fourth relaxation cycle.
Source: The author, 2021.

In any case, the dislocation glide speed was calculated by using two atomic snapshots at different timesteps. The dislocation traveled distance and the time between the snapshots was measured using OVITO code. Thus, the dislocation glide speed was readily calculated, yielding values from 0.5 to 2.0 nm.ps⁻¹. Considering the maximum glide speed, a dislocation would take approximately 12 ps and 10 ps to cross the entire grain for the samples with $d = 24.1$ nm and $d = 20.4$ nm, respectively. The total relaxation time in this work was approximately 12 ps. The study of strain rate sensitivity of nanocrystalline metals is rare and complex; hence it deserves further investigation.

4.3 Aluminum

The distribution of grain volumes for each sample is shown in Figure 32. Since the total volume of the samples is constant (4500 nm³), the histogram shows the sample with fewer grains having a higher individual grain volume.

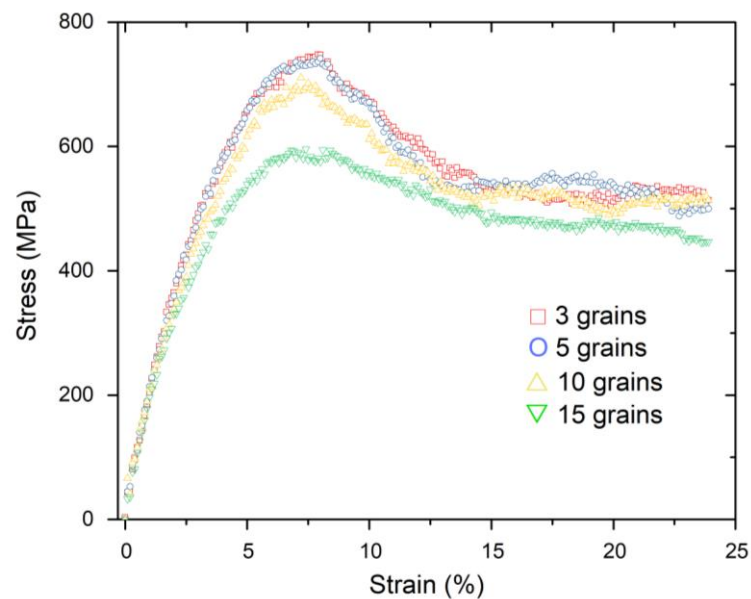
Figure 32 – Grain volume distribution for the four Al nanocrystalline samples.



Source: The author, 2021.

The simulated stress-strain curves are shown in Figure 33. The sample with 15 grains (smallest grain size) shows the lowest mechanical resistance. In comparison, the sample with three grains (largest grain size) presents the highest strength, with the 5 and 10 grains nanocrystals presenting intermediate stress values and obeying the inverse relationship.

Figure 33 – Stress-strain curves of Al nanocrystalline samples.

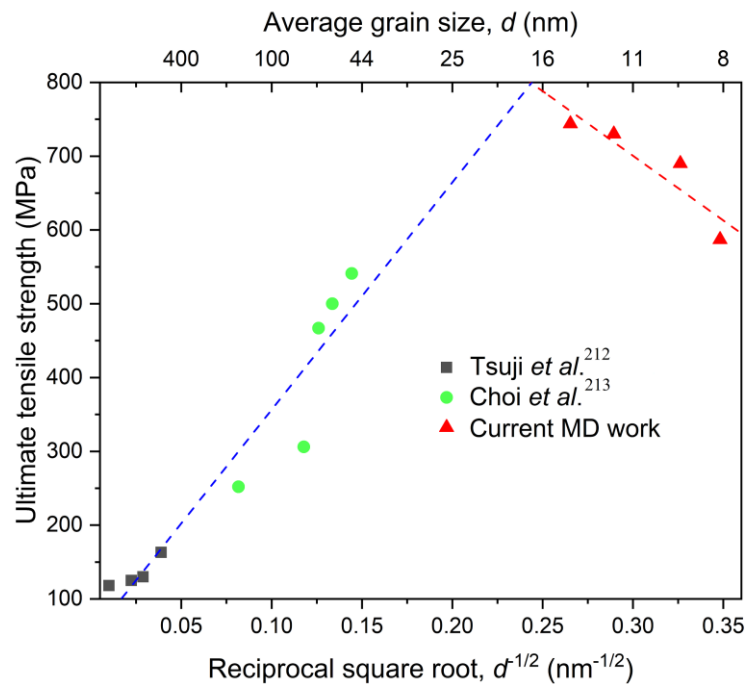


Source: The author, 2021.

The similar mechanical behavior between the three and five nanocrystalline grain samples is related because they are close to the point where the transition from the conventional to the inverse Hall-Petch relationship occurs. This transition does not occur abruptly. It is expected, for grain sizes close to the transition, a parabolic behavior. This behavior was reported in the literature using MD for copper²¹⁰, and experimentally for 0.6%C steel²¹¹. Thus, for materials with grain sizes close to the parabola vertex, the difference between their stress values is small compared to materials with grain sizes far from the vertex. For this reason, the difference between the stress values for the 5 and 10 grains samples was not pronounced.

Experimental tensile testing of samples with grain sizes ranging from micrometer to nanometer for aluminum with at least 99% purity can be found elsewhere^{212,213}. Figure 34 presents the combination of these data with the results of the present MD work. The blue and red dashed lines are the linear fit for the ultimate stress of individual behaviors. The ultimate tensile strength was used in Figure 34 instead of yield stress to ease both HP regimes' visualization.

Figure 34 – Conventional (dashed blue line) and inverse (dashed red line) Hall-Petch relationship.

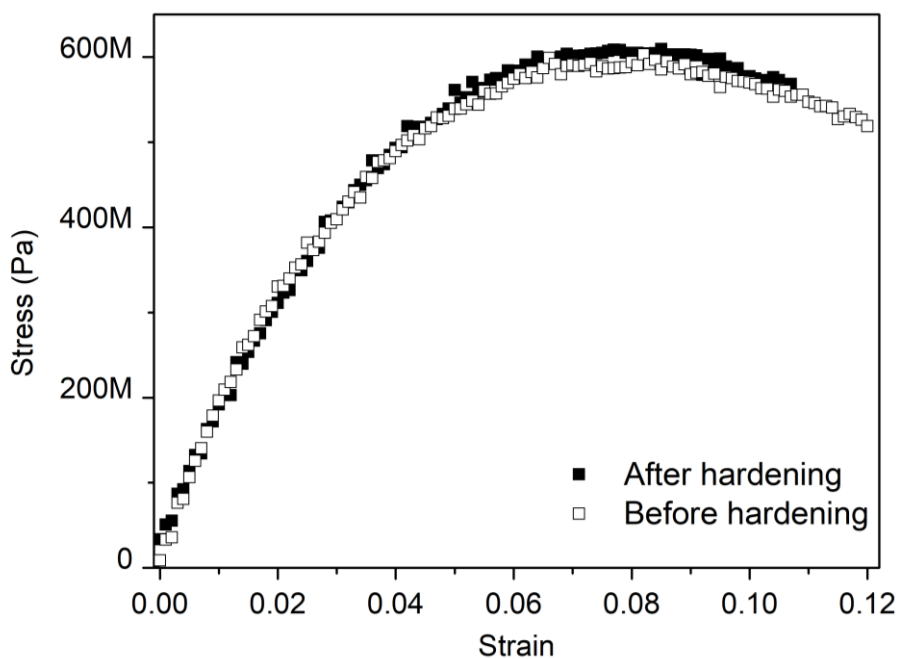


Source: The author, 2021.

The fitted intersection corresponds to the grain size of approximately 17 nm. Although close to the expected grain size transition value from conventional to inverse HP relationship for metals, the 17 nm value might be in practice even small. This assumption is based on two reasons: (1) the fitting curves of Figure 36 were extrapolated to cover the full axis range jeopardizing the results, especially for grain sizes below 50 nm due to a lack of reliable experimental data and; (2) a reduction in the slope of the conventional Hall-Petch relationship is expected at grain size below 100 nm, thus changing its direction.

To assess whether the dislocation mechanism persists for the Al NC samples, the 15 and 10 grain systems' strain hardening behavior was analyzed. It is well known that the strain hardening phenomenon occurs basically by the generation and interaction of the dislocation stress fields¹⁷. Thus, it is expected that the nanocrystalline samples do not present strain hardening since the reduced grain sizes would difficult or even inhibit the generation of dislocations. Figure 35 shows the tensile test curve before and after the strain hardening of the 15-grain system. The 10-grain system has similar behavior and was not exhibited.

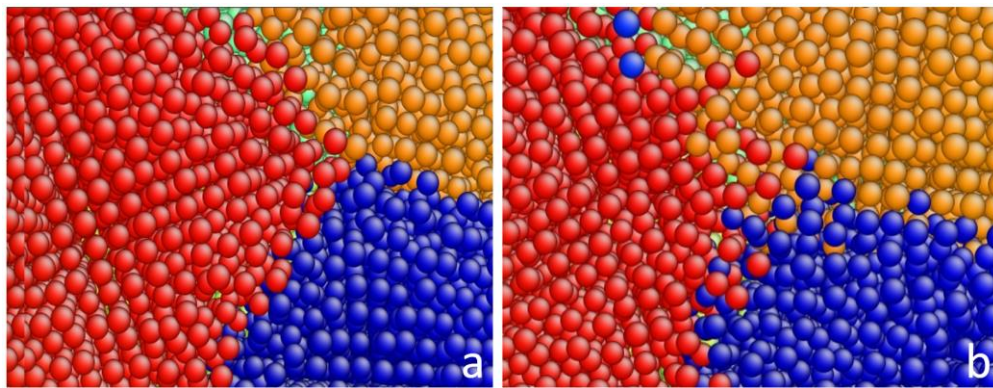
Figure 35 – Tensile test result after strain hardening of the 15-grain nanocrystalline sample.



Source: The author, 2021.

The stress-strain curves showed in Figure 35 confirms the expectation that no significant increase in strength should be observed after strain hardening for nanocrystalline systems. Therefore, for the conditions applied in this work, dislocations are not responsible for the plastic deformation. Coble creep was also evidenced, as shown in Figure 36 for the 15-grain sample. Grain boundaries are well defined before loading. However, after 6% of strain, it is possible to observe some atoms migrating along the neighboring grains due to diffusion. Furthermore, the grains are rotated relatively from their original position.

Figure 36 – A triple junction of the 15-grain sample.



Legend: (a) Grain boundaries before the tensile test, (b) Grain boundaries after a strain of 6%. Note the small displacement of atoms in grain boundaries. Colors are used to reveal the grains and are not related with the atomic arrangement.

Source: The author, 2021.

CONCLUSIONS

Concerning the $\text{Al}_{80}\text{Ti}_{15}\text{Ni}_5$ alloy, the decreasing of Young modulus and ultimate tensile strength with grain size suggests that grain boundaries are elastically softer than grain cores. Furthermore, this behavior indicates that the amorphous structure represents a lower limit-case of the nanocrystalline structure. In the amorphous sample, shear transformation zones were still formed in the elastic regime, and its coalescence becomes shear bands with increasing strain. The results indicate that the plastic deformation is governed by the interplay of grain boundary sliding and grain boundary diffusion for the nanocrystalline samples. The reduced grain rotation of less than 0.34° is probably caused by solute atoms acting as pinning points. An increase of partial dislocation was observed, but its contribution to the total deformation was limited. For instance, 0.07 strain causes a relatively small increase in dislocation density of just one order of magnitude. Although the ternary interatomic potential used for the AlNiTi alloy has not shown great accuracy, at least for the elastic moduli, the results can still be useful in a qualitative approach to describe the structural evolution under strain.

Regarding the nanocrystalline nickel, the yield and ultimate tensile stresses obeyed the inverse Hall-Petch relationship for grains smaller than *circa* 20 nm. The sample with $d = 24.1$ nm did not show perfect dislocations despite being inside the conventional HP domain and possessing high stacking fault energy, indicating that the inhibition of perfect dislocations does not cause the transition from conventional to inverse HP. The suppression of conventional slip mechanism likely only causes a deviation from the HP relationship. The grain size that provokes a transition from perfect dislocations to Shockley partial emission at grain boundaries was calculated to be around 37.7 nm. However, this finding was considered valid for samples built with Voronoi tessellation with random crystallographic directions and no insertion of defects inside the grain interior. For pure Ni materials, it can be postulated the existence of three deformation regimes concerning grain size:

1. A regime that follows the conventional HP relationship ($d \geq 37.7$ nm);
2. A regime that occurs due to the incapacity of perfect dislocations to be nucleated from grain boundaries resulting in an HP deviation, this regime is characterized by the emission of Shockley partials from the grain boundaries that leave stacking faults along the path ($20 \leq d \leq 37.7$ nm);

3. A regime that occurs below 20 nm and corresponds to the beginning of the inverse HP relationship. In this regime, the average distance of GBs and triple junctions is such that the displacement of atoms during strain causes grain rotation and grain boundary sliding, along with Coble/Nabarro-Herring creep. Thus, the inverse HP relation is most likely caused by the onset of these mechanisms.

The Young modulus showed a linear relationship with the reciprocal grain size, denoting a direct dependency on the grain boundary atomic fraction. By fitting the relevant results, Young's modulus of grain boundary was equal to 39 % of the grain interior. Although using a simple concept, the Reuss model for composites has demonstrated predictive results for smaller grains. The Reuss model would probably present better results if the parameters were more adequate. However, the complexity in simulating a completely amorphous nickel material is prohibited. A new finding corresponding to the strain rate sensitivity parameter showed an unusual behavior, with a regime in which it decreases with the grain size. At first, this fact was associated to the high strain rate used. However, at $d \approx 10$ nm, a change in this pattern occurs; the strain rate sensitivity begins to increase with decreasing grain size. This fact indicates that an essential change in some mechanical response and atomic rearrangement might occur at this grain size. Nevertheless, due to the incapability of extracting the effective activation volume using stress relaxation tests, further strain sensitive analysis is necessary.

Lastly, the nanocrystalline aluminum has also followed an inverse Hall-Petch relationship. The grain size transition from conventional to inverse Hall-Petch relationship was calculated to be around 17 nm. No strain hardening was observed for the 10 and 15-grain samples. Thus, the conventional plastic deformation mechanism of dislocation glide was not considered necessary in this study. The atomic diffusion along the grain boundaries, Coble creep, and grain rotation were observed.

REFERENCES

- 1 DOBRZAŃSKI, L. A. Significance of materials science for the future development of societies. *J. Mater. Process. Technol.*, v. 175, p. 133-148, 2006.
- 2 XU, Q. Thoughts on the development of new material technology. *IOP Conference Series: Materials Science and Engineering*, v. 493, p. 012122, 2019.
- 3 TIMOSHENKO, S. P. *History of strength of materials*. USA: McGraw-Hill, 1953.
- 4 DIETER G.E. *Mechanical Metallurgy*. Singapore: McGraw-Hill, 1988.
- 5 MOURITZ, A. Strengthening of metal alloys, in MOURITZ, A (ed), *Introduction to Aerospace Materials*. Cambridge: Woodhead Publishing, 2012. p. 57-90.
- 6 CHERKAOUI, M.; CAPOLUNGO, L. *Atomistic and continuum modeling of nanocrystalline materials: deformation mechanisms and scale transition*. New York: Springer, 2009.
- 7 GAO, G.-J. J.; WANG, Y.-J.; OGATA, S. Studying the elastic properties of nanocrystalline copper using a model of randomly packed uniform grains. *Comput. Mater. Sci.*, v. 79, p. 56-62, 2013.
- 8 GLEITER, H. Nanocrystalline materials. *Prog. Mater. Sci.*, v. 33, p. 223-315, 1989.
- 9 MEYERS, M. A.; MISHRA, A.; BENSON, D. J. Mechanical properties of nanocrystalline materials. *Prog. Mater. Sci.*, v. 51, pp. 427-556, 2006.
- 10 BIRRINGER, R. et al. Nanocrystalline materials an approach to a novel solid structure with gas-like disorder? *Phys. Lett A*, v. 102, p. 365-369, 1984.
- 11 CHEN, M. et al. Deformation twinning in nanocrystalline aluminum. *Science*, v. 23, p. 1275-1277, 2003.
- 12 BONETTI, E. et al. Anelasticity and structural stability of nanostructured metals and compounds. *Nanostruct. Mater.*, v. 6, p. 639-642, 1995.
- 13 WÜRSCHUM, R.; HERTH, S.; BROSSMANN, U. Diffusion in nanocrystalline metals and alloys - A Status Report. *Adv. Eng. Mater.*, v. 5, p. 365-372, 2003.
- 14 SINGH, M.; LARA, S.; TLALI, S. Effects of size and shape on the specific heat, melting entropy and enthalpy of nanomaterials. *J. Taibah Univ. Sci.*, v. 11, p. 922-929, 2017.
- 15 AVRAMOV, I.; MICHAILOV, M. Specific heat of nanocrystals. *J. Phys. Condens. Matter*, v. 20, p. 295224, 2008.
- 16 HERZER, G. Nanocrystalline soft magnetic materials. *J. Magn. Magn. Mater.*, v.112, p.258-262, 1992.
- 17 HULL, D.; BACON, D. J. *Introduction to dislocations*. 5 ed. Oxford: Elsevier, 2011.

- 18 REED-HILL, R.E. *Physical metallurgy principles*. Canada: D. Van Nostrand, 1968.
- 19 HALL, E. O. The deformation and ageing of mild steel: III Discussion of Results. *Proc. Phys. Soc. B*, v. 64, p. 747, 1951.
- 20 PETCH, N. J. The cleavage strength of polycrystal. *J. Iron Steel Inst.*, v. 174, p. 25-28, 1953.
- 21 HANSEN, N. Hall-Petch relation and boundary strengthening. *Scr. Mater.*, v. 51, p.801-806, 2004.
- 22 TIAN, L.; LI, L. A review on strengthening of nanostructured materials. *Int. J. Eng. Technol.*, v. 8, p. 236-249, 2018.
- 23 CHOKSHI, A. H. et al. On the validity of the Hall-Petch relationship in nanocrystalline materials. *Scr. Metall.*, v. 23, p. 1679-1684, 1989.
- 24 FOUGERE, G. E. et al. Grain-size dependent hardening and softening of nanocrystalline Cu and Pd. *Scr. Metall. Mater*, v. 26, p. 1879-1883, 1992.
- 25 YANG, M.C. et al. Study on microhardness of bulk nanocrystalline copper. *Nanostruct. Mater.*, v. 9, p. 481-484, 1997.
- 26 CHANG, H. et al. Synthesis, processing and properties of nanophase TiAl. *Scr. Metall. Mater.*, v. 25, p. 1161-1166, 1991.
- 27 CHANG, H.; ALTSTETTER, C. J.; AVERBACK, R. S. Characteristics of nanophase TiAl produced by inert gas condensation. *J. Mater. Res.*, v. 7, p. 2962-2970, 1992.
- 28 SONG, H. W.; GUO, S.R.; HU, Z. Q. A coherent polycrystal model for the inverse Hall-Petch relation in nanocrystalline materials. *Nanostruct. Mater.*, v. 11, p. 203-210, 1999.
- 29 NOSKOVA, N. I. The structure and properties of nanocrystalline polyphase alloys. *Nanostruct. Mater.*, v. 9, p. 505-508, 1997.
- 30 HU, J. et al. Grain boundary stability governs hardening and softening in extremely fine nanograined metals. *Science*, v. 355, p. 1292-1296, 2017.
- 31 NIEMAN, G.W.; WEERTEMAN, J. R.; SIEGEL, R.W. Microhardness of nanocrystalline palladium and copper produced by inert-gas condensation. *Scr. Metall.*, v. 23, p. 2013-2018, 1989.
- 32 SURYANARAYANA, C.; KOCH, C. C. Nanocrystalline materials – Current research and future directions. *Hyperfine Interact.*, v. 130, p. 5-44, 2000.
- 33 PADILLA, H. A.; BOYCE, B. L. A review of fatigue in nanocrystalline materials. *Exp. Mech.*, v. 50, p. 5-23, 2010.

- 34 KOCH, C. C; NARAYAN, J. The inverse Hall-Petch effect – Fact or Artifact? *Mat. Res. Soc. Symp.*, v. 634, 2001.
- 35 NAIK, S. N.; WALLEY, S. M. The Hall-Petch and inverse Hall-Petch relations and the hardness of nanocrystalline metals. *J. Mater. Sci.*, v. 55, p. 2661-2681, 2020.
- 36 GERTSMAN, V. Y. et al. The study of grain size dependence of yield stress of copper for a wide grain size range. *Acta Metall. Mater.*, v. 42, p. 3539-3544, 1944.
- 37 AGNEW, S.R. et al. Microstructure and mechanical behavior of nanocrystalline metals. *Mater. Sci. Eng. A*, v. 285, p. 391-396, 2000.
- 38 PANDE, C. S.; COOPER, K.P. Nanomechanics of Hall-Petch relationship in nanocrystalline materials. *Prog. Mater. Sci.*, v.54, p. 689-706, 2009.
- 39 EL-SHERIK, A. M. et al. Deviations from hall-etch behavior in as-prepared nanocrystalline nickel. *Scripta Metall. et Mater.*, v. 27, p. 1185-1188, 1992.
- 40 CHEUNG, C.; PALUMBO, G.; ERB, U. Synthesis of nanocrystalline permalloy by electrodeposition. *Scr. Metall. et Mater.*, v. 31, p. 735-740, 1994.
- 41 MATSUI, I. et al. Mechanical behavior of electrodeposited bulk nanocrystalline Fe-Ni alloys. *Mater. Res.*, v. 18, p. 95-100, 2015.
- 42 ERB, U. et al. In: SURYANARAYANA, C.; SING, J.; FROES, FH. *Processing and properties of nanocrystalline materials*. Warrendale: The Minerals, Metals & Materials Society, 1996.
- 43 MORRIS, D. G. The origins of strengthening in nanostructured metals and alloys. *Rev. de Metal.*, v. 46, p. 173-186, 2010.
- 44 TRELEWICZ, J. R.; SCHUH, C.A. The Hall–Petch breakdown in nanocrystalline metals: A crossover to glass-like deformation. *Acta Mater.*, v. 55, p. 5948-5958, 2007.
- 45 LU, K.; WEI, W.D.; WANG, J.T. Microhardness and fracture properties of nanocrystalline Ni-P alloy. *Scr. Metall. et Mater.*, v. 24, p. 2319-2323, 1990.
- 46 CORDERO, Z. C.; KNIGHT, B. E.; SCHUH, C. A. Six decades of the Hall–Petch effect – a survey of grain-size strengthening studies on pure metals. *Int. Mater. Rev.*, v. 61, p. 495-512, 2016.
- 47 LUO, J.; WANG, Z. On the Physical Meaning of the Hall-Petch Constant. *Adv. Mat. Res.*, v. 15-17, p. 643-648, 2007.
- 48 NIEH, T. G.; WADSWORTH, J. Hall-Petch relation in nanocrystalline solids. *Scr. Metall. Mater.*, v. 25, p. 955-658, 1991.
- 49 UNGÁR, T. et al. Dislocations, grain size and planar faults in nanostructured copper determined by high resolution X-ray diffraction and a new procedure of peak profile analysis. *Acta Mater.*, v. 46, p. 3693-3699, 1998.

- 50 SCATTERGOOD, R. O.; KOCH, C. C. A modified-model for Hall–Petch behavior in nanocrystalline materials. *Scr. Metall. Mater.*, v. 27, p. 1195-1200, 1992.
- 51 LIAN, J. B.; BUADELET, B.; NAZAROV, A. Model for the prediction of the mechanical behavior of nanocrystalline materials. *Mater Sci Eng A*, v.172, p. 23-29, 1993.
- 52 MASAMURA, R. A. et al. Yield stress of fine grained materials. *Acta Metall.*, v. 13, p. 4527-4534, 1998.
- 53 CONHAD, H.; NARAYAN, J. On the grain size softening in nanocrystalline materials. *Scr. Mater.*, v. 42, p. 1025-1030, 2000.
- 54 TAKEUCHI, S. The mechanism of the inverse Hall–Petch relation in nanocrystals. *Scr. Mater.*, v. 44, p. 1483, 2001.
- 55 LU, K.; SUI, M. L. An explanation of the Hall–Petch law in micro and nanocrystalline materials. *Scr. Mater.*, v. 28, p. 1465-1470, 1993.
- 56 KONSTANTINIDIS, D. A.; AIFANTIS, E. C. On the “anomalous” hardness of nanocrystalline materials. *Nanostruct. Mater.*, v.10, p. 1111-1118, 1998.
- 57 CARLTON, C. E.; FERREIRA, P. J. What is behind the inverse Hall–Petch effect in nanocrystalline materials? *Acta Mater.*, v. 55, p. 3749-3756, 2007.
- 58 ROMANOV, A. E. Continuum theory of defects in nanoscaled materials. *Nanostruct. Mater.*, v.6, p. 125-134, 1995.
- 59 GRYAZNOV, V. G.; KAPRELOV, A. M.; ROMANOV, A. E. Size effect of dislocation stability in small particles and microcrystallites. *Scr. Metall.*, v. 23, p. 1443-1448, 1989.
- 60 SIEGEL, R. W.; FOUGERE, G. E. Mechanical properties of nanophase metals. *Nanostruct. Mater.*, v. 6, p. 205-216, 1995.
- 61 GOGOTSI, Y. *Nanomaterials handbook*. First ed. Florida: Taylor & Francis Group, 2006.
- 62 BUDROVIC, Z.; SWYGENHOVEN, H. V.; DERLET, P. M.; PETEGEM, S. V.; SCHMITT, B. Plastic Deformation with Reversible Peak Broadening in Nanocrystalline Nickel. *Science*, v. 304, p. 273-276, 2004.
- 63 NABARRO, F. R. N. Deformation of crystals by the motion of single ions. *Report of a Conference on the Strength of Solids*, Physical Society, London, p. 75-90, 1948.
- 64 HERRING, C. Diffusional Viscosity of a Polycrystalline Solid. *J. Appl. Phys*, v. 21, p. 437-445, 1950.
- 65 COBLE, R. L. A Model for boundary diffusion controlled creep in polycrystalline materials. *J. Appl. Phys.*, v. 34, p. 1679, 1963.

- 66 MASUMURA, R. A.; HAZZLEDINE, P. M.; PANDE, C. S. *Acta Mater.*, v. 46, p. 4527, 1998.
- 67 QUEK, S. S.; CHOOI, Z. H.; WU, Z.; ZHANG, Y. W. The inverse hall–petch relation in nanocrystalline metals: A discrete dislocation dynamics analysis. *J. Mech. Phys. Solids.*, v. 88, p. 252-266, 2016.
- 68 LU, L.; SUI, L.; LU, K. Superplastic extensibility of nanocrystalline copper at room temperature. *Science*, v. 287, p. 1463-1466, 2000.
- 69 VALIEV, R. Z. et al. Deformation behaviour of ultra-fine-grained copper. *Acta Metall. Mater.*, v. 42, p. 2467-2475, 1994.
- 70 SWYGENHOVEN, H.; CARO, A.; FARKAS, D. Grain boundary structure and its influence on plastic deformation of polycrystalline FCC metals at the nanoscale: A Molecular Dynamics study. *Scripta Mater.*, v. 44, p. 1513-1516, 2001.
- 71 LIFSHITZ, M. On the theory of diffusion-viscous flow of polycrystalline bodies. *J. Exp. Theor. Phys.*, v. 17, p. 909, 1963.
- 72 RACHINGER, W. A. Relative grain translations in the plastic flow of aluminum. *J. Inst. Met.*, v. 81, p. 33, 1952.
- 73 LANGDON, T. G. Grain boundary sliding revisited: Developments in sliding over four decades. *J. Mater. Sci.*, v 41, p. 597-609, 2006.
- 74 FANTOZZI, G.; CHEVALIER, J.; OLAGNON, C.; CHERMANT, J. L. Creep of ceramic matrix composites. *Compr. Compos. Mater.*, v. 4, p. 115-162, 2000.
- 75 NIEH, T. G.; WADSWORTH, J.; SHERBY, O. D. *Superplasticity in Metals and Ceramics*. Cambridge: Cambridge University Press, 1997.
- 76 GIFKINS, R. C. Grain-boundary sliding and its accommodation during creep and superplasticity. *Metall. Trans. A*, v. 7, p. 1225-1232, 1976.
- 77 ZELIN, M.G.; MUKHERJEE, A. K. Geometrical aspects of superplastic flow. *Mater. Sci. Eng. A*, v. 208, p. 210-225, 1996.
- 78 WANG, L. et al. Grain rotation mediated by grain boundary dislocations in nanocrystalline platinum. *Nat. Commun.*, v. 5, p. 5402, 2014.
- 79 ZIZAK, I. et al. Ion-beam-induced collective rotation of nanocrystals. *Phys. Rev. Lett.*, v. 101, p. 065503, 2008.
- 80 WANG, Y. B. et al. Deformation-induced grain rotation and growth in nanocrystalline Ni. *Appl. Phys. Lett.*, v. 92, 011903, 2008.
- 81 HARRIS, K. E.; SINGH, V. V.; KING, A. H. Grain rotation in thin films of gold. *Acta Mater.* V. 46, p. 2623–2633, 1998.

- 82 SHAN, Z. et al. Grain boundary –mediated plasticity in nanocrystalline nickel. *Science*, v. 305, p. 654-657, 2004.
- 83 OVID'KO, I. A.; SHEINERMAN, A. G. Special rotational deformation in nanocrystalline metals and ceramics. *Scripta Mater.* V. 59, p. 119–122, 2008.
- 84 LIU, P. et al. Direct dynamic atomic mechanisms of strain-induced grain rotation in nanocrystalline, textured, columnar-structured thin gold films. *Scripta Mater.* v. 64, p. 343-346, 2011.
- 85 YAMAKOV, V. et al. Deformation-mechanism map for nanocrystalline metals by molecular dynamics simulation. *Nat. Mater.*, v. 3, p. 43-47, 2004.
- 86 CAHN, J. E.; TAYLOR, J. E. A unified approach to motion of grain boundaries, relative tangential translation along grain boundaries, and grain rotation. *Acta Mater.*, v. 52, p. 4887-4898, 2004.
- 87 SWYGENHOVEN, H. V.; DERLET, P. M. Grain-boundary sliding in nanocrystalline fcc metals. *Phys. Rev. B*, v. 64, p. 224105, 2001.
- 88 KE, M.; HACKNEY, S. A.; AIFANTIS, E. C. Observation and measurement of grain rotation and plastic strain in nanostructured metal thin films. *Nanostruct. Mater.*, v. 5, p. 689-697, 1995.
- 89 JAMES, C. M. L. Mechanical grain growth in nanocrystalline copper. *Phys. Rev. Lett.*, v. 96, p. 215506, 2006.
- 90 BENSON, D. J.; FU, H.-H.; MEYERS, M. A. On the effect of grain size on yield stress: extension into nanocrystalline domain. *Mater. Sci. Eng. A*, v. 319-321, p. 854-861, 2001.
- 91 KIM, H. S.; ESTRIN, Y.; Bush, M. B. Plastic deformation behavior of fine-grained materials. *Acta Mater.*, v. 24, p. 493-504, 2000
- 92 FU, H.-H.; BENSON, D. J.; MEYERS, M. A. Analytical and computational description of effect of grain size on yield stress of metals. *Acta Mater.*, v. 49, p. 2567-2582, 2001.
- 93 BRINK, T; ALBE, K. From metallic glasses to nanocrystals: Molecular dynamics simulations on the crossover from glass-like to grain-boundary mediated deformation behaviour. *Acta Mater.*, v. 156, p. 205-214, 2018.
- 94 LANGER, J. S. Shear-transformation zone theory of deformation in metallic glasses. *Scr. Mater.*, v. 54, p. 375-379, 2006.
- 95 ZHONG, C. et al. Size distribution of shear transformation zones and their evolution towards the formation of shear bands in metallic glasses. *J. Non-Cryst. Solids.*, v. 445-446, p. 61-68, 2016.
- 96 YU, H. B.; WANG, W. H.; BAI, H.Y. Relating activation of shear transformation zones to β relaxations in metallic glasses. *Phys. Rev. B*, v. 81, p. 220201, 2010.

- 97 PEREPEZKO, J. H. et al. Nucleation of shear bands in amorphous alloys. *PNAS*, v. 18, p. 3938-3942, 2014.
- 98 LUND, A. C.; NIEH, T. G.; SCHUH C. A. Tension/compression strength asymmetry in a simulated nanocrystalline metal. *Phys. Rev. B*, v. 69, p. 012101, 2004.
- 99 COHEN, M. H.; TURNBULL, D. Metastability of amorphous structures. *Nature*, v. 203, p. 964, 1964.
- 100 SHENG, H. W. et al. Atomic packing and short-to-medium range order in metallic glasses. *Nature*, v. 439, p. 7075, 2006.
- 101 MURR, L. E. Handbook of materials structures, properties, processing and performance. Switzerland: Springer, 2015.
- 102 LESAR, R. *Introduction to computational materials science: Fundamentals to applications*. Cambridge: Cambridge University Press, 2013.
- 103 ASHBY, M. F. Physical modelling of materials problems. *Mater. Sci. Technol.*, v. 8, p. 102-111, 1992.
- 104 LO, D. S. H. *Finite element mesh generation*. Boca Raton: Taylor & Francis group, 2015.
- 105 PFALLER, S.; POSSART, G.; STEINMANN, P. Molecular dynamics and finite elements: an approach to couple different worlds. *Proc. Appl. Math. Mech.*, v. 14, p. 569-570, 2014.
- 106 LEE, J. G. *Computational materials science: An introduction*. Florida: CRC Press, 2012.
- 107 JIA, W. et al. Pushing the limit of molecular dynamics with ab initio accuracy to 100 million atoms with machine learning. arXiv:2005.00223, 2020.
- 108 ALDER, B. F.; WAINWRIGHT, T. E. Phase transition for a hard sphere system. *J. Chem. Phys.*, v. 27, p. 1208-1209, 1957.
- 109 ALDER, B. F.; WAINWRIGHT, T. E. Studies in molecular dynamics. I. General method. *J. Chem. Phys.*, v. 31, p. 459-466, 1959.
- 110 RAPAPORT, D. C. *The art of molecular dynamics simulation*. 2 ed. New York: Cambridge University Press, 2004.
- 111 WANG, X. W. et al. The Lennard-Jones potential: when (not) to use it. *Phys. Chem. Chem. Phys.*, v. 22, p. 10624-10633, 2020.
- 112 DAW, M. S.; BASKES, M. I. Semiempirical, quantum mechanical calculation of hydrogen embrittlement in metals. *Phys. Rev. Lett.*, v. 50, p. 1285-1288, 1983.
- 113 DAW, M. S.; BASKES, M. I. Embedded-atom method: derivation and application to impurities, surfaces, and other defects in metals. *Phys. Rev B*, v. 29, p. 6443-6453, 1984.

- 114 GRUBMÜLLER, H. et al. Generalized Verlet algorithm for efficient molecular dynamics simulations with long-range interactions. *Mol. Simul.*, v. 6, p. 121-142, 1991.
- 115 HAIRER, E.; LUBICH, C.; WANNER, G. Geometric numerical integration illustrated by the Störmer–Verlet method. *Acta Numer.*, v. 12, p. 399-450, 2003.
- 116 BERENDSEN, H. J. C. Molecular dynamics simulations: the limits and beyond. In: *Computational Molecular Dynamics: Challenges, Methods, Ideas*, editors P. DEUFLHARD et al., Proceeding of the 2nd International Symposium on Algorithms for Macromolecular Modelling, Berlin, May 21–24, 1997.
- 117 CHOE, J.-I.; Kim, B. Determination of proper time step for molecular dynamics simulation. *Bull. Korean Chem. Soc.*, v. 21, p. 419-424.
- 118 CICCOTTI, G.; HOOVER, W. G. *Molecular-Dynamics Simulation of Statistical-Mechanical Systems*. Amsterdam: Elsevier, 1986.
- 119 LEACH, A. R. *Molecular Modelling: Principles and Applications*. 2nd edn. Harlow: Prentice Hall, 2001.
- 120 CHOWDHURY, P. R.; FENG, T.; RUAN, X. Development of interatomic potentials for the complex binary compound Sb_2Te_3 and the prediction of thermal conductivity. *Phys. Rev. B*, v. 99, p. 155202, 2019.
- 121 VARVENNE, C. et al. Average-atom interatomic potential for random alloys. *Phys. Rev. B*, v. 93, p. 104201, 2016.
- 122 MUELLER, T; HERNANDEZ, A.; WANG, C. Machine learning for interatomic potential models. *J. Chem. Phys.*, v. 152, p. 050902, 2020.
- 123 NOSE, S. A molecular dynamics method for simulations in the canonical ensemble. *Mol. Phys.*, v. 52, p. 255-268, 1984.
- 124 PARRINELLO, M.; RAHMAN, A. Polymorphic transitions in single crystals: A new molecular dynamics method. *J. Appl. Phys.*, v. 52, p. 7182-7190, 1981.
- 125 HU, R.; NASH, P.; CHEN, Q. Enthalpy of formation in the Al-Ni-Ti system. *J. Phase Equilib. Diff.*, v. 30, p. 559-563, 2009.
- 126 SWYGENHOVEN, H. V.; CARO, A. Plastic behavior of nanophase Ni: A molecular dynamics computer simulation. *Appl. Phys. Lett.*, v. 71, p. 1652-1654, 1997.
- 127 SWYGENHOVEN, H. V; SPACZER, M.; CARO, A. Microscopic description of plasticity in computer generated metallic nanophase samples: A comparison between Cu and Ni. *Acta Mater.*, v. 47, p. 3117-3126, 1999.
- 128 SWYGENHOVEN, H. V; CARO, A.; FARKAS, D. A molecular dynamics study of polycrystalline fcc metals at the nanoscale: grain boundary structure and its influence on plastic deformation. *Mater. Sci. Eng. A*, v. 309-310, p. 440-444, 2001.

- 129 WEN, Y.-H.; ZHU, Z.-Z.; ZHU, R.-Z. Molecular dynamics study of the mechanical behavior of nickel nanowire: Strain rate effects. *Comput. Mater. Sci.*, v. 41, p. 553-560, 2008.
- 130 PUKŠIČ, N.; JENKO, M.; GODEC, M.; MCGUINNESS, P. J. A comparison of the uniaxial deformation of copper and nickel (1 1 1) surfaces: a molecular dynamics study. *Sci. Rep.*, v. 7, p. 42234, 2017.
- 131 ZHIGANG, R.; WENPING, W.; NANLIN, L. Effects of strain rate, temperature and grain size on the mechanical properties and microstructure evolutions of polycrystalline nickel nanowires: a molecular dynamics simulation. *Wuhan Univ. J. Nat. Sci.*, v. 23, p. 251-258, 2018.
- 132 KATAKAM, K. C.; GUPTA, P.; YEDLA, N. Large-Scale molecular dynamics simulation studies on deformation of Ni nanowires: Surface profile, defects and stacking fault width analysis. *J. Mater. Eng. Perform.*, v. 28, p. 63-78, 2018.
- 133 JAKSE, N. Molecular-dynamics study of liquid nickel above and below the melting point. *J. Chem. Phys.*, v. 123, p. 244512, 2005.
- 134 JARMAKANI, H. N. et al. Molecular dynamics simulations of shock compression of nickel: From monocrystals to nanocrystals. *Acta Mater.*, v. 56, p. 5584-5604.
- 135 LI, H.; DU, W.; LIU, Y. Molecular dynamics study of tension process of ni-based superalloy. *Acta Metall. Sin. (Engl. Lett.)*, v. 33, p. 741-750, 2020.
- 136 YEDLA, N. Strain controlled fatigue response of large-scale perfect and defect nickel nanowires: a molecular dynamics study. *J. Mol. Graph. Model.*, Future issue, <https://doi.org/10.1016/j.jmngm.2021.107885>, 2021.
- 137 LIU, H. et al. The effect of void defect on the evolution mechanisms of dislocations and mechanical properties in nickel-based superalloys by molecular dynamics simulation of real γ/γ' structures. *Int. J. Solids Struct.*, v. 191-192, p. 464-472, 2020.
- 138 YANG, X.-F. et al. The effect of grain boundary structures on crack nucleation in nickel nanolaminated structure: A molecular dynamics study. *Comput. Mater. Sci.*, v. 186, p. 110019, 2021.
- 139 HUANG, D.; ZHANG, Q.; QIAO, P. Molecular dynamics evaluation of strain rate and size effects on mechanical properties of FCC nickel nanowires. *Comput. Mater. Sci.*, v. 50, p. 903-910, 2011.
- 140 HESS, B.; KUTZNER, C.; SPOEL, D.; LINDAHL, E. GROMACS 4: Algorithms for highly efficient, load-balanced, and scalable molecular simulation. *J. Chem. Theory Comput.*, v. 4, p. 435-447, 2008.
- 141 PLIMPTON, S. Fast parallel algorithms for short-range molecular dynamics. *J. Comp. Phys.*, v. 117, p. 1-19., 1995.

- 142 THIELEMANN, H. C. et al. From GROMACS to LAMMPS: GRO2LAM. *J. Mol. Model.*, v. 25, p. 147, 2019.
- 143 TERSOFF, J. Modeling solid-state chemistry: Interatomic potentials for multicomponent systems. *Phys. Rev. B.*, v. 39, p. 5566, 1989.
- 144 SUN, H. COMPASS: An ab Initio force-field optimized for condensed-phase applications - overview with details on alkane and benzene compounds. *J. Phys. Chem. B.*, v. 102, p. 7338-7364, 1998.
- 145 HIREL, P. AtomsK: A tool for manipulating and converting atomic data files. *Comput. Phys. Commun.*, v. 197, p. 212-219, 2015.
- 146 VORONOI, G. Nouvelles applications des paramètres continus à la théorie de formes quadratiques. *J. Reine Angew. Math.*, v. 134, p. 198-287, 1908.
- 147 AURENHAMMER, F. Voronoi Diagrams - A survey of a fundamental geometric data structure. *ACM Comput. Surv.*, v. 23, p. 345-405, 1991.
- 148 FOX, B. L. Construction of Voronoi Polyhedra. *J. Comput. Phys.*, v. 29, p. 81-92, 1978.
- 149 OKABE, A.; BOOTS, B.; SUGIHARA, K.; CHIU, S. N. *Spatial tessellations: Concepts and applications of Voronoi diagrams*. 2nd edn. England: John Wiley & Sons, 1999.
- 150 MULCHRONE, K. F.; BILLI, A.; FAGERENG, A. Problems and solutions in structural geology and tectonics: chapter 8 - finite strain analysis using shape and point data. *Dev. Struct. Geol. Tectonics*, v. 5, p. 89-104, 2019.
- 151 POLAK, E.; RIBIÈRE, G. Note sur la convergence de directions conjuguée. *Rev. Fr. Inform. Rech. Opér.*, v. 16, p. 35-43, 1969.
- 152 KHODA, K. M.; LIU, Y.; STOREY, C. Generalized Polak-Ribière algorithm. *J. Optim. Theory Appl.*, v. 75, p. 345-354.
- 153 FAKEN, D.; JÓNSSON, H. Systematic analysis of local atomic structure combined with 3D computer graphics. *Comput. Mater. Sci.*, v. 2, p. 279-286, 1993.
- 154 SHENG, H. W. et al. Atomic packing and short-to-medium range order in metallic glasses. *Nature*, v. 439, p. 419-425, 2006.
- 155 STUKOWSKI, A.; BULATOV, V. V.; ARSENLIS, A. Automated identification and indexing of dislocations in crystal interfaces. *Model. Simul. Mater. Sci. Eng.*, v. 20, p. 085007, 2012.
- 156 STUKOWSKI, A. Visualization and analysis of atomistic simulation data with OVITO - the Open Visualization Tool. *Model. Simul. Mater. Sci. Eng.*, v. 18, p. 015012, 2010.
- 157 PANZARINO, J. F.; RUPERT, T. J. Tracking microstructure of crystalline materials: A post-processing algorithm for atomistic simulations. *JOM*, v. 66, p. 417-428, 2014.

- 158 ALIAGA, L. C. E. et al. Experimental and molecular dynamics simulation study on the glass formation of Cu–Zr–Al alloys. *Mater. Res. Express*, v. 6, p. 045202, 2019.
- 159 WARD, L.; AGRAWAL, A.; FLORES, K. M.; WINDL, W. Rapid production of accurate embedded-atom method potentials for metal alloys, arXiv:1209.0619, 2012. <https://arxiv.org/abs/1209.0619>
- 160 RIEGNER, D. Molecular dynamics simulations of metallic glass formation and structure, Ph. D. dissertation, The Ohio State University, Ohio, USA, 2016.
- 161 SAFTA, C. et al. Interatomic potentials models for Cu-Ni and Cu-Zr alloys. Sandia National Laboratories. 2014. Available online: <https://www.osti.gov/biblio/1475252>
- 162 ZHOU, X. W.; JOHNSON, R. A.; WADLEY, H. N. G. Misfit-energy increasing dislocations in vapor-deposited CoFe/NiFe multilayers. *Phys. Rev. B*, v. 69, p. 144113, 2004.
- 163 Interatomic potentials repository. National Institute of Standards and Technology (NIST). Accessed Sep. 20, 2020. Available online: <https://www.ctcms.nist.gov/potentials/>
- 164 MISHIN, Y.; FARKAS, D.; MEHL, M. J.; PAPACONSTANTOPOULOS, D. A. Interatomic potentials for monoatomic metals from experimental data and ab initio calculations. *Phys. Rev. B*, v. 59, p. 3393-3407, 1999.
- 165 RIDA, A.; MICOULAUT, M.; ROUHAUD, E.; MAKKE, A. Understanding the strain rate sensitivity of nanocrystalline copper using molecular dynamics simulations. *Comput. Mater. Sci.*, v. 172, p. 109294, 2020.
- 166 KIM, D. H.; KIM, W. T.; KIM, D. H. Formation and crystallization of Al–Ni–Ti amorphous alloys. *Mater. Sci. Eng. A*, v. 385, p. 44-53, 2004.
- 167 GUO, J. Q.; OHTERA, K. Microstructures and mechanical properties of rapidly solidified high strength Al-Ni based alloys. *Acta Mater.*, v. 46, p. 3829-3838, 1998.
- 168 KURZYDŁOWSKI, K. J. Structure and properties of metals. *Acta Phys. Pol. A*, v. 96, p. 69-79, 1999.
- 169 XU, W.; DÁVILA, L. P. Size dependence of elastic mechanical properties of nanocrystalline aluminum. *Mater. Sci. Eng. A*, v. 692, p. 90-94, 2017.
- 170 SCHIØTZ, J.; VEGGE, T.; DI TOLLA, F. D.; JACOBSEN, K. W. Atomic scale simulations of the mechanical deformation of nanocrystalline metals. *Phys. Rev. B*, v. 60, p. 11971, 1999.
- 171 HAQUE, M. A.; SAIF, M. T. A. Mechanical behavior of 30-50 nm thick aluminum films under uniaxial tension. *Scr. Mater.*, v. 47, p. 863-867, 2002.
- 172 PETERSON, J. et al. Quantifying amorphous and crystalline phase content with the atomic pair distribution function. *J. Appl. Crystallogr.*, v. 46, p. 332-336, 2012.

- 173 FENG, S. et al. Atomic structure of shear bands in $\text{Cu}_{64}\text{Zr}_{36}$ metallic glasses studied by molecular dynamics simulations. *Acta Mater.*, v. 95, p. 236-243, 2015.
- 174 DA, W. et al. Inhomogeneity of free volumes in metallic glasses under tension. *Materials*, v. 12, p. 98, 2019.
- 175 JU, S. P.; HUANG, H. H.; WU, T. Y. Investigation of the local structural rearrangement of $\text{Mg}_{67}\text{Zn}_{28}\text{Ca}_5$ bulk metallic glasses during tensile deformation: A molecular dynamics study. *Comput. Mater. Sci.*, v. 96, p. 56-62, 2015.
- 176 STEVENS, R. N. Grain-boundary sliding and diffusion creep in polycrystalline solids. *Philos. Mag.*, v. 23, p. 265-283, 1971.
- 177 MENDELEV, M. I.; KRAMER, M. J.; BECKER, C. A.; ASTA, M. Analysis of semi-empirical interatomic potentials appropriate for simulation of crystalline and liquid Al and Cu. *Philos. Mag.*, v. 88, p. 1723-1750, 2008.
- 178 MENDELEV, M. I.; UNDERWOOD, T. L.; ACKLAND, G. J. Development of an interatomic potential for the simulation of defects, plasticity, and phase transformations in titanium. *J. Chem. Phys.*, v. 145, p. 154102, 2016.
- 179 HURLEI, D. C. et al. R. H. Anisotropic elastic properties of nanocrystalline nickel thin films. *J. Mater. Res.*, v. 20, p. 1186-1193, 2005.
- 180 TOPOLSKI, K.; BRYNK, T.; GARBACZ, H. Elastic modulus of nanocrystalline titanium evaluated by cyclic tensile method. *Arch. Civ. Mech. Eng.*, v. 16, p. 927-934, 2016.
- 181 CHO, M. K. et al. Inverse Hall–Petch relation of nanostructured Ni films prepared by electrodeposition. *Curr. Appl. Phys.*, v. 10, p.57-59, 2010.
- 182 PENG, H. L.; LI, M. Z; WANG, W. H. Structural signature of plastic deformation in metallic glasses. *Phys. Rev. Lett.*, v. 106, p.135503, 2011.
- 183 VOLLATH, D. *Nanoparticles – Nanocomposites – Nanomaterials: An introduction for beginners*. Weinheim: Wiley-VCH:, 2013.
- 184 LAGERLÖF, K. P. D.; CASTAING, J.; PIROUZ, P; HEUER, A. H. Nucleation and growth of deformation twins: A perspective based on the double-cross-slip mechanism of deformation twinning. *Philos. Mag.*, v. 82, p. 2841-2854, 2002.
- 185 WANG, L.; et al. Determining the activation energies and slip systems for dislocation nucleation in body-centered cubic Mo and face-centered cubic Ni single crystals. *Scr. Mater.*, v. 65, p. 179-182, 2011.
- 186 LI, J. et al. Molecular dynamics simulation of mechanical properties of nanocrystalline platinum: Grain-size and temperature effects. *Phys. Lett. A*, v. 383, p. 1922-1928, 2019.
- 187 SANDERS, P. G.; EASTMAN, J. A.; WEERTMAN, J. R. Elastic and tensile behavior of nanocrystalline copper and palladium. *Acta Mater.*, v. 45, p. 4019-4025, 1997.

- 188 VOIGT, W. *Lehrbuch der Kristallphysik*. Braunschweig: Springer Vieweg Verlag, 1966.
- 189 REUSS, A. Berechnung der fließgrenze von mischkristallen auf grund der plastizitätsbedingung für einkristalle. *Z. Angew. Math. Mech.*, v. 9, p.49-58, 1929.
- 190 PARK, J., LAKES, R. S. *Biomaterials: An introduction*. New York: Springer, 2007.
- 191 WU, D.; WANG, X. L.; NIEH, T. G. Variation of strain rate sensitivity with grain size in Cr and other body-centred cubic metals, *J. Phys. D: Appl. Phys.*, v. 47, p.175303, 2014.
- 192 HUTCHINSON, J. W.; NEALE, K. Q. Influence of strain-rate sensitivity on necking under uniaxial tension. *Acta Metall.*, v. 25, p. 839-846, 1977.
- 193 HEDWORTH, J.; STOWELL, M. J. The measurement of strain-rate sensitivity in superplastic alloys. *J. Mater. Sci.*, v. 6, p. 1061-1069, 1971.
- 194 HART, E. W. Theory of the tensile test. *Acta Metall.*, 15, p. 351-355, 1967.
- 195 WANG, Y. M.; HAMZA, A. V.; MA, E. Temperature-dependent strain rate sensitivity and activation volume of nanocrystalline Ni. *Acta Mater.*, v. 54, p .2715-2726, 2006
- 196 WEI, Q.; CHENG, S.; RAMESH, K. T.; MA, E. Effect of nanocrystalline and ultrafine grain sizes on the strain rate sensitivity and activation volume: FCC versus BCC metals. *Mater. Sci. Eng. A*, v. 381, p. 71-79, 2004.
- 197 LU, L.; LI, S. X.; LU, K. An abnormal strain rate effect on tensile behavior in nanocrystalline copper. *Scr. Mater.*, v. 45, p. 1163-1169, 2001.
- 198 VALIEV, R. Z.; ALEXANDROV, I. V.; ZHU, Y. T.; LOWE, T. C. Paradox of strength and ductility in metals processed by severe plastic deformation. *J. Mater. Res.*, v. 17, p. 5-8, 2002.
- 199 HUMPHREY, R. T.; JANKOWSKI, A. F. Strain-rate sensitivity of strength in macro-to-micro-to-nano crystalline nickel. *Surf. Coat. Technol.*, v. 206, p. 1845-1849, 2011.
- 200 ZHANG, T.; ZHOU, K.; CHEN, Z. Q. Strain rate effect on plastic deformation of nanocrystalline copper investigated by molecular dynamics. *Mater. Sci. Eng. A*, v. 648, p. 23-30, 2015.
- 201 VEHOFF, H. et al. The effect of grain size on strain rate sensitivity and activation volume – from nano to ufg nickel. *Int. J. Mater. Res.*, v. 98, p. 259-268, 2007.
- 202 DAO, M.; LU, L.; SHEN, Y. F.; SURESH, S. Strength, strain-rate sensitivity and ductility of copper with nanoscale twins. *Acta Mater.*, v. 54, p. 5421-5432, 2006.
- 203 CHEN, J.; LU, L.; LU, K. Hardness and strain rate sensitivity of nanocrystalline Cu. *Scr. Mater.*, v. 54, p. 1913-1918, 2006.
- 204 WEI, Q. Strain rate effects in the ultrafine grain and nanocrystalline regimes – influence on some constitutive responses. *J. Mater. Sci.*, v. 42, p. 1709-1727, 2007.

- 205 MAO, Z. N.; AN, X. H.; LIAO, X. Z.; WANG, J. T. Opposite grain size dependence of strain rate sensitivity of copper at low vs high strain rates. *Mater. Sci. Eng. A*, v. 738, p. 430-438, 2018.
- 206 CAILLARD, D; MARTIN, J. L. Thermally activated mechanisms in crystal plasticity, in CAHN, R. W. (ed), *Pergamon materials series*. Pergamon, v. 8, p. 32-433.
- 207 WANG, Y. M.; HAMZA, A. V.; MA, E. Activation volume and density of mobile dislocations in plastically deforming nanocrystalline Ni. *Appl. Phys. Lett.*, v. 86, p. 241917, 2005.
- 208 OVID'KO, I. A.; SHEINERMAN, A. G. Kinetics of grain boundary sliding and rotational deformation in nanocrystalline materials. *Rev. Adv. Mater. Sci.*, v. 35, p. 45-58, 2013.
- 209 MOHANTY, G.; WEHRS, J. Room temperature stress relaxation in nanocrystalline Ni measured by micropillar compression and miniature tension. *J. Mater. Res.*, v. 31, p. 1085-1095, 2016.
- 210 WENG, G. J.; BARAI, P. Mechanics of very fine-grained nanocrystalline materials with contributions from grain interior, GB zone, and grain-boundary sliding. *Int. J. Plast.*, v. 25, p. 2410-2434, 2009.
- 211 BARACALDO, R. R.; MARRERO, J. M. C; PÁRAMO, A. B. Studying the Hall-Petch effect regarding sub-micrometer steel (0.6%C). *Ing. Investig.*, v. 31, p. 112-120, 2011.
- 212 TSUJI, N.; ITO, Y.; SAITO, Y.; MINAMINO, Y. Strength and ductility of ultrafine grained aluminum and iron produced by ARB and annealing. *Scr. Mater.*, v. 47, p. 893-899, 2002.
- 213 CHOI, H. J.; LEE, S.W.; PARK, J. S.; BAE, D. H. Positive deviation from a Hall-Petch relation in nanocrystalline aluminum. *Mater. Trans.*, v. 50, p. 640-643, 2009.

APPENDIX – Works produced from this thesis

Papers:

- “Nanograin size effects on deformation mechanisms and mechanical properties of nickel: a molecular dynamics study.”, *Journal of Nanoscience and Nanotechnology*. Accepted in 20/02/2021.
- “Molecular dynamics simulations of the mechanical behavior of nanostructured and amorphous Al₈₀Ti₁₅Ni₅ alloy.”, DOI: 10.17533/udea.redin.20201009, *Revista Facultad de Ingeniería*.
- “Inverse Hall-Petch behavior for nanocrystalline aluminum using molecular dynamics”, *Ingeniería e Investigación*, under last stage review.

Conference works:

- “Molecular dynamics study of deformation mechanisms of nanocrystalline nickel”, BARBOZA, A. M.; ALIAGA, L. C. R.; BASTOS, I. N. XXII ENMC, 2019.
- “Estudo por Dinâmica Molecular do Comportamento Mecânico da Liga Al₈₀Ti₁₅Ni₅ com Estrutura Amorfa e Nanocristalina”, BARBOZA, A. M.; ALIAGA, L. C. R.; BASTOS, I. N. XXIII CBECIMat, 2018.
- “Comportamento da relação inversa de Hall-Petch para alumínio nanocristalino usando dinâmica molecular”, BARBOZA, A. M.; ALIAGA, L. C. R.; BASTOS, I. N. XX ENMC, 2017.